UNIVERSITY OF CALIFORNIA, SAN DIEGO

Large-eddy simulation, atmospheric measurement and inverse modeling of greenhouse gas emissions at local spatial scales

A dissertation submitted in partial satisfaction of the requirements for the degree Doctor of Philosophy

in

Engineering Sciences (Mechanical Engineering)

by

Anders Andelman Nottrott

Committee in charge:

Professor Jan Kleissl, Chair
Professor Ralph Keeling
Professor Sutanu Sarkar
Professor Daniel Tartakovksy
Professor Ray Weiss

2014

The Dissertation of Anders Andelman Nottrott is approved, and it is acceptable in quality and form for publication on microfilm and electronically:

_____

_____

_____

_____

_____

Chair

University of California, San Diego

2014

DEDICATION

To my parents
and my friends

EPIGRAPH

We came all this way to explore the moon, and the most important thing is that we discovered the earth.

William A. Anders

TABLE OF CONTENTS

LIST OF FIGURES

LIST OF TABLES

ACKNOWLEDGEMENTS

I gratefully acknowledge the mentorship of my advisor Professor Jan Kleissl; his guidance and encouragement have been invaluable throughout my academic career. And Professor Ralph Keeling whose support inspired me to pursue the work in this dissertation. I am thankful to my committee members, Professor Sutanu Sarkar, Professor Daniel Tartakovksy and Professor Ray Weiss, for their valuable comments and suggestions during the preparation of this dissertation.

I am thankful to my advisors, Dr. Manvendra Dubey and Dr. Thom “Nighthawk” Rahn, and colleagues, Caleb Arata, Jesse Canfield, Dr. Keeley Costigan, Jeremy Sauer, at Los Alamos National Laboratory (LANL); and to my colleagues, Dr. Andrew Aubrey, Dr. Christian Frankenberg and Andrew Thorpe, at NASA Jet Propulsion Laboratory (JPL). Their support allowed me to participate in the RMOTC field experiment and their hard work made the experiment successful. Thank you to Wes Riesland at RMOTC who provided technical support during the field experiment.

I acknowledge the support of all my colleagues and collaborators at the University of California, San Diego. I am thankful to Dr. Anirban Garai for many interesting and insightful discussions on meteorology and atmospheric turbulence, and to Dr. Patrick Mathiesen, Dr. Neda Yaghoobian and Anthony Dominguez, Dr. Heather Graven, Dr. Camille Yver, Dr. Manfredi Manizza and Brian Franz. I am grateful to Professor Stefan Llewellyn Smith for recommending me to the American Institute of Mathematics for participation in the Sustainability Problems workshop. Thank you to Nicolas Busan, Mike Watson and Steve Roberts who provided technical support throughout my academic career.

I thank Dr. Ashley Mullen for his support.

I acknowledge the support of my advisors, Dr. Manabu Kanda and Dr. Atsushi Inagaki, and colleagues Shiho Onomura, Hiroshi Takimoto, Makoto Nakayoshi, Hideaki Kumemura and Takuya Makabe during my three month fellowship the Tokyo Institute of Technology in Ookayama, Japan. The fellowship was funded through the National Science Foundation (NSF) and Japan Society for the Promotion of Science (JSPS) EAPSI program. Thank you to the Anzai family for graciously hosting me in their home in Hayama, and for some excellent barbeque parties.

I am grateful for the financial support that made my research possible. Funding was provided through an anonymous donation to the UCSD Department of Mechanical and Aerospace Engineering, and by the National Institute of Standards and Technology (NIST) Megacities Carbon Project under award number 70NANB12H248.

Computational support for the work in Chapter 2 was provided by the National Center for Atmospheric Research (NCAR) Computational and Information Systems Laboratory (CISL), and the San Diego Supercomputer Center through the National Science Foundation (NSF) Extreme Science and Engineering Discovery Environment (XSEDE).

The content of **Chapter 2** was published in Nottrott A., Kleissl J., Keeling R., 2014, Modeling passive scalar dispersion in the atmospheric boundary layer with WRF large-eddy simulation, *Atmospheric Environment* 82, pp. 172-182. Anders Nottrott was the principal investigator and first author of this publication.

The content of **Chapter 3** has been submitted for publication in Nottrott A., Rahn T., Keeling R., Kleissl J., Dubey M., 2014, Triangulation method for source

determination at local spatial scales, Submitted to *Atmospheric Environment*. Anders Nottrott was the principal investigator and first author of this publication.

The content of **Chapter 4** is being prepared for publication in Nottrott A., Rahn T., Dubey M., Keeling R., Kleissl J., 2014, Top-down emissions quantification using atmospheric measurements from a methane controlled release experiment. Manvendra Dubey of Los Alamos National Laboratory (LANL), Earth and Environmental Systems Division was the principal investigator for the field experiment, and Anders Nottrott is the first author of the publication.

VITA

2009	Bachelor of Science, Mechanical Engineering, John Muir College, University of California, San Diego
2011	Master of Science, Engineering Sciences (Mechanical Engineering), Jacobs School of Engineering, University of California, San Diego
2014	Doctor of Philosophy, Engineering Sciences (Mechanical Engineering), Jacobs School of Engineering, University of California, San Diego

PUBLICATIONS

Nottrott A., Rahn T., Dubey M., Keeling R., Kleissl J., 2014, Top-down emissions quantification using atmospheric measurements from a methane controlled release experiment, In preparation.

Nottrott A., Rahn T., Keeling R., Kleissl J., Dubey M., 2014, Triangulation method for source determination at local spatial scales, Submitted to *Atmospheric Environment*.

Nottrott A., Kleissl J., Keeling R., 2014, Modeling passive scalar dispersion in the atmospheric boundary layer with WRF large-eddy simulation, *Atmospheric Environment* **82**, pp. 172-182.

Nottrott A., Kleissl J., Washom B., 2013, Energy dispatch schedule optimization and cost benefit analysis for grid-connected, photovoltaic-battery storage systems, *Renewable Energy* **55**, pp. 230-240.

Sun L., **Nottrott A.**, Kleissl J., 2012, Effect of hilly urban morphology on dispersion in the urban boundary layer, *Building and Environment* **48**, pp. 195-205.

Nottrott A., Onomura A., Inagaki A., Kanda M., Kleissl J., 2011, Convective heat transfer on leeward building walls in an urban environment: measurements in an outdoor scale model, *Int. J. Heat Mass Transfer*, **54** (15-16), pp. 3128-3138.

Nottrott A., Kleissl J., 2010, Validation of the NSRDB-SUNY global horizontal irradiance in California, *Solar Energy* **84** (10), pp. 1816-1827.

ABSTRACT OF THE DISSERTATION

Large-eddy simulation, atmospheric measurement and inverse modeling of greenhouse gas emissions at local spatial scales

by

Anders Andelman Nottrott

Doctor of Philosophy in Engineering Sciences (Mechanical Engineering)

University of California, San Diego

2014

Professor Jan Kleissl, Chair

Anthropogenic greenhouse gas (GHG) emissions enhance the atmospheric greenhouse effect, tend to increase the average global temperature, and contribute to global climate change. Those consequences motivate the establishment of regulatory frameworks to control and reduce GHG emissions. The credibility of emissions regulations depends on reliable, independent methods for long-term monitoring, verification and accounting of the actual emissions of market participants. Therefore the objectives of the present study are: **(1)** to evaluate the performance of state of the art trace

gas dispersion models for the atmospheric boundary layer; **(2)** to develop novel measurement and modeling techniques for quantifying GHG emissions from spatially distributed sources using a top-down approach. Top-down methods combine atmospheric measurements of GHG concentration with meteorological data, and inverse transport models to quantify emissions sources.

The ability of Weather Research and Forecasting, large-eddy simulation (WRF-LES) to model passive scalar dispersion from continuous sources in the atmospheric boundary layer was investigated. WRF-LES profiles of mean and fluctuating concentration in the daytime convective boundary layer were similar to data from laboratory experiments and other LES models. Poor turbulence resolution near the surface in neutral boundary layer simulations caused under prediction of mean dispersion in the crosswind direction, and over prediction of concentration variance in the surface layer. WRF-LES simulations also showed that the concentration intermittency factor is a promising metric for detecting source location using atmospheric measurements.

A source determination model was developed to predict the location and strength of continuous, surface level, trace gas sources using concentration and turbulence measurements at two locations. The need for measurements at only two locations is advantageous for GHG monitoring applications where large sensor arrays are unfeasible due to high equipment costs and practical constraints on sensor placement. Atmospheric measurements of turbulence and methane concentration made during an outdoor, controlled release experiment were used to demonstrate the feasibility of the source determination model. The model predicted trace gas flux with less than 50% uncertainty,

and provided an upper bound for fluxes from localized sources. The model can be used for detection and continuous, long-term monitoring of fugitive GHG emissions.

1. Introduction

1.1 Objective of the dissertation

The objectives of the present study are: **(1)** to evaluate the performance of state of the art trace gas dispersion models for the atmospheric boundary layer; **(2)** to develop novel measurement and modeling techniques for quantifying greenhouse gas emissions from spatially distributed sources using a top-down approach. The models and experiments in this study considered trace gas emissions from continuous, isokinetic, neutrally buoyant sources, and all results apply to atmospheric boundary layer turbulence over flat, homogeneous terrain. Chapter 2 describes an application of the Weather Research and Forecasting, Large Eddy Simulation (WRF-LES) to model trace gas dispersion in the atmospheric boundary layer. Chapter 2 is based on physical modeling techniques that directly simulate large scale turbulence characteristics to solve the forward dispersion problem. Chapter 3 describes a source determination method that combines atmospheric measurements of trace gas concentration and turbulence at two locations with an inverse dispersion model, to locate and quantify emissions from distributed sources. The source determination method in Chapter 3 is based on a quasi-analytical, Gaussian footprint model that solves the inverse dispersion problem. Analysis of concentration and turbulence measurements obtained during an outdoor, methane controlled release experiment are presented in Chapter 4. The feasibility of the source determination method developed in Chapter 3 was assessed using data from the field experiment.

1.2 Motivation

1.2.1 The atmospheric greenhouse effect

Radiative energy from the sun drives the Earth-atmosphere system, and Earth's atmosphere plays a vital role in regulating the climate of our planet through the atmospheric greenhouse effect. The atmospheric greenhouse effect is simply defined as "the infrared radiation energy trapped by atmospheric gasses and clouds" (Raval & Ramanathan, 1989). Approximately 69% of shortwave (solar) radiation incident at the top of the atmosphere is absorbed by the Earth-atmosphere system and transformed into thermal energy (Kiehl & Trenberth, 1997). Longwave (thermal) radiation at the surface of the Earth is trapped and re-radiated by the atmosphere. The amount of heat trapped at the surface depends on total radiative forcing. Total radiative forcing is generally a function of the atmospheric concentration of greenhouse gasses, aerosols (i.e. fine particles suspended in the atmosphere), land surface changes (e.g. deforestation) and natural events (e.g. volcanic eruptions). Those variables are drivers of global climate change and interact to produce complex climate feedbacks.

A gas that absorbs radiative energy in the thermal infrared band (wavelengths approximately 5.6 μm to 1 cm) and enhances the atmospheric greenhouse effect is referred to as a greenhouse gas (GHG). Water vapor (H_2O) and carbon dioxide (CO_2) are strong GHGs responsible for approximately 60% and 26% of the clear sky atmospheric radiative forcing, respectively (Kiehl & Trenberth, 1997). Methane (CH_4), nitrous oxide (N_2O) and ozone (O_3) are also GHGs and contribute most of the remaining atmospheric radiative forcing. H_2O, CO_2, CH_4, N_2O and O_3 were the primary GHGs present in the atmosphere during preindustrial times, i.e. before the year 1750. Anthropogenic processes

(such as energy production, transportation, and manufacturing) emit CO_2, CH_4 and N_2O, and also produce many additional GHGs which were not present in the preindustrial atmosphere (Ramanathan et al, 1985). The focus of this work is on quantifying anthropogenic emissions of greenhouse gasses at local spatial scales of O(1 km^2).

Recent atmospheric measurements of CO_2, CH_4 and N_2O have revealed significant concentration increases for those gasses during the last century. The annual change in the global mean CO_2 concentration increased from 0.7 ppm yr^{-1} in the year 1960 to 1.8 ppm yr^{-1} in 2005. In 2013 the atmospheric concentration of CO_2 measured at Mauna Loa Observatory in Hawaii surpassed 400 ppm (Keeling et al, 2013), more than 100 ppm greater than in the year 1750. The increase in atmospheric CO_2 was primarily attributed to emissions from fossil fuel combustion and effects of land use changes on plant and soil carbon. Atmospheric concentration of CH_4 was about 1.77 ppm in 2005, approximately twice the preindustrial level. The increase in atmospheric CH_4 was mostly caused by anthropogenic emissions from cultivation of ruminant animals, rice agriculture, biomass burning and industrial emissions. Atmospheric concentration of N_2O was about 0.319 ppm in the year 2005, about 18% greater than the preindustrial level. Increased atmospheric concentration of N_2O is primarily due to agriculture and associate land use change, although the relative contribution from individual anthropogenic source remains uncertain (IPCC, 2007).

Each GHG species has unique thermal radiative properties and a different atmospheric residence time. Therefore, the integrated radiative forcing over a specified time interval is different for every GHG. The global warming potential (GWP) of a GHG quantifies the potential climate impact of long-lived GHGs, and is a useful metric to

compare the relative climate impacts of different gasses. CO_2, CH_4 and N_2O are considered long-lived GHG species because they have atmospheric residence times of O(1-100 yr). The GWP is referenced against CO_2 (the most abundant GHG) so that CO_2 has a GWP of 1 over all time scales. The 20-year GWP of CH_4 and N_2O are 72 and 289, respectively (IPCC, 2007).

1.2.2 Regulation of anthropogenic GHG emissions

GHG emissions from human activity enhance the greenhouse gas effect, tend to increase the average global temperature and contribute to global climate change. In that context, humanity has a collective interest in monitoring, verification and accounting of GHG emissions. Trading of carbon emissions credits and carbon taxes are the two most widely implemented frameworks for the regulation and control of GHG emissions (Ekins & Barker, 2002).

In the former strategy, which is often referred to as “Cap-and-Trade”, a regulatory agency limits the total allowable GHG emissions within their jurisdiction and equally distributes emissions credits (permits) among producers that emit GHGs. Producers that emit less than their GHG quota trade (sell) excess credits in a regulated market to producers that emit more than their GHG quota. Year-over-year reductions in the total allowable GHG emissions within the market are enforced by the regulatory agency to achieve long term reductions in GHG emissions. California’s Global Warming Solutions Act (California AB 32), for example, established a GHG Cap-and-Trade program which includes an enforceable GHG emissions cap and tradable permits to large GHG emitters such as refineries, power plants, and industrial facilities (CARB, 2013).

A carbon tax is an indirect tax levied on GHG (carbon) emissions. A regulatory agency sets the price for carbon (GHG) emissions and producers pay fees based on the mass of GHGs they emit. A carbon tax is considered an indirect tax because it is linked to a market externality (i.e. air pollution) rather than income. The carbon tax system incentivizes reduction of total GHG emissions because producers pay fewer taxes when they reduce their GHG emissions. The Federal Council of Switzerland imposes a carbon tax on all fossil fuels (e.g. oil, natural gas). The price of carbon emissions was set at 60 CHF (67 USD) per metric ton CO_2 in the year 2014 (BAFU, 2013).

The credibility of regulatory frameworks for control and reduction of GHG emissions depends on having a reliable method for independent verification and long-term monitoring of the actual emissions of market participants. While long-term verification and monitoring is relatively straightforward for centralized GHG emissions sources, like power plants and refineries, it is complicated for distributed sources like oil and gas fields, where GHG sources from gas infrastructure, petroleum extraction and/or carbon sequestration operations are sparsely distributed over areas on the order of 1-1000 km^2. The development of a method to quantify GHG emissions from distributed sources using long-term, continuous measurements remains an open problem, and that is the focus of this work.

1.2.3 Quantifying GHG emissions

There are two methodologies for quantifying greenhouse gas (GHG) emissions, bottom-up and top-down. Bottom-up estimates combine a priori information about GHG emissions from known sources (e.g. energy production/consumption, industrial processes, agriculture, land use and waste handling) to develop temporal and spatial emissions

inventories. The EDGAR and EPA GHG databases are examples of bottom-up emissions inventories. Bottom-up inventories may be combined with atmospheric transport models (e.g. the WRF model; Sections 2.1.1 and 2.2.1) to estimate and forecast atmospheric concentration of GHGs (Petrón et al, 2012; Yver et al, 2013). Top-down estimates use direct atmospheric measurements of GHG concentration coupled with meteorological data and inverse transport models (see Sections 1.3.5, 3.2.2 and A.2) to quantify GHG emissions from a priori unknown sources (Humphries et al, 2012; Lewicki & Hilley, 2012).

There are advantages and disadvantages to each method. The bottom-up approach quantifies GHG emissions in the absence of atmospheric measurements, which is advantageous because existing measurements of GHG are sparse in both space and time. However, bottom-up inventories suffer from large uncertainties in reported emissions and the spatial distribution of emissions sources (Christen et al, 2011; Miller et al, 2013). Top-down estimates measure GHG concentration directly and have a high sensitivity to changes in the strength and distribution of actual sources (Lewicki & Hilley, 2012). The sparse spatiotemporal coverage of direct atmospheric GHG measurements has hindered the development of top-down methodologies. The lack of direct measurements has been primarily due to inadequacy of existing measurement equipment for field deployment, and the high cost of measurements (Keeling, 2008). The recent development of a robust, accurate and affordable cavity ring-down spectrometer (CRDS), and the associated field calibration systems (Crosson, 2008; Welp et al, 2012), has made accurate, long-term, continuous field measurements of GHGs feasible. With the proliferation of new technology and the availability of large volumes of continuous GHG concentration data a

new problem has arisen, namely a lack of capable modeling tools to interpret the measurements. This work is focused on the development of new top-down modeling and data analysis techniques to interpret long-term, continuous GHG measurements from stationary sensors, and obtain information about the location and strength of individual emissions sources.

1.3 Background

1.3.1 Governing equations for the atmospheric boundary layer

The atmospheric boundary layer (ABL) defined as the part of the troposphere that is directly influenced by the earth's surface, and is generally confined to the lowest 1-3 km of the atmosphere (Stull, 1988). The ABL is characterized by complex turbulent flow and responds to surface forcings on timescales of O(1 hr). The state of the ABL is quantified by the governing equations of motion which describe the thermodynamic state of the ABL, conservation of mass, conservation of momentum, conservation of heat and moisture, and conservation of passive scalar quantities.

The ideal gas law describes the thermodynamic state of gases in the ABL

$$P = \rho R T_v \,, \tag{1.1}$$

where P is air pressure, ρ is the density of moist air, T_v is the absolute, virtual air temperature, and R is the ideal gas constant for dry air. The continuity equation (conservation of mass) is written

$$\partial_t \rho + \partial_j (\rho u_j) = 0 \,, \tag{1.2}$$

where u_j is the component of fluid velocity in the j^{th} direction, ∂_t denotes a time derivative, ∂_j denotes a gradient in the j^{th} direction and $j \in \boldsymbol{Z} = [1,3]$, and summation

over *j* is implied. Assuming normal ABL conditions Businger (1982) showed that Eq. 1.2 reduces to $\partial_j u_j = 0$.

The Navier-Stokes equations are an application of Newton's Second Law for conservation of momentum. The general form of the Navier-Stokes equations for the ABL is

$$\partial_t u_i + u_j \partial_j u_i = -\delta_{i3} g - f_c \varepsilon_{ij3} u_j - \frac{1}{\rho} \partial_i p + \nu \partial_j^2 u_i \,. \qquad 1.3$$

g is gravitational acceleration, f_c is the Coriolis parameter, p is pressure and τ_{ij} is the stress tensor. δ_{ij} is the Kronecker Delta and ε_{ijk} is the Alternating Unit Tensor. Einstein summation notation is used in Eq. 1.3 and $i, j \in \boldsymbol{Z} = [1,3]$. The coordinate system for Eq. 1.3 is defined for flat terrain so that the $i = 1$ direction is aligned with the mean wind direction and normal to the gravitational acceleration vector, $i = 2$ is normal to the mean wind direction and the gravitational vector, and $i = 3$ is aligned with the gravitational acceleration vector. The first term in Eq. 1.3 represents momentum storage and the second term describes advection of momentum by the mean wind. The third term defines the gravitational acceleration vector in the $i = 3$ direction. The fourth term describes the influence of the earth's rotation on the ABL flow using the *f*-plane approximation. The fifth term describes pressure-gradient forces that drive the mean wind. The sixth term represents the influence of viscous stresses assuming the ABL flow behaves as a Newtonian, incompressible fluid.

The conservation equations for heat and moisture are applications of the First Law of Thermodynamics and describe the contribution of sensible and latent heat fluxes to the thermodynamic state of the ABL. These equations are important for quantifying heat and

moisture fluxes between the surface to atmosphere, and the reader is referred to Stull (1988) for details of their derivation. Conservation of passive scalar quantities (i.e. trace gasses) is discussed in Section 1.3.3.

Although Eq. 1.3 is a complete description of the ABL flow, its form provides little insight into the nature of ABL turbulence. A more useful form of Eq. 1.3 can be obtained by decomposing the velocity vector and pressure into mean and fluctuating (turbulent) components using the Reynolds averaging technique.

$$u_i = \overline{u_i} + u_i' \tag{1.4a}$$

$$p = \bar{p} + p' \tag{1.4b}$$

The over-bar in Eq. 1.4 represents a time averaged quantity and the prime symbol denotes an instantaneous fluctuation or deviation from the time averaged quantity. Substituting these decomposed variables into Eqs. 1.3 and taking a time-average yields a momentum conservation equation for the mean velocity in the turbulent ABL.

$$\partial_t \overline{u_i} + \overline{u_j}\partial_j \overline{u_i} = -\delta_{i3} g - f_c \varepsilon_{ij3} \overline{u_j} - \frac{1}{\bar{\rho}} \partial_i \bar{p} + \nu \partial_j^2 \overline{u_i} - \partial_j \overline{u_i' u_j'} \tag{1.5}$$

Eq. 1.5 is called the Reynolds Averaged Navier-Stokes (RANS) equation. The interpretation of the first six terms in Eq. 1.5 is analogous to Eq. 1.3, but for the mean velocity. The last term in Eq. 1.6 describes the divergence of the turbulent momentum flux, or the influence of the Reynolds' stress on the motion of the mean fluid. Recasting Eq. 1.3 in RANS form shows that turbulent motions in the ABL have a significant contribution to the mean flow in the ABL.

Turbulence kinetic energy (TKE) is a measure of turbulence intensity defined as $\bar{e} = 0.5\overline{u_j{}'u_j{}'}$, where summation over j is implied. The TKE budget equation describes the physical processes that generate turbulence (Stull, 1988).

$$\partial_t \bar{e} + \overline{u_j}\partial_j \bar{e} = \delta_{i3}\frac{g}{\bar{\theta}_v}\left(\overline{u_i{}'\theta_v{}'}\right) - \left(\overline{u_i{}'u_j{}'}\right)\partial_j \overline{u_i} - \partial_j \overline{u_j{}'e} - \frac{1}{\bar{\rho}}\partial_i \overline{u_i' p'} - \varepsilon \qquad 1.6$$

$\bar{\theta}_v$ in Eq. 1.6 is the mean virtual potential temperature. The first term in Eq. 1.6 is the local TKE storage term and the second term describes advection of TKE with the mean wind. The third term in Eq. 1.6 is the buoyant production term which describes contribution of heat flux to turbulent production or loss. Buoyant production of turbulence occurs over land during the day when the surface is warmer than the air due to solar heating. Buoyant destruction of turbulence occurs at night over land when the surface is cooler than the air. The fourth term is the mechanical shear production term. The vertical momentum flux is negative in the ABL due to surface drag. Therefore the fourth term in Eq. 1.6 tends to increase TKE. The fifth term describes the transport of TKE by turbulent motions in the fluid. The sixth term is the pressure correlation term which quantifies how TKE is redistributed in the flow by pressure perturbations. The last term in Eq. 1.6 represents the viscous dissipation of TKE which is always a loss term.

1.3.2 Atmospheric boundary layer stability

The structure of ABL turbulence depends on the atmospheric stability condition, which is generally a function of buoyant and shear forces. During the daytime solar radiation heats the ground and creates an unstable layer near the surface which drives convective circulation in the bottom ~10% of the ABL. That region is known as the surface layer (SL) or the constant flux layer. Above the SL is the mixed layer (ML)

which is characterized by large thermals (updrafts and downdrafts) and roll vortices. The ML is also impacted by mesoscale convection patterns. The top of the boundary layer is marked by a strong capping inversion, which inhibits vertical motion, traps pollutants and may produce gravity waves (Driedonks & Tennekes, 1984). At night the ground is usually cooler than the air which creates stable stratification that inhibits vertical motions. Turbulence in the stable boundary layer (SBL) is sporadic and driven by wind shear. Stable stratification causes flattening of vertical eddies, and produces large horizontal vortices (Karman-vortex streets) and gravity waves (Etling, 1990). During early morning and late evening the heat flux at the surface is nearly zero and the ABL stratification becomes neutral. The neutral ABL is a relatively transient state compared to the convective and stable regimes, and is characterized by strong shear stress in the surface layer. TKE in the neutral ABL is maintained by shear production (Grant, 1992).

Atmospheric stability is quantified in terms of the TKE budget equation (Eq. 1.6). The flux Richardson number (Ri_f) is a dimensionless ratio of the buoyant production to shear production terms (Stull, 1988).

$$Ri_f = \frac{\frac{g}{\overline{\theta}_v}\left(\overline{u_i{}'\theta_v{}'}\right)}{\left(\overline{u_i{}'u_j{}'}\right)\partial_j\overline{u}_i} \tag{1.7}$$

The critical value of $Ri_f = 1$. A flow is dynamically unstable when $Ri_f > 1$, and dynamically stable when $Ri_f < 1$. $Ri_f = 0$ for neutral flows.

A dimensionless stability parameter for the surface layer (ζ) can be derived by multiplying the buoyant production term in Eq. 1.6 by $-\kappa z/u_*^3$, where $z \equiv x_3$ is the vertical direction, $u_* \equiv \left[\left(\overline{u_1{}'u_3{}'}\right)_s^2 + \left(\overline{u_2{}'u_3{}'}\right)_s^2\right]^{1/2}$ is the friction velocity (i.e. surface

shear stress; the s subscript denotes a value at the surface) and $\kappa \approx 0.4$ is the von Kármán constant.

$$\zeta = \frac{-\kappa z g(\overline{u_i{}'\theta_v{}'})_s}{\bar{\theta}_v u_*^3} \equiv \frac{z}{L} \tag{1.8a}$$

ζ is the ratio of two length scales and provides the definition of the Obukhov length (L).

$$L = \frac{-\bar{\theta}_v u_*^3}{\kappa g(\overline{u_i{}'\theta_v{}'})_s} \tag{1.8b}$$

$\zeta > 0$ in the stable boundary layer, $\zeta < 0$ in the convective SL and $\zeta = 0$ in the neutral SL. A value of ζ in the range -0.5 to -0.05 indicates forced (mixed) convection and $\zeta < -1$ in strongly convective conditions.

1.3.3 Turbulent dispersion

Dispersion of trace gasses in the atmospheric boundary layer is driven by turbulent diffusion (Roberts & Webster, 2002), a topic pioneered by GI Taylor in 1922. Scalar (i.e. trace gas) diffusion in fluid flows is governed by the advection-diffusion equation

$$\partial_t c + u_j \partial_j c = D\partial_j^2 c + Q_n\,, \tag{1.9}$$

where c is the scalar concentration, u is the fluid velocity, D is the molecular diffusivity, ∂_t denotes a time derivative, ∂_j denotes a gradient in the j^{th} direction and summation over $j \in [1,3]$ is implied. Q_n is a general source term. Taylor's Fickian approach leads to the definition of the eddy diffusivity coefficient. This result is obtained by a Reynolds decomposition of the velocity (Eq. 1.4a) and concentration $c = \bar{c} + c'$. Substituting these decomposed variables into Eq. 1.9 and taking a time-average yields a conservation equation for scalar transport in turbulent flows.

$$\partial_t \bar{c} + \overline{u}_j \partial_j \bar{c} = D\partial_j^2 \bar{c} - \partial_j \overline{u_j' c'} + Q_i \quad 1.10$$

Eq. 1.10 can be simplified by the assumption that, in many flows (and away from boundaries), the turbulent diffusion is much greater than the molecular diffusion, i.e. $\overline{u_j' c'} \gg D\partial_j \bar{c}$. This simplification leads to Eq. 1.11 which is applicable to the atmospheric boundary layer (ABL).

$$\partial_t \bar{c} + \overline{u}_j \partial_j \bar{c} = -\partial_j \overline{u_j' c'} + Q_i \quad 1.11$$

The scalar flux density terms are then parameterized by eddy diffusivity coefficients (K),

$$\overline{u_j' c'} = -K_j \partial_j \bar{c}. \quad 1.12$$

Eq. 1.12 is a simple and useful model analogous to Fick's first law of diffusion, because the scalar flux density is proportional to the mean scalar concentration gradient. Although eddy diffusivity coefficients are flow dependent and are not known a priori, Richardson (1926) proposed the now well-known 4/3 power law for the eddy diffusivity,

$$\varepsilon = \alpha {l_c}^{4/3}, \quad 1.13$$

where l_c is the length scale of the particle clouds size and α is a constant of proportionality. This self-similarity relationship was confirmed in field experiments (Stommel, 1949; Okubo, 1971) and by rigorous mathematical analysis (Batchelor, 1952), however, a wide range of values for the parameter α have been observed ($0.002 > \alpha > 0.01$; Fischer, 1979).

Eqs. 1.9, 1.10 and 1.11 are cast in a Eulerian reference frame so that the entire flow field is specified as a function of position x_i and time t. In a Eulerian frame the observer is stationary and the fluid moves in time (relative to the observer) through specific locations in space. However, in the context of scalar diffusion it is perhaps more

natural to observe the flow from a Lagrangian reference frame. In a Lagrangian frame the observer follows the motion of an individual "fluid parcel" in space and time (i.e. the fluid parcel is stationary in time with respect to the observer) and individual fluid parcels are marked by a time-independent vector field $\boldsymbol{b}$. The disadvantage of Eulerian equations in turbulent flows is that the Eulerian equations contain non-linear advection terms for the velocity u_i *and* concentration c fields. The unknown Reynolds stresses $\overline{u_i{}'u_j{}'}$ and scalar flux densities $\overline{u_i{}'c'}$ arising from the non-linear terms require closure approximations that depend on the velocity and concentration fields, and so these approximations are not uniformly valid (Wilson & Sawford, 1996). For example, the parameterization in Eq. 1.12 assumes that the scalar flux density is linearly proportional to the mean concentration gradient and requires that the length scale of turbulence l_T is small compared to the length scale of the concentration distribution l_c (Deardorff, 1978).

The Lagrangian form of the scalar mass conservation equation (Eq. 1.9) is

$$\boldsymbol{d_t}c = D\partial_j c. \tag{1.14}$$

In Eq. 1.14 the bold derivative symbol is used to denote the material (or Lagrangian) derivative. The advantage of Eq. 1.14 over Eq. 1.9 is that the non-linear advective terms are contained implicitly without approximation in the time derivative that follows the particle motion. The same simplification used in Eq. 1.11 can be applied yield $\boldsymbol{d_t}c = 0$ from Eq. 1.14, because molecular diffusion can be neglected in the infinite Reynolds number limit. Using that assumption the Lagrangian form of the scalar mass conservation equation simply states that individual fluid parcels retain their concentration as they move through the fluid in time and gives rise to the concept of "marked fluid parcels" (Wilson

& Sawford, 1996). Thus the displacement statistics of marked particles in a fluid flow are exactly related to the concentration statistics of a passive tracer dispersing in that flow.

Working in a Lagrangian reference frame it is possible to define a timescale of diffusion. Taylor (1922) considered a stationary, homogeneous, isotropic turbulence field with passive tracer particles diffusing from a point source. The position X_i of an individual particle after some time T is a function of the particle's Lagrangian velocity U_i.

$$X_i = \int_0^T U_i dt \tag{1.15}$$

Assuming that U_i is a random function of t due to the random nature of the turbulent flow, Eq. 1.15 may be interpreted as a "random walk" of the particle during time T. If many particles are released from the same point then it is expected that $\langle X_i \rangle = 0$, where the angle brackets denote an ensemble mean over many realizations of Eq. 1.15; clearly the variance $\langle X_i^2 \rangle \neq 0$. An expression for $\langle X_i^2 \rangle$ may be written as (Draxler, 1976),

$$\langle X_i^2 \rangle = 2\overline{u_\iota' u_\iota'} \int_0^T \int_0^t R_i(\tau) d\tau dt. \tag{1.16}$$

$\overline{u_\iota' u_\iota'}$ in Eq. 1.16 is the Eulerian velocity variance, R_i is the Lagrangian autocorrelation function of the velocity and the subscript $i \in [1,3]$ represents a component of the three-dimensional velocity vector. The Lagrangian autocorrelation function is defined as

$$R_i(\tau) = \frac{\overline{U_\iota(t) U_\iota(t+\tau)}}{\overline{U_\iota(t) U_\iota(t)}}. \tag{1.17}$$

In the limit of high Reynolds number turbulence, as in the ABL, the acceleration of fluid particles in the Lagrangian reference frame is autocorrelated over time scales on the order

of the Kolmogorov timescale $t_\eta = (\nu/\bar{\epsilon})^{1/2}$, where ν the kinematic viscosity of the fluid and $\bar{\epsilon}$ is the mean dissipation rate of turbulence kinetic energy. $t_n$is the characteristic timescale of viscous dissipation and is much smaller than the integral timescale of the energy-containing eddies in the flow (Borgas & Sawford, 1990). This observation permits the assumption that the X_i and U_i evolve as a Markov process (Wilson & Sawford, 1996).

A straightforward definition of a Markov process was given by van Dop et al (1985): "A stochastic process is Markovian when its future state depends only on its present state (and some transition rule)." The conceptual interpretation of this assumption in the context of dispersion is that the future state (i.e. the position and velocity) of a particle transported in time within the flow depends only on the current state of the particle, and the local properties of the turbulence field in the vicinity of the particle. The Markovian assumption establishes the shape of Eq. 1.17 as decaying exponential that tends toward $R_i = 0$ as $\tau \to \infty$ and $R_i = 1$ at $\tau = 0$. The timescale of Lagrangian motions (T_L) is then defined from Eqs. 1.16 and 1.17 as

$$T_L = \int_0^\infty R_i d\tau. \tag{1.18}$$

The Langevin equation (Eq. 1.19) applies to Markovian processes and is commonly employed to predict the evolution of Lagrangian particle trajectories in simulations of scalar dispersion.

$$dU_i = a_i(\boldsymbol{X}, \boldsymbol{U}, t)dt + b_{ij}(\boldsymbol{X}, \boldsymbol{U}, t)dW_j(t) \tag{1.19}$$

The Langevin equation is a stochastic differential equation (SDE) represented here in the most general form. a_i and b_{ij} are known as the drift and diffusion terms, respectively and are functions of the turbulence field. dW_j is a vector component of Gaussian random noise that is uncorrelated with other components and uncorrelated in time (Wilson & Sawford, 1996); dW_j has a variance equal to dt. Eq. 1.19 is integrated along with its companion $dX_i = U_i dt$ to obtain the Lagrangian particle velocity and position. The difficulty in modeling Eq. 1.19 is to determine the drift and diffusion coefficients for complex turbulent flows like the ABL. The first rigorously derived solution for Gaussian forcing in non-stationary, inhomogeneous turbulent flows was developed by Thomson (1987).

1.3.4 Large-eddy simulation

In three-dimensional large-eddy simulation (LES), large turbulent motions are directly represented, while the effects of small scale motions are parameterized with a subgrid-scale (SGS) model. Typically LES of the atmospheric boundary layer can be classified as LES with near-wall modeling, meaning that the filter and grid are sufficiently fine to resolve 80% of the turbulence kinetic energy away from the wall (the large scales), but the viscous layer at the wall is not resolved and must be modeled. Pope (2000) summarized the primary steps in LES. A filtering operation is performed to decompose the full turbulent velocity field $\boldsymbol{u}(\boldsymbol{x}, t)$ into the sum of the filtered (or resolved) component $\widetilde{\boldsymbol{u}}(\boldsymbol{x}, t)$ and a SGS (residual) component $\boldsymbol{u}''(\boldsymbol{x}, t)$ so that

$$u_i = \widetilde{u_i} + u_i'', i \in [1,3]. \quad 1.20$$

The filtering operation is defined as

$$\widetilde{\boldsymbol{u}}(\boldsymbol{x},t) = \int G(\boldsymbol{r},\boldsymbol{x})\boldsymbol{u}(\boldsymbol{x}-\boldsymbol{r},t)d\boldsymbol{r}. \quad 1.21$$

In Eq. 1.21 *G* is the filter function and the integration is performed over the entire domain. The filtering operation is applied to the governing equations (Eqs. 1.2 and 1.3) to yield the LES equations (Deardorff, 1970).

$$\partial_i \widetilde{u_i} = 0 \quad 1.22$$

$$\partial_t \widetilde{u_i} + \partial_j \widetilde{u_i}\widetilde{u_j} = \nu\partial_j\partial_j\widetilde{u_i} - \frac{1}{\rho}\partial_i\tilde{p} - \partial_j\tau_{ij} + \widetilde{F_i} \quad 1.23$$

$\widetilde{F_i}$ is a general external forcing term. Closure of Eq. 1.23 is obtained by modeling the SGS stress tensor, $\tau_{ij} = \widetilde{u_i u_j} - \widetilde{u_i}\widetilde{u_j}$. The simplest model for the SGS stresses is the eddy-viscosity model. However, a number of more advanced models have been developed for improved accuracy. Eqs. 1.22 and 1.23 are solved numerically for $\widetilde{\boldsymbol{u}}(\boldsymbol{x},t)$, which is an approximation to the large-scale motions in one realization of a turbulent flow. In the context of computational methods for LES, the tilde accent can reflect the application of an explicit low-pass filter as defined by Eq. 1.21, or implicit filtering arising from the discrete solution of the LES equations on a finite numerical grid (Kirkil et al, 2012). The scalar advection-diffusion equation (Eq. 1.9) can also be solved in an LES framework to generate high spatiotemporal resolution concentration fields for scalars dispersing in the ABL.

$$\partial_t\tilde{c} + \widetilde{u_j}\partial_j\tilde{c} = -\partial_j\widetilde{u_j'c'} + \widetilde{Q_n} \quad 1.24$$

LES explicitly represents effects of individual turbulent eddies on scalar dispersion over the full range of ABL stability conditions, capturing both plume meandering caused by large scale structures and small scale turbulent dispersion caused by smaller eddies. Thus

LES provides the ability to simulate realistic timeseries and time dependent statistics of scalar concentration and flux in the ABL, which is not possible with analytical or stochastic models.

1.3.5 The "inverse problem"

The "inverse problem" for atmospheric dispersion is the process of quantifying pollutant emissions from an unknown source (or sources) through the application of measurements and dispersion models. The inverse problem spans a wide range of applications from entomology to public health and safety, and is often addressed in the context of emergency assessment for industrial hazards and terrorism (Singh et al, 2013). However, inverse modeling also has important applications for monitoring, verification and accounting of GHG emissions.

The source-sensor relationship describes the influence of upwind sources on downwind concentration measurements. The source-sensor relationship is quantified using footprint models and source determination models, both of which are inverse models. Due to the multi-scale and random nature of turbulence all inverse models for dispersion in the atmospheric boundary layer (ABL) are under-constrained spatially (and possibly temporally) by the availability of concentration measurements, and thus use deterministic or stochastic models that simulate atmospheric turbulence to quantify the source-sensor relationship.

An important distinction exists between footprint models and source determination models in the context of the inverse modeling. Footprint models are concerned with quantifying the relative influence of trace gas sources within the measurement region of a flux or concentration sensor, i.e. what the sensor "sees"

(Schmid, 2002). Source determination models are used to locate and quantify the rate of emissions from a source (or sources) for which location and strength are not known a priori (Zheng & Chen, 2011). Source determination models are used for localization of sources that have a finite spatial extent and inhomogeneous spatial distribution within the sensor footprint. Thus a footprint model is a component of a source determination model and additional data – such as temporal measurements of trace gas flux or concentration and atmospheric turbulence data – are necessary to infer the location and strength of sources within the sensor footprint.

The source-sensor relationship depends on a number of factors. Aside from rather obvious variables, like wind direction and the distance and height difference between the sensor and source, Lecelrc and Thurtell (1990) showed that atmospheric stability has a strong influence on the source-sensor relationship. Stability, which is defined by the relative contributions of buoyant and shear production of turbulence, dictates the nature of turbulence within the ABL (see Section 1.3.2). Kljun et al (2002) investigated the source-sensor relationship for different ABL stability conditions by modeling flux and concentration footprints. They showed that the peak location and areal extent of the footprint function varied greatly as the ABL stability ranged from strongly convective through stable. Generally, the peak of the concentration footprint occurs closer to the sensor in convective conditions than in stable conditions. The 50% level source area is smaller in convective conditions than in stable condition.

2. Modeling passive scalar dispersion in the atmospheric boundary layer with WRF large-eddy simulation

2.1 Introduction

2.1.1 Motivation

This chapter is an assessment of the capability of the Weather Research and Forecasting (WRF) Large-eddy simulation software (hereafter WRF-LES) to model passive scalar dispersion, and thereby GHG dispersion, in the atmospheric boundary layer (ABL). The advantage of WRF-LES over other LES codes is that WRF-LES is integrated within the broader WRF source code which has multi-scale (synoptic to mesoscale) weather simulation capabilities. Two-way nesting of mesoscale and local (LES) scale boundary conditions will be feasible for operational modeling in the near future (Talbot et al, 2012). This capability will enable realistic simulations of dispersion from distributed, local scale GHG emissions sources; a process which is significantly impacted by mesoscale forcing. A recent investigation of the influence of different subgrid-scale (SGS) stress models on ABL turbulence simulation in WRF-LES by Kirkil et al (2012) showed that representation of surface layer turbulence at the resolved scale is *especially* poor in WRF-LES, particularly in the neutrally stratified ABL. Poor representation of surface layer turbulence occurred regardless of the chosen SGS model and was attributed to excessive artificial diffusion in the numerical differencing scheme (E. Bou-Zeid, Personal communication, 2012). Thus the goals of this assessment are twofold. The first is to conduct a detailed investigation and validation of passive scalar dispersion in the ABL modeled using WRF-LES. The second is to understand how

WRF-LES can be used as a modeling tool to interpret and derive source information from long-term GHG concentration time series measured in the ABL.

The WRF-LES model and setup for numerical experiments are discussed in Section 2.2. Results of WRF-LES simulations are presented in Section 2.3. The vertical structure of boundary layer turbulence statistics is discussed in Sections 2.3.1 and 2.3.2, mean dispersion trajectories and concentration profiles investigated in Sections 2.3.3 and 2.3.4 and concentration fluctuations are investigated in Sections 2.3.5 and 2.3.6. A discussion of the results is presented in Sections 2.4 and 2.5, respectively. Conclusions are summarized in Section 2.5.

2.1.2 Literature review

Wills & Deardorff (1976, 1981) conducted pioneering experiments on scalar dispersion in a laboratory scale model of the convective atmospheric boundary layer (CBL). Data from those experiments established trajectories for plume rise and spread in the CBL downwind of a localized point source of a pollutant. Wills & Deardorff (1976) demonstrated that Taylor's frozen turbulence hypothesis can be applied to transform the dispersion field from a continuous point source (CPS) to that of an instantaneous line source (ILS). That result is important for numerical simulation of ABL dispersion because it can be leveraged to reduce computational cost in LES (see Section 2.2.3). Later experiments (Deardorff & Willis, 1984) investigated concentration fluctuations downwind of localized scalar sources in the CBL. Large concentration fluctuations occurred and the magnitude of those fluctuations decayed rapidly as a function of downwind distance from the source due to small scale mixing. Shaughnessy & Morton (1977) and Fackrell & Robbins (1982) studied dispersion from CPSs in neutrally

stratified boundary layers. Profiles of mean concentration and concentration fluctuations downwind of ground level sources in the neutral ABL maintain a self-similar shape, while dispersion fields from elevated releases preserve downwind self-similarity only in the crosswind direction. The nature of concentration fluctuations downwind of elevated point sources in the neutral ABL depends on the ratio of source size to characteristic length scale of turbulent structures (Fackrell & Robbins, 1982). However, this effect was less apparent in their data for ground level sources. Venkatram and Wyngaard (1988) present an excellent review of scalar dispersion in the ABL.

ABL dispersion processes span a wide range of length scales, from the integral scale down to the smallest inertial scales and the dissipation range. The large-eddy simulation (LES) technique resolves turbulent structures down to the inertial scales and is well suited to investigate the multi-scale nature of dispersion. Nieuwstadt (1992) studied dispersion from a CPS in a LES of the CBL, and decomposed the dispersion field into two components: a small scale component due to the mixing action of inertial scale eddies and a meandering component caused by large scale motions in the ABL. Nieuwstadt found that meandering was the dominant driver of mean plume spreading near the source, but became small relative to the small scale component as the vertical and crosswind dimensions of the plume approach the integral length scale of the boundary layer. Henn & Sykes (1992) used LES to study concentration fluctuations downwind of a CPS (modeled as volume source at grid resolution) dispersing in a CBL. Henn & Sykes observed large variability in scalar concentration due to the formation of “concentration filaments” generated by vortical structures in the ABL turbulence field. Yee & Chan (1997) expanded the work of Henn & Sykes and developed a model

probability distribution function for concentration fluctuations using a gamma distribution. The LES study of Dosio et al (2003) investigated passive scalar dispersion over a wide range of stability conditions from near neutral to strongly convective and developed new parameterizations for mean dispersion that are valid from nearly-neutral through strongly convective conditions.

2.2 Methodology

2.2.1 Background

The Weather Research and Forecasting model (WRF; Skamarock & Klemp, 2008) is a community model developed by the National Center for Atmospheric Research (NCAR) and the National Oceanic and Atmospheric Administration (NOAA). WRF has multi-scale, nested simulation capability (from synoptic to local scales), includes real-world land-use and topographic data, and has the capability to ingest regional-scale meteorological forcing data (i.e. data assimilation). WRF is designed to run on massively parallel computers, and it is well documented with a broad user base and support group. The Advanced Research WRF (ARW) implements a fully compressible, Euler non-hydrostatic dynamics solver that is conservative for scalar variables. ARW can run in a LES mode (WRF-LES).

Large-eddy simulation provides a framework to obtain turbulence data for ABL wind and scalar fields at greater spatiotemporal resolution than mesoscale atmospheric models or direct measurements. The LES technique directly resolves large turbulent motions in three-dimensions by computing a numerical solution to the filtered Navier-Stokes equations, while the effects of small scale motions are parameterized with a SGS model

(see Section 1.3.4). The filtered mass conservation and Navier-Stokes equations are (Deardorff, 1970)

$$\partial_i \widetilde{u_i} = 0\,, \tag{2.1}$$

$$\partial_t \widetilde{u_i} + \partial_j \widetilde{u_i}\widetilde{u_j} = \nu \partial_j \partial_j \widetilde{u_i} - \frac{1}{\rho}\partial_i \tilde{p} - \partial_j \tau_{ij} + \widetilde{F_i}\,, \tag{2.2}$$

where $\widetilde{u_i}$ is the i^{th} component of filtered velocity field, $\tilde{p}$ is the filtered pressure and τ_{ij} is the subgrid-scale stress tensor. ν and ρ are the fluid kinematic viscosity and density, respectively. $\widetilde{F_i}$ is a general forcing term, e.g. Coriolis force due the earth's rotation. ∂_j represents a spatial derivative while ∂_t is a derivative with respect to time. Einstein's summation notation is used in Eqs. 2.1 and 2.2 where $i, j \in [1,2,3]$. Closure of Eq. 2.2 is obtained by modeling τ_{ij} (for more details of SGS models in WRF-LES see Kirkil et al, 2012). Eqs. 2.1 and 2.2 are written for incompressible flow and represent an approximation of the compressible solution (in a Boussinesq approximation sense) that is solved in WRF-LES. The WRF-LES dynamical core uses finite differences (rather than a pseudospectral method) to compute spatial derivatives. Passive scalar dispersion is modeled in WRF-LES by solving the filtered advection-diffusion equation for the atmospheric boundary layer

$$\partial_t \tilde{\phi} + \widetilde{u_j}\partial_j \tilde{\phi} = -\partial_j \widetilde{u_j \phi} + S(x_j), \tag{2.3}$$

where $\tilde{\phi}$ is the resolved (filtered) scalar mass concentration, $\widetilde{u_j \phi}$ is the SGS scalar mass flux and $S(x_j)$ is the continuous source function. Molecular diffusion is assumed to be negligible in the high Reynolds number limit. The SGS scalar flux is modeled as $\widetilde{u_j \phi} = -K_\phi \partial_j \tilde{\phi}$, where K_ϕ is the SGS scalar eddy diffusivity coefficient.

Nieuwstadt (1992) defined the downwind trajectory of a scalar concentration field in terms of the centroid and first moment of the spatial distribution of the concentration field. The parameters used in this paper to describe the downwind plume trajectory in the *x*-*z* plane are (see Figure 2.1): the local (or instantaneous) plume centerline height (z_l), the average plume centerline height ($\bar{z}$), the total vertical dispersion (σ_z), the total vertical dispersion relative to the source height ($\sigma_z{}'$), the spreading component about the local centerline height (s_z) and the meandering component about the average centerline height (m_z). Analogous parameters are defined for the crosswind trajectory in the *x*-*y* plane. The reader is referred to Nieuwstadt (1992) and Appendix A.1.1 for mathematical definitions of these variables.

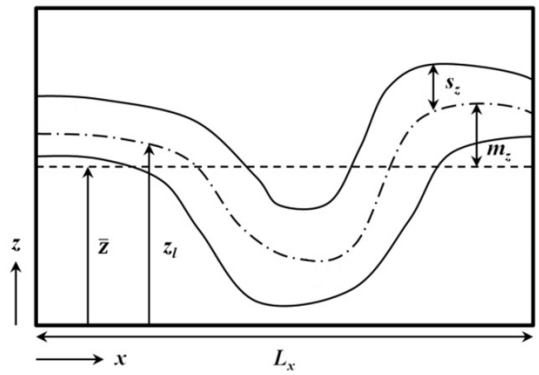

Figure 2.1: Schematic of a dispersing ILS illustrating parameters that describe the downwind trajectory of the scalar field. The *x*-axis is aligned with the mean wind $M = (\bar{u}^2 + \bar{v}^2)^{1/2}$. The parameters shown here are functions in the *x*-*z* plane, and equivalent parameters in the *x*-*y* plane are analogous. Adapted from Nieuwstadt (1992).

2.2.2 WRF configuration

WRF ARW Version 3.3 was used in this study and the WRF-LES 'namelist' configuration is listed in Table 2.1. Fifth and third-order finite difference schemes for momentum and scalars were used in the horizontal and vertical directions, respectively. The third order Runge-Kutta scheme was used for time integration. The passive scalar for

ABL dispersion simulations was activated by setting the ‘tracer_opt’ namelist parameter to a value of ‘2’. SGS diffusion for the scalar was enabled by adding a call to the ‘horizontal_diffusion’ and ‘vertical_diffusion’ subroutines in ‘module_em.F’. A mass source of passive scalar was initialized by modifying the tracer variable loop in ‘solve_em.F’ subroutine. Periodic lateral boundary conditions were enforced for the velocity, temperature and scalar, and a no penetration/absorption condition was enforced for the scalar at the lower and upper boundaries so that the total scalar mass in the domain was conserved.

Table 2.1: Namelist configuration for WRF-LES

Namelist Option	Setting (Value)
Turbulence and mixing (diff_opt)	Mixing in physical space; full diffusion (2)
Eddy coefficient (km_opt)	3D Smagorinsky first order closure (3)
Subgrid-scale model (sfs_opt)	Nonlinear backscatter and anisotropy (0)
Damping layer option (damp_opt)	w-Rayleigh damping (3)
w-Rayleigh damping coefficient (dampcoef)	0.2
Coriolis force (pert_coriolis)	Coriolis only acts on wind departures from geostrophic balance (true)
Lateral boundary conditions (periodic_x, periodic_y)	Periodic lateral boundary conditions (true)
Upper boundary condition (top_lid)	Rigid lid (true)
Surface layer option (sf_sfclay_physics)	Monin-Obukhov scheme (1)
Surface heat and moisture fluxes (isfflx)	Specified surface heat flux (2)
Scalar advection option (scalar_adv_opt)	Positive-definite advection of scalars (1)

2.2.3 Description of numerical experiments

Seven simulation cases (five domain configurations) were run for a range of ABL stability conditions from neutral through strongly convective (Table 2.2) in flat, homogeneous terrain. The aerodynamic roughness length was $z_o = 0.15$ m for all domains and the Coriolis parameters were $f = 8.5 \cdot 10^{-5}$ Hz and $e = 0$ Hz. All simulations were spun up until surface averaged shear stress and domain averaged turbulence kinetic energy were nearly constant in time. The upper 250 meters of the domain for the CBL cases was allocated as damping layer to prevent the reflection of gravity waves, and the

inversion height (z_i; defined as the lowest point of the temperature inversion) ranged from about 900-1200 m depending on the surface heat flux and time in the simulation. The inversion strength was initialized to $\partial T/\partial z$ = 0.081 K/m beginning at the base of the inversion extending upward for a distance of 100 m. Above that height the inversion strength was initialized to $\partial T/\partial z$ = 0.003 K/m up to the top of the domain. Empirical testing of WRF-LES for the neutral ABL simulations demonstrated that a deep neutral boundary layer could not be maintained because turbulent mixing at the inversion caused warm air from above the inversion to be entrained downward into the boundary layer. This resulted in the formation of a stable temperature profile throughout the boundary layer after a few hours of simulation time. Therefore, a damping layer of thickness 250 m was applied at the top of the domain to maintain a deep neutral ABL and to simulate dynamic effects of a temperature inversion in the neutral ABL simulation. The domain resolution was varied to investigate the resolution dependence of concentration fluctuations and observed errors in turbulence fields.

Table 2.2: Domain and boundary layer parameters for different numerical experiments in this study. Δz values are approximate because WRF uses vertical pressure coordinates. Simulation names are similar to Dosio et al (2003). Inversion heights in this table were initial values at the start of each simulation.

Name	L_x, L_y [m]	L_z [m]	Δx, Δy [m]	Δz [m]	U_g [m s^{-1}]	$\overline{w'\theta'}_s$ [m s^{-1} K^{-1}]	z_i [m]	u_* [m s^{-1}]	w_* [m s^{-1}]	L [m]
B3	7680	1750	30	8	0.5	0.05	1000	0.12	1.19	-2.69
B5	7680	1750	30	8	5	0.1	1000	0.28	1.48	-18.6
B5HR	3040	1500	10	2.75	5	0.1	900	0.29	1.48	-19.2
SB2	7680	1750	30	8	10	0.1	1000	0.49	1.48	-109
SB2HR	3040	1500	10	2.75	10	0.1	900	0.50	1.48	-100
N	8640	1067	30	8	15	0	815	0.6	0	-∞
NHR	7680	1067	15	4	15	0	815	0.6	0	-∞

Continuous point sources of a passive scalar were modeled as instantaneous line sources aligned parallel to the streamwise direction under the assumption of Taylor's

hypothesis (Willis & Deardorff, 1976). This approach is applicable to domains that are spatially homogeneous in the horizontal directions and it reduces the computational cost of dispersion simulations. The simulation run time for dispersion at long downwind distances is reduced by approximately L_x/M_p using the CPS to ILS transformation (L_x/M_p is the amount of time required to advect the scalar plume across the entire streamwise dimension of the domain). Ensemble average statistics of scalar concentration at any downwind location can be computed from instantaneous streamwise spatial transects of scalar concentration taken at the appropriate moment in time. The transformation from CPS to ILS is also compatible with periodic boundary conditions because it eliminates the need for sponge boundary conditions for the scalar on the streamwise domain boundaries which are required to prevent recirculation of the scalar when simulation run times are greater than L_x/M_p. Different source heights (z_s) were used for passive scalar releases to facilitate comparison of data from the present LES study with data from previous laboratory and numerical experiments. Source heights $z_s = 0.0033z_i$, $0.07z_i$, $0.19z_i$ were used in simulations B3 and B5, $z_s = 0.0033z_i$, $0.07z_i$ in simulation SB2 and $z_s = 0.0043z_i$, $0.07z_i$ in simulation N. $z_s = 0.07z_i$ in simulation NHR and $z_s = 0.0033z_i$ in simulations B5HR and SB2HR. Sources in domains B3, B5, SB2 and N were initialized using 1 grid cell in the crosswind horizontal direction and 2 grid cells in the vertical direction (Δy x $2\Delta z$; after Henn & Sykes, 1992 and Dosio et al, 2003). Sources in domains B5HR and SB2HR were initialized with $3\Delta y$ x $6\Delta z$. The source was initialized with $2\Delta y$ x $4\Delta z$ in domain NHR. The initial source volume and scalar mass were constant for all simulations, and sources were represented with more grid points in the higher resolution domains.

2.3 Results

2.3.1 Variance profiles

Figures 2.2 and 2.3 show normalized vertical profiles of the Reynolds stresses, temperature variance, kinematic heat flux for CBL and neutral ABL (cases B3, N and NHR) compared with data from established LES codes, laboratory experiments and aircraft data. Good agreement was observed between WRF-LES and validation data for the CBL (Figure 2.2). The peak in the vertical velocity variance occurred around $0.4z_i$ and the vertical profile of kinematic heat flux was linear over the depth of the boundary layer. Agreement between WRF-LES and validation data was also reasonable for the neutral ABL simulations (Figure 2.3). The magnitude of the maximum streamwise velocity variance in WRF-LES is larger than the other data, however, Moeng et al (2007) observed streamwise velocity variances as large as $9u_*^2$ in WRF-LES (using a less realistic SGS model). The peak in the vertical velocity variance occurred above the surface layer at a height of $0.2z_i$ in the low resolution domain (case N), but occurred closer to the surface around $0.1z_i$ in the high resolution domain (case NHR). This observation is consistent with the results of Kirkil et al (2012), and indicates that the SGS model is under-dissipative resulting in large $\partial\bar{u}/\partial z$. Bou-Zeid et al. (2005) demonstrated that the Lagrangian scale-dependent dynamic (LASD) SGS model produces a streamwise velocity and variance profile consistent with similarity theory and observations, however, the application of the LASD SGS model in WRF-LES did not significantly improve the vertical profile of vertical velocity variance (Kirkil et al, 2012). The variance profiles in Figure 2.3 are all within the range of the LES code inter-comparison presented in Andren et al (1994).

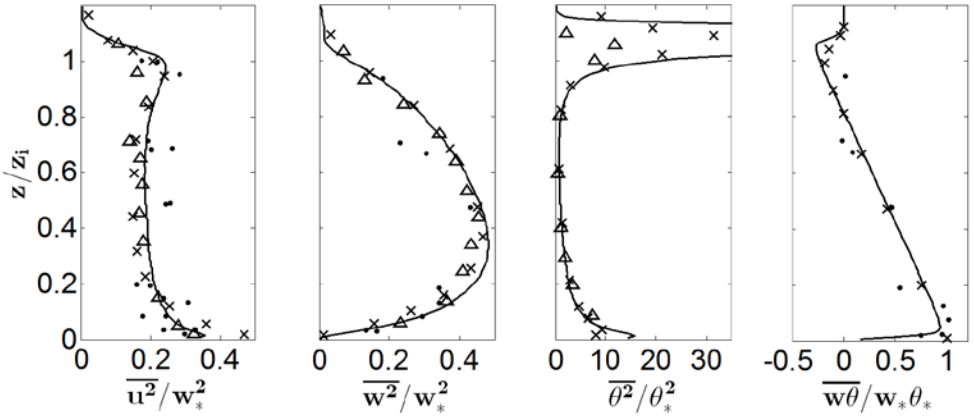

Figure 2.2: Vertical profiles of resolved velocity variance, temperature variance and heat flux normalized by the convective velocity scale and/or convective temperature scale for the CBL (WRF-LES case B3). WRF-LES resolved scales (solid line); LES of Raasch & Etling (1991; crosses); water channel data of Willis & Deardorff (1976; triangles); aircraft data of Lenschow et al (1980; dots).

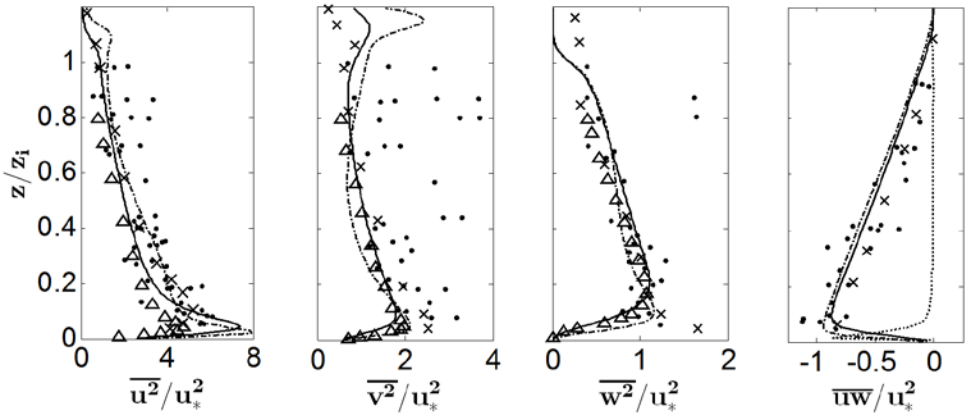

Figure 2.3: Vertical profiles of velocity variance and momentum flux normalized by the surface shear stress in the neutral ABL (WRF-LES case N). WRF-LES simulation N resolved scales (solid line) and subgrid-scales (dotted line); WRF-LES simulation NHR resolved scales (dash-dotted line); LES of Moeng & Sullivan (1994; crosses); WRF-LES using nonlinear backscatter and anisotropy SGS model with $\Delta x = \Delta y = 32$ m and $\Delta z = 8$ m Kirkil et al (2012; triangles); aircraft data from Grant (1986; dots).

2.3.2 Validity of CPS to ILS transformation

Continuous point source releases of passive scalars were modeled as instantaneous line sources under the assumption of Taylor's hypothesis. The transformation between downwind distance and time is $x = M_p t$, where M_p is the mean

wind speed at the average vertical centerline height of the plume $\bar{z}$. This transformation is only valid when the intensity of turbulent velocity fluctuations is small compared to the mean wind speed, i.e. $\overline{u_i}^2/{M_p}^2 \ll 1$. Figure 2.4 shows vertical profiles of velocity variances divided by mean wind speed for all simulations. The assumption of Taylor's hypothesis is not valid for case B3 but is reasonable for all other cases. Dosio et al (2003) found that although the CPS to ILS transformation was not strictly valid for their B3 case the mean downwind trajectory of the dispersion field matched experimental data quite well. Nevertheless, Figure 2.4 indicates that concentration fluctuations from the ILS dispersion field in the B3 boundary layer are not comparable to concentration fluctuations from a CPS released in the same turbulence field, so data from the B3 case was not used to investigate scalar concentration fluctuations.

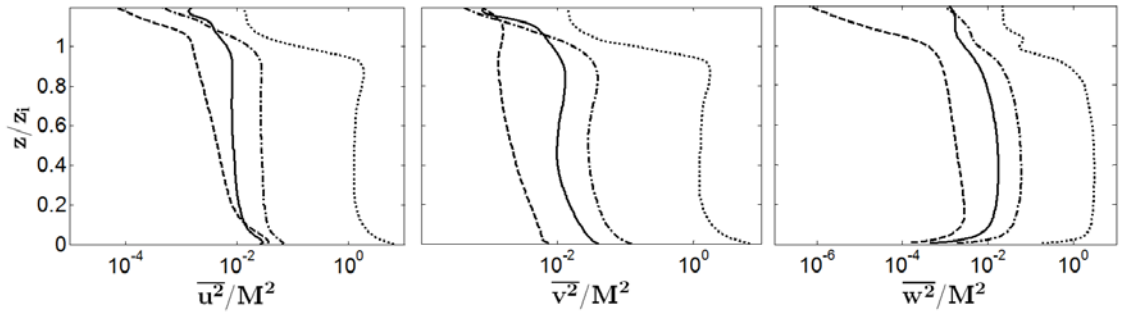

Figure 2.4: Vertical profiles of velocity variance to mean wind speed ratio for all simulation cases. B3 (short dash line), B5 (dash-dot line), SB2 (solid line) and N (long dash line). Data from the high resolution cases B5HR, SB2HR and NHR (not shown) are similar.

2.3.3 Plume trajectories

A dimensionless downwind distance parameter

$$X = \frac{w_*}{z_i}\frac{x}{M_p} = \frac{w_*}{z_i}t, \qquad 2.4$$

is defined after Willis & Deardorff (1976), where x is the downwind distance from the source and t is the downwind travel time (consistent with the transformation described in Section 2.3.2). A modified dimensionless downwind distance X_m is defined by substituting the convective velocity scale in Eq. 2.3 with a mixed velocity scale w_m. w_m applies when the buoyant and shear turbulent production are of similar magnitude. Moeng & Sullivan (1994) proposed the relationship $w_m^3 = w_*^3 + 5u_*^3$. Figure 5 shows the components of mean dispersion parameters modeled with WRF-LES for a surface layer release in the CBL compared with data from laboratory experiments. The modeled mean dispersion parameters generally fall within the range of the experimental data, with the exception of the total horizontal crosswind dispersion (Figure 2.5c) which becomes smaller than the experimental data for $X > 1.25$. This behavior was also observed in the LES study of Dosio et al (2003). It is interesting that the contribution of the meandering component (m_y) to σ_y becomes constant downwind of $X > 1.25$ although σ_y continues to grow. This observation indicates that beyond $X > 1.25$ the horizontal crosswind dispersion is primarily driven by the spreading component of dispersion (s_z).

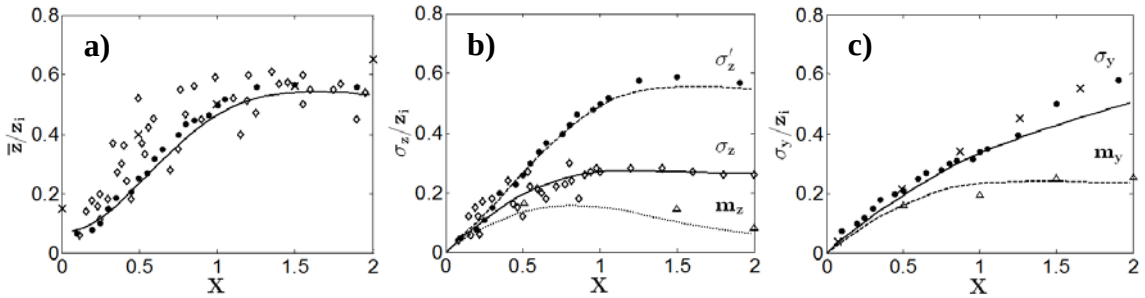

Figure 2.5: Validation of mean dispersion parameters for a passive scalar release in the CBL (case B3) plotted as a function of dimensionless downwind distance X (Eq. 2.4). The source was located at $X = 0$ and $z_s = 0.07z_i$. **a)** Mean plume height, **b)** total vertical dispersion and vertical meandering component, and **c)** total horizontal crosswind dispersion and crosswind meandering component. WRF-LES results are plotted as continuous lines and experimental data are plotted as symbols; Willis & Deardorff (1976; dots), Briggs (1993; diamonds) and Weil et al (2002; crosses and triangles). Each line in Figure 2.5b,c shows a different component of dispersion, and the label above each line indicates the variable that corresponds to the appropriate component of dispersion (refer to Section 2.2.1, Figure 2.1 and Appendix A.1.1).

Figure 2.6 shows mean dispersion trajectories downwind of point sources in moderately convective (case SB2) and neutral (case N) ABLs compared with results from the LES of Dosio et al (2003). The mean plume height (Figure 2.6a) and total vertical dispersion (Figure 2.6b) are in close agreement with Dosio et al for both the SB2 and N cases. The total horizontal crosswind dispersion (σ_y/z_i; Figure 2.6c) for the WRF-LES SB2 case is similar to the Dosio et al data for $X_m < 1.25$, but begins to diverge farther downwind. However, σ_y/z_i in the WRF-LES simulation N is significantly smaller than the Dosio et al data. We investigated the dependence of $\sigma_y(X_m)$ on SGS scalar flux by setting the $-\partial_j \widetilde{u_j \phi}$ term in Eq. 2.3 to zero (Appendix A.1.2). Excluding the $-\partial_j \widetilde{u_j \phi}$ term in case N caused a 5% decrease in $\sigma_y(X_m)$ at $X_m = 0.25$. Including the $-\partial_j \widetilde{u_j \phi}$ term, $\sigma_y(X_m)$ was about 10% larger at $X_m = 0.25$ for the surface layer release ($z_s = 0.07z_i$) in the NHR case compared to case N. The fact that $\sigma_y(X_m)$ becomes larger and more accurate with

increasing resolution indicates a deficiency in the SGS model, likely an under prediction of $K_{\phi,h}$ (see Section 2.4).

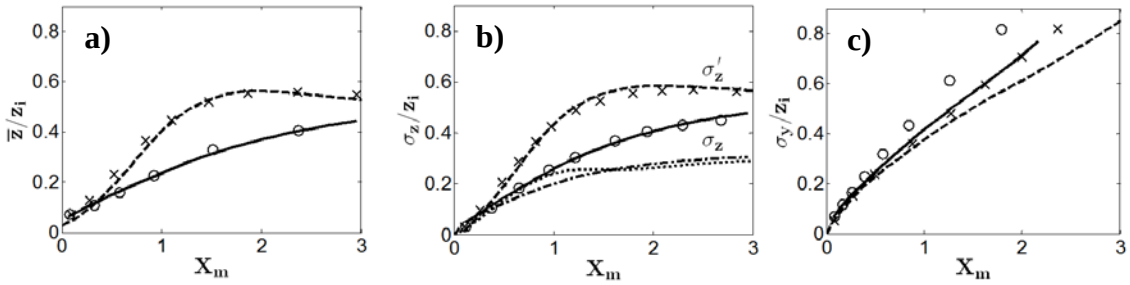

Figure 2.6: Validation of mean dispersion parameters for a passive scalar release in cases SB2 and N plotted as a function of dimensionless downwind distance X_m (Eq. 2.4). The source was located at X_m = 0 and z_s = 0.07z_i. **a)** Mean plume height, **b)** total vertical dispersion, and **c)** total horizontal crosswind dispersion. WRF-LES results are plotted with continuous lines (SB2 long and short dash lines; N solid and dash-dot lines). WRF-LES data are compared to LES data from Dosio et al (2003) plotted with crosses for SB2 and circles for N. Each pair of lines in Figure 2.6b (long dash/solid and short dash/dash-dot) shows a different component of dispersion. The label above indicates the variable that corresponds to the appropriate component of dispersion (refer to Section 2.1, Figure 2.1 and Appendix A.1.1).

2.3.4 Mean concentration profiles

Figure 2.7 shows contours of dimensionless mean concentration $c_* = \bar{c}(x,y,z)z_i^2 M_p/S$ for a surface layer source in the B3 simulation. Figure 2.7a is a vertical cross-section along the plume centerline, while Figure 2.7b shows total c_* from the surface to the inversion height. The magnitude and shape of c_* contours are very similar to the laboratory measurements of Willis & Deardorff (1976), although the plume width (Figure 2.7b) is slightly underestimated by WRF-LES for X > 1.25 (consistent with Figure 2.5c). Profiles of average scalar concentration in the CBL do not exhibit self-similar behavior when normalized σ_y or σ_z, because CBL turbulence is dominated by large coherent structures and therefore non-Gaussian (for example refer to laboratory data in Willis & Deardorff, 1976).

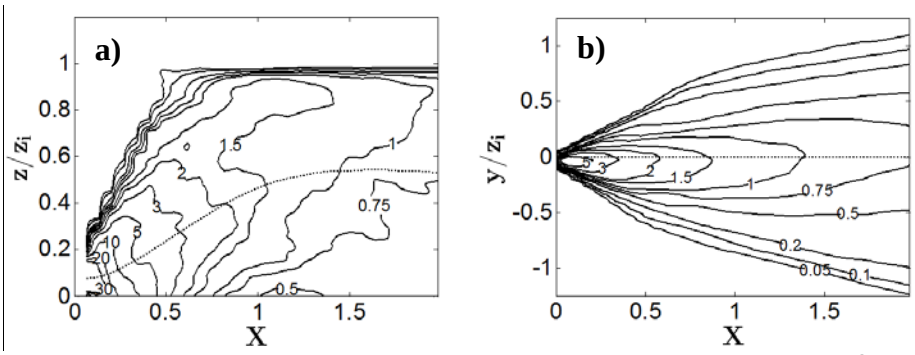

Figure 2.7: Contours of dimensionless mean concentration $c_* = \bar{c}(x, y, z)z_i^2 M_p/S$ for a surface layer (z_s = 0.07z_i) release in the B3 simulation. **a)** Vertical cross-section along the plume centerline; **b)** integrated over the z-direction from the surface to the inversion height. The dashed lines indicate the plume centerline ($\bar{z}$ and $\bar{y}$).

Figure 2.8 shows vertical profiles of mean concentration along the plume centerline at different locations downwind of ground-level and surface layer sources released in case N. Figure 2.8a shows the expected self-similarity of the mean concentration field due to the presence of the ground. Consistent with the water channel experiments of Fackrell & Robins (1982), self-similarity does not occur in the vertical direction for surface layer releases (Figure 2.8b). Figure 2.9 confirms self-similarity of the crosswind horizontal concentration profiles in the neutral boundary layer simulation (Shaughnessy & Morton, 1977). The slight negative skewness apparent in Figure 2.9 occurred because the mean wind direction was not exactly parallel to the direction of the ILS when the source was initialized due to the Coriolis force. Although the data shown in Figure 2.9 are for a surface layer source, self-similarity was also observed for the ground-level source.

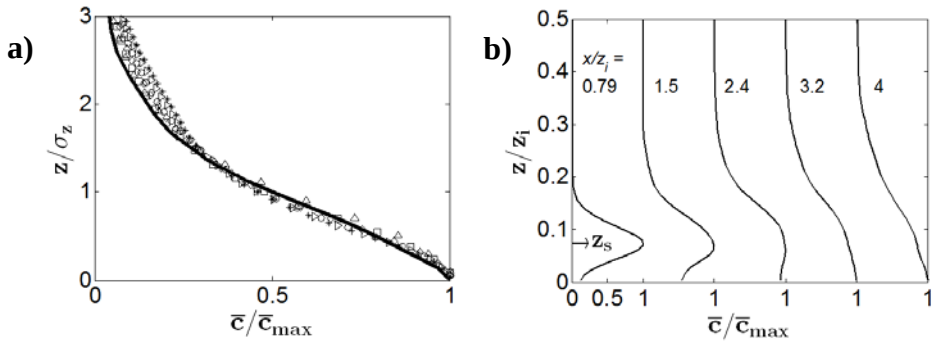

Figure 2.8: Vertical profiles of mean concentration at various downwind locations along the plume centerline. **a)** A ground-level source ($z_s = 0.0043z_i$), and **b)** a source in the surface layer ($z_s = 0.07z_i$) in case N. The mean concentration is normalized by the maximum mean concentration at each downwind location. Figure 2.8a: x/z_i = 2.1 (triangles); 3.0 (squares); 3.9 (diamonds); 4.7 (circles); 5.6 (leftward arrows); 6.5 (stars). A fit to data from Fackrell & Robbins (1982) is shown by the line in Figure 2.8a. Profiles in Figure 2.8b are offset by $\bar{c}/\bar{c}_{max}$ = 1 for readability.

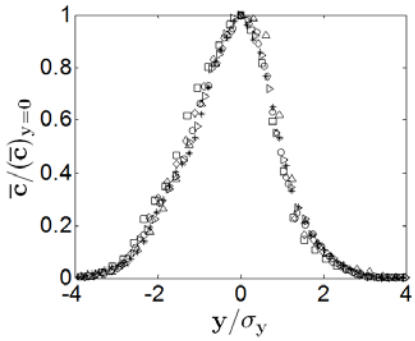

Figure 2.9: Self-similarity of horizontal crosswind profiles of mean concentration at various downwind locations at the height of the plume vertical centerline ($\bar{z}$) for a surface layer ($z_s = 0.07z_i$) source in case N. The mean concentration is normalized by the maximum mean concentration (i.e. mean concentration at y = 0) at each downwind location. x/z_i = 2.4 (triangles); 3.2 (squares); 4.0 (diamonds); 4.9 (circles); 5.8 (leftward arrows); 6.6 (stars).

2.3.5 Concentration fluctuations

Available data on concentration fluctuations in the CBL are somewhat unstructured making direct validation of the present LES experiments challenging. Figure 2.10 shows vertical and horizontal profiles of normalized concentration variance at different distances downwind of an elevated release located at $z_s = 0.19z_i$ in case B5. The variance profiles in Figure 2.10a illustrate downward motion of the plume (i.e. looping)

downwind of the source which is a characteristic feature of neutrally buoyant releases from elevated sources in the CBL (Henn & Sykes, 1992). Figure 2.10b shows crosswind horizontal profiles of concentration variance, normalized by the mean variance in the region $|y| < 0.25\sigma_y$, at the centerline height of the plume. The WRF-LES model correctly captures the peak in the concentration variance that occurs in the range $0.5 < y/\sigma_y < 1.5$ (Venkatram & Wyngaard, 1988) although there is considerable scatter in the WRF-LES data. Figure 2.11 shows a comparison of ground-level concentration standard deviation from the same elevated release as in Figure 2.10 with data from Henn & Sykes (1992). The data are of similar magnitude but do not match exactly because the sources were located at slightly different heights in the boundary layer. The larger standard deviation of the WRF-LES data may be due to the higher spatial resolution used in our simulations compared to Henn & Sykes.

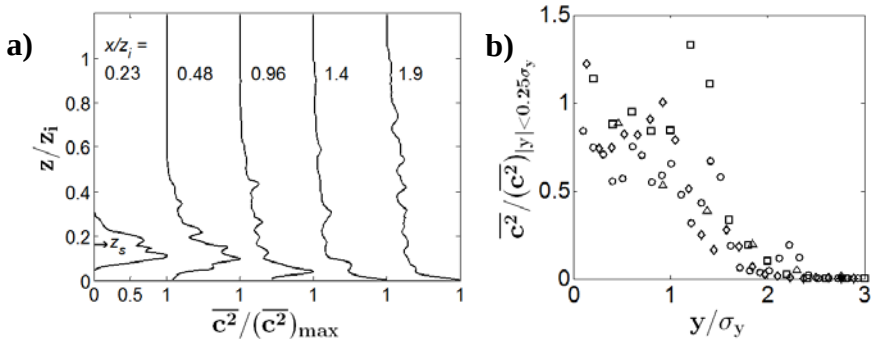

Figure 2.10: Vertical and horizontal profiles of normalized concentration variance at different distances downwind of an elevated release located at $z_s = 0.19z_i$ in case B5. **a)** Vertical profiles of concentration variance normalized by the maximum variance at each downwind position. **b)** Crosswind horizontal profiles of concentration variance at the vertical centerline height normalized by the mean variance in the region $|y| < 0.25\sigma_y$. x/z_i = 0.23 (triangles); 0.70 (squares); 1.2 (diamonds); 1.6 (circles). Profiles in Figure 2.10a are offset by $\overline{c^2}/(\overline{c^2})_{max} = 1$ for readability.

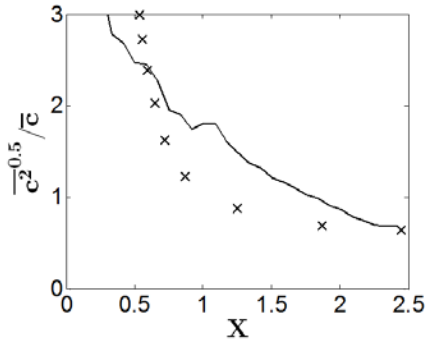

Figure 2.11: Standard deviation of ground-level concentration fluctuations downwind of an elevated source normalized by the mean ground level concentration. WRF-LES data for a source located at $z_s = 0.19z_i$ in case B5 (solid line). LES data from Henn & Sykes (1992) for an elevated source at $z_s = 0.25z_i$ (crosses).

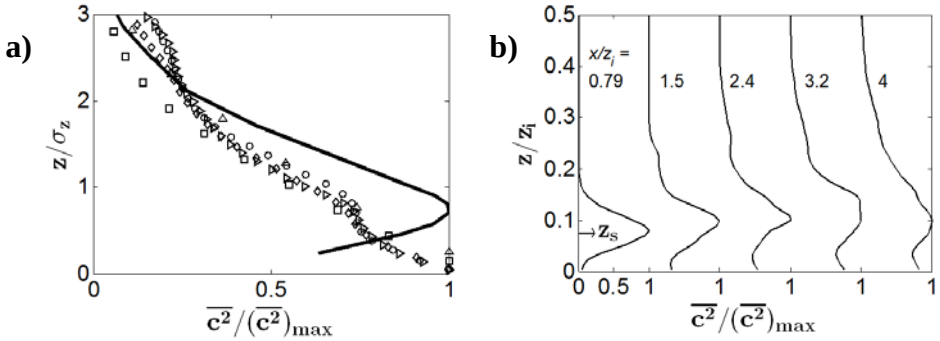

Figure 2.12: Vertical profiles of concentration variance at different downwind locations along the plume centerline for **a)** a ground-level source ($z_s = 0.0043z_i$), and **b)** a source in the surface layer ($z_s = 0.07z_i$) in case N. The concentration variance in normalized by the maximum variance at each downwind location. Figure 2.12a: $x/z_i = 0.59$ (triangles); 1.3 (squares); 3.9 (diamonds); 4.7 (circles); 5.6 (arrows). A fit to data from Fackrell & Robbins (1982) is shown by the line in Figure 2.12a. Profiles in Figure 2.12b are offset by $\bar{c}/\bar{c}_{max} = 1$ for readability.

Figure 2.12 shows vertical profiles of normalized concentration variance for ground-level and surface layer sources in case N. Wind tunnel experiments of Fackrell & Robbins (1982) showed that vertical profiles of normalized variance for ground-level sources are self-similar along the plume centerline axis with a maximum value at z/σz ≈ 0.75. Fackrell & Robbins also hypothesized that the value of $\overline{c^2}$ should tend toward zero at the surface although their lowest measurements did not extend below 0.05zi. The WRF-LES data in Figure 2.12a are approximately self-similar. Although there is a local

maximum in the WRF-LES profiles at $z/\sigma_z \approx 0.75$, the normalized variance approaches a value of 1 at the surface rather than 0. The vertical profiles for the surface layer source (Figure 2.12b) exhibit the correct upward trend for $\left(\overline{c^2}\right)_{max}$, but also show a local maximum in concentration variance at the surface. Figure 2.13 shows crosswind horizontal profiles of normalized concentration variance at different distances downwind at the height of plume vertical centerline for the surface layer release (zs = 0.07zi). The data in Figure 2.13 exhibit the weak peak in concentration variance that occurs at $y/\sigma y \approx 0.5$ but do not preserve self-similarity (see Figure 7 in Fackrell & Robbins, 1982).

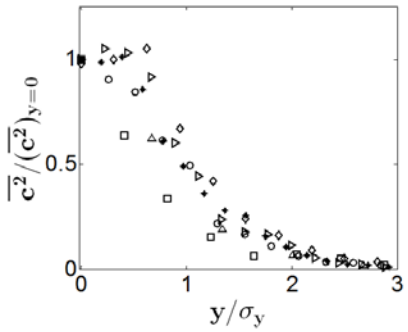

Figure 2.13: Crosswind horizontal profiles of concentration variance at the height of the plume vertical centerline, normalized by the variance at the horizontal centerline of the plume (i.e. the variance at $y = 0$) for a surface layer release $z_s = 0.07z_i$ in case N. x/z_i = 0.79 (triangles); 1.5 (squares); 2.4 (diamonds); 3.2 (circles); 4.0 (leftward arrows); 4.9 (stars).

2.3.6 Intermittency factor for ground-level sources

The intermittency factor (γ) for a timeseries of a scalar (c) is defined as the fraction of time during which the magnitude of c exceeds a threshold value (c_T): $\gamma \equiv \tau/T$, T is the total length of the timeseries and τ is the total length of time during which $c > c_T$. The intermittency factor is an alternative metric to standard statistical moments for quantifying concentration variability in a timeseries of measurements. Figure 2.14 shows contours of γ in the *x*-*z* plane along the horizontal centerline of the plume for ground-

level releases in simulations B5HR, SB2HR and N. Direct comparison of γ with data from experiments or other LES studies is difficult because γ depends on both source area relative to the characteristic length scale of turbulence (Fackrell & Robbins, 1982) and the velocity of the source gas (Venkatram & Wyngaard, 1988). Nevertheless the magnitude and shape of contours downwind of the source in Figure 2.14a are comparable to data from the lab experiments of Willis & Deardorff (presented in Venkatram & Wyngaard, 1988). The intermittency factor profiles for the B5 and SB2 simulations were nearly identical to Figures 2.14a,b although the profile for SB2 exhibited a stronger downwind gradient in γ near the surface. A value of $\gamma \geq 0.95$ downwind of a ground-level source in the neutral ABL (Figure 2.14c) is consistent with the wind tunnel experiments (Fackrell & Robbins, 1982). The most interesting feature of Figures 2.14a,b is the gradient in γ that occurs near the surface downwind of sources in the CBL. That gradient may provide the ability to estimate the source-sensor distance for sources upwind of an in situ concentration measurement in the daytime atmospheric surface layer.

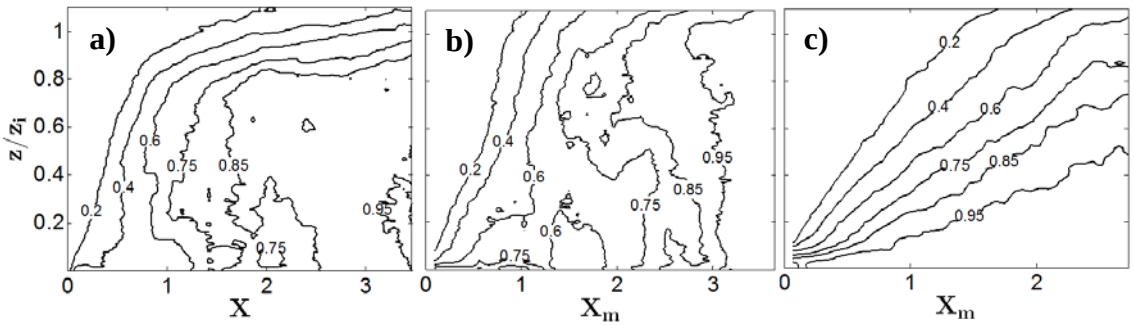

Figure 2.14: Contours of the intermittency factor (γ) in the *x*-*z* plane along the horizontal centerline of the plume for ground-level releases located at $X = 0$. **a)** Simulation B5HR ($z_s = 0.0033z_i$); **b)** simulation SB2HR ($z_s = 0.0033z_i$); **c)** simulation N ($z_s = 0.0043z_i$). The threshold was $c_T = 0.1\bar{c}$.

2.4 Discussion and conclusions

WRF-LES is a useful and relatively accessible tool for simulating turbulence and passive scalar dispersion in the atmospheric boundary layer. There are real practical advantages of WRF-LES when compared with other LES codes including, the regular/modular structure of the source code, extensive documentation and example simulations, widely connected user base (more than 20,000 WRF ARW users worldwide) and helpful support group. The most significant disadvantage of WRF-LES appears to be excessive numerical diffusion in the dynamic solver which causes poor resolution of surface layer turbulence in shear driven boundary layers (Kirkil et al, 2012). We have shown that this problem can be mitigated by increasing the spatial resolution of the numerical grid (Figure 2.3), but the computational cost of that solution is usually prohibitive.

WRF-LES accurately modeled mean dispersion parameters for passive scalars in the CBL. However, as the relative contribution of shear production to buoyant production increased (i.e. $L \to -\infty$) WRF-LES tended to underestimate the growth of the crosswind horizontal plume width as a function of downwind distance. This error was especially significant in the neutral atmospheric boundary layer (Figure 2.6c). The underestimation of σ_y/z_i in the WRF-LES simulation N was attributed to a bias in the horizontal SGS eddy diffusivity coefficient for scalars ($K_{\phi,h}$). WRF-LES assumes $K_{\phi,h} = 3K_{m,h}$, where $K_{m,h}$ is the horizontal SGS eddy diffusivity coefficient for momentum, and $K_{m,h}$ is calculated by the SGS model for the momentum equation (Eq. 2.2). This is claim is supported by the fact that a 10% increase in σ_y/z_i was observed when a source of identical volume was modeled in case NHR instead of case N (see Appendix A.1.2). It is unlikely that the

underestimation of $\sigma_y(X)$ was related to poor resolution of the source, because the bias increased with downwind distance where the plume is resolved by O(10-100) grid cells. The observed bias in the scalar field is consistent with the underestimation of the streamwise and crosswind horizontal turbulent velocity variances in Figure 2.4. Future WRF-LES research should focus on improving parameterizations for the eddy diffusivity coefficients in the wall-layer where a zonal approach like the Two-Layer Model (TLM; Piomelli & Balaras, 2002) may be appropriate. That self-similarity was preserved in the mean concentration profiles downwind of the ground-level source in the neutral simulations (Figures 2.8a and 2.9) indicates that *relative* plume dispersion was modeled correctly. It is worth noting as an aside that replacing w_m by u_* results in better agreement between the neutral boundary layer data in Figure 2.6c. That observation indicates that w_m is not an appropriate velocity scale for normalizing the downwind distance (X_m) in the neutral boundary layer, because $w_m \neq u_*$ when $\overline{w'\theta'}_s = 0$.

A disadvantage of LES for dispersion simulations is that the minimum source size is limited by the spatial resolution of the numerical grid. The smallest source volume that can be practically represented in full scale simulations of the ABL is of O(100-1000 m^3) due to the high computational cost of LES. This limitation results in a low pass filtering of the true concentration timeseries. Weil et al (2012) addressed this issue by incorporating a stochastic, Lagrangian particle dispersion model into an LES of the CBL. Validation of scalar concentration fluctuations modeled with WRF-LES was complicated by the fact that measures of concentration variability depend on source size, effluent velocity and grid resolution; all of which vary considerably among data presented in existing literature. Reasonable agreement was observed between concentration variance

profiles calculated from the LES data of Henn & Sykes (1992) and data from the present study in the CBL (Figures 2.10 and 2.11). However, for case N WRF-LES greatly overestimated the magnitude of the concentration variance in the neutral surface layer compared to wind tunnel experiments (Figure 2.12a). This issue is likely related to poor turbulence resolution in the neutral surface layer, because smaller $\overline{u_i^2}$ causes less dispersion of concentration filaments which results in large concentration fluctuations and increased concentration variance near the surface. Timeseries of scalar concentration in the atmospheric boundary layer are non-stationary and non-Gaussian. Therefore the intermittency factor (γ) is a useful alternative metric to mean and variance for quantifying concentration variability, because the relationship between the low order moments of a timeseries of concentration measurements and the probability distribution for the instantaneous concentration magnitude is not straightforward (Yee & Chan, 1997). A gradient in the intermittency factor (γ) was observed near the surface downwind of ground-level sources in the daytime convective boundary layer. This finding indicates that γ is a promising metric for estimating source-sensor distance in practical, local-scale source determination applications where the location of upwind sources within the concentration footprint of a measurement sensor is unknown. However, the relationship between γ and source-sensor range may depend on mesoscale forcing, topography and/or source area effects which would need to be quantified using site specific models and in situ measurements.

Acknowledgement

The content of Chapter 2 was published in Nottrott A., Kleissl J., Keeling R., 2014, Modeling passive scalar dispersion in the atmospheric boundary layer with WRF large-eddy simulation, *Atmospheric Environment* 82, pp. 172-182. Anders Nottrott was the principal investigator and first author of this publication.

3. Triangulation method for source determination at local spatial scales

3.1 Introduction

3.1.1 Motivation and background

The development of top-down, inverse models (refer to Sections 1.2.3 and 1.3.5) to quantify greenhouse gas (GHG) emissions from distributed sources using long-term, continuous measurements remains an open problem with important applications for the control, regulation and financial valuation of GHG emissions. This chapter describes a source determination model that uses in situ, surface level measurements of trace gas concentration and atmospheric turbulence at only two locations as model input. Source determination models are used to locate and quantify the rate of emissions from a source (or sources) for which location and strength are not known a priori (Section 1.3.5). The source location is determined by triangulation (Figure 3.1). Localization of trace gas sources by triangulation has been proposed by Gruber et al (1960) and Henry et al (2002), and is analogous to the technique of beamforming in signal processing (Chen et al, 2002). After the source location is determined a concentration footprint model (i.e. an inverse dispersion model) is used to quantify the source strength. We have developed a novel model framework which combines aspects of source-sensor orientation and uncertainty in source location with a concentration footprint model to quantify the accuracy of the proposed source determination method at local spatial scales of O(1 km^2).

Due to the multi-scale and random nature of turbulence, all inverse models for dispersion in the atmospheric boundary layer (ABL) are under-constrained spatially (and possibly temporally) by the availability of concentration measurements. Thus inverse atmospheric dispersion models use deterministic or stochastic methods to simulate

atmospheric turbulence and quantify the source-sensor relationship. Many previous studies have developed source determination models that use concentration measurements obtained from an array of detectors to quantify a priori unknown source parameters for single and multiple point releases (Singh et al, 2013; Lewicki & Hilley, 2012; Humphries et al, 2012; Zheng & Chen, 2011; Keats et al, 2007). The methods used in those studies provide accurate predictions of source location and strength, however, all results incorporated measured concentration data from a large number of sensors (between 5 and 42) arrayed downwind of the source. A large sensor array is impractical for GHG monitoring applications due to high equipment costs and practical constraints on feasible sites for sensor placement (such as topography and land/infrastructure ownership). Henry et al (2002), Christen et al (2011) and Nottrott et al (2013a, 2013b) have shown that it is possible to obtain the azimuth of ground level sources of trace gases in the vicinity of a single concentration sensor by partitioning concentration measurements as a function of wind direction. However, in the absence of a priori information about source strength, or at least one additional set of concentration measurements, it is not possible to constrain the source-sensor distance.

3.1.2 Model formulation

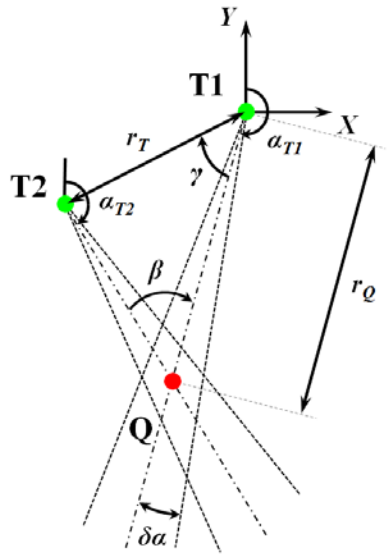

Figure 3.1: A diagram illustrating source localization by triangulation using measurements from sensors T1 and T2 (green circles) separated in space by distance r_T. The origin of the coordinate system is located at sensor T1 and the location of sensor T2 is (X_{T2},Y_{T2}). The source Q (red circle) is located at the intersection of the dash-dotted lines (X_Q,Y_Q) which are defined by the source azimuth angle measured at each sensor (α_{T1} and α_{T2}). r_Q is the distance between T1 and Q, γ is the angle between r_Q and r_T, and $\beta = \alpha_{T1} - \alpha_{T2}$. The polygon bounded by the dotted lines represents the spatial uncertainty of the source location due to uncertainty in the source azimuth measurement ($\delta\alpha$) at each sensor. The azimuth angles α_{T1} and α_{T2} are defined relative to the Y axis.

We have developed a framework which combines aspects of source-sensor orientation and uncertainty in source location with a concentration footprint model to quantify the accuracy of our source determination method at local spatial scales of O(1 km^2). Our source determination method uses in situ, surface level measurements of trace gas concentration and atmospheric turbulence at only two locations as input. The source location is determined by triangulation (Figure 3.1) using coincident measurements of trace gas concentration and wind direction to determine the direction of the source relative to two sensors. Localization of trace gas sources by triangulation has been proposed by Gruber et al (1960) and Henry et al (2002), and is analogous to the technique

of beamforming in signal processing (Chen et al, 2002). After the source location is determined, a concentration footprint model (i.e. an inverse dispersion model) is used to quantify the source strength. Measurements of wind speed, turbulence intensity and atmospheric boundary layer stability quantify the inputs to the concentration footprint model.

The azimuthal direction (α) of a ground level, continuous source of a trace gas relative to a single concentration sensor can be determined from coincident timeseries of concentration and wind direction measurements. Nottrott et al (2013a, 2013b) found that the azimuthal direction of methane (CH_4) sources at ranges upwind of 0.1-5 km could be determined with an uncertainty of approximately ±3° by measuring CH_4 concentration fluctuations as a function of wind direction. Henry et al (2002) partitioned hourly averaged concentration of cyclohexane (C_6H_{12}) by wind direction, and used a nonparametric regression to determine the azimuthal distribution of an upwind source relative to a single concentration sensor. Henry et al (2002) used measurements from two towers, at downwind ranges of 7 km and 10 km, to triangulate the position of C_6H_{12} source with an error of about ±1 km. The angular uncertainty of the source azimuth was reported as ±3° and ±7° at 7 km and 10 km downwind, respectively. Chen et al (2009) and Christen et al (2011) showed that long term variability in wind direction on time scales of days to months permits detection of sources in a nearly 360° azimuthal direction around a measurement location. Thus, the location of a trace gas source at almost any azimuthal location relative to two concentration sensors can be detected from a long measurement record.

After the source location has been determined a concentration footprint model is used to quantify the source-sensor relationship and predict the flux of trace gas from the source. Many different analytical and stochastic footprint models have been developed for the ABL, and an excellent review of those models is presented in Schmid (2002). We used a quasi-analytical concentration footprint model in this paper to illustrate the application of our source determination method, however, the choice of concentration footprint model is not integral to our method.

Mathematical and practical details of the source determination model are described in Section 3.2. The accuracy of the triangulation method for source localization, the effect of uncertain source location on source strength prediction, and an example source determination application are presented in Section 3.3. Applications and limitations of the source determination method are discussed in Section 3.4. Conclusions are summarized in Section 3.5.

3.2 Methodology

3.2.1 Triangulation method for source localization

Eq. 1 describes the location of the source (X_Q,Y_Q) relative to sensors T1 (0,0) and T2 (X_{T2},Y_{T2}) as a function of the source azimuth angles α_{T1} and α_{T2} measured at each sensor (refer to Figure 3.1).

$$\begin{bmatrix} -sin(90° - \alpha_{T1}) & cos(90° - \alpha_{T1}) \\ -sin(90° - \alpha_{T2}) & cos(90° - \alpha_{T2}) \end{bmatrix} \begin{bmatrix} X_Q \\ Y_Q \end{bmatrix} = \begin{bmatrix} 0 \\ Y_{T2}cos(90° - \alpha_{T2}) - X_{T2}sin(90° - \alpha_{T2}) \end{bmatrix} \quad 3.1$$

The solution to Eq. 3.1 represents the intersection of two lines (written here in point-slope notation) that pass through points (0,0) and (X_{T2},Y_{T2}) each having a slope defined by angles α_{T1} and α_{T2}, respectively.

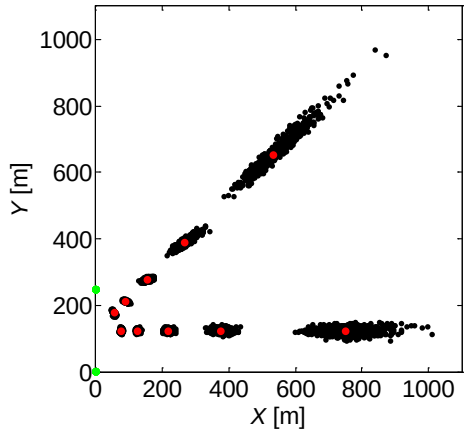

Figure 3.2: Example spatial distributions of Δ (black points) for ten source locations (red points) with $\delta\alpha$ = 1.2° and N = 100. The concentration sensors (green points) are located at (0,0) and (0,250).

Measurements of α naturally contain some error so that the source azimuth angle relative to the sensor is known to $\alpha \pm \delta\alpha$. Uncertainty in α leads to spatial uncertainty in the source location, i.e. the triangulation problem is noisy. We modeled the uncertainty in α using a Monte Carlo method. Values of α_{T1} and α_{T2} corresponding to the true source location $(X_Q,Y_Q)_0$ were taken as the mean values in two independent, random, normal probability distributions $P(\alpha_{T1})$ and $P(\alpha_{T2})$ with standard deviations $\delta\alpha$. The spatial distribution of probable source locations is given by the set $\Delta = \left\{\left(X_Q, Y_Q\right)_n : n \in \boldsymbol{Z} = [1, N]\right\}$. The spatial dispersion of the points in Δ describes the uncertainty in the source location. Δ was generated by solving Eq. 3.1 with N values of α_{T1} and α_{T2} randomly drawn from distributions $P(\alpha_{T1})$ and $P(\alpha_{T2})$. Figure 3.2 shows examples of Δ for ten

different source positions. The spatial uncertainty of the source location increases with source-sensor distance (r_Q).

3.2.2 Concentration footprint model for source strength prediction

We used a concentration footprint model to estimate the source strength (flux) based on the predicted source-sensor locations calculated with Eq. 3.1. For illustrative purposes, we used a quasi-analytical concentration footprint function (η_c) derived from Hsieh et al (2000) and Kormann & Meixner (2001). The model has a simple algebraic formulation, is applicable over the full range of ABL stability conditions, and agrees well with other footprint models. Mathematical details and validation of the model are presented in Appendix A.2. The choice of concentration footprint model is not integral to our source determination method. A more complex footprint model, e.g. a stochastic footprint model based on turbulence parameterizations or large-eddy simulations, could be applied within our source determination framework to improve source strength predictions in complex terrain (see Section 3.4 for further discussion on this point).

The atmospheric concentration measured downwind of a localized source of an arbitrary trace gas is the total concentration (C_T), which is the sum of the background (ambient) concentration (C_b) and the concentration enhancement (C_e) due to emissions from the source, $C_T = C_b + C_e$. The concentration enhancement is calculated by subtracting background concentration from the total concentration, $C_e = C_T - C_b$. C_b can be determined by measuring the concentration upwind of the source (Kaharabata et al, 2000) or by computing the lower envelope of the downwind concentration signal (Vinogradova et al, 2007). The source flux (F) is calculated from the concentration footprint by dividing the mean concentration enhancement ($\overline{C_e}$) by the value of the

concentration footprint function at the source location, $F = \overline{C_e}/\eta_c(x_Q, y_Q, z_m)$. Refer to Appendix A.2 for additional details.

3.2.3 Quantifying error in the source strength prediction due to uncertain source location

Flux and concentration footprint models contain a large amount of uncertainty in practical applications due to various assumptions made in order to achieve closure of model equations. Hsieh et al (2000) and Kljun et al (2002), for example, showed that differences in the crosswind integrated footprint functions among six different footprint models were often > 50% near the peak of the footprint function. The predicted location of the footprint maximum varied significantly between models and was strongly dependent on ABL stability conditions. However, differences between modeled footprints were usually < 20% upwind of the footprint maximum location for all stability conditions.

In light of those differences we assumed that the present concentration footprint function (Section 3.2.2) is perfectly accurate in order to quantify the uncertainty in the source strength calculation due to error in the source localization (Section 3.2.1) independently from errors contained in the footprint model. A set of values describing the relative error in the source strength prediction due to uncertain source location is defined by

$$E = \frac{\eta_c(\Delta', z_m)}{\eta_c\left(\left(X_Q, Y_Q\right)_0', z_m\right)}. \qquad 3.2$$

E is the ratio of η_c at the predicted source locations (Δ) to η_c at the true source location. $\eta_c(x, y, z_m)$ is the concentration footprint function in sensor relative coordinates, $(X_Q,Y_Q)_0$ is the true source location, and the prime superscript indicates a two-

dimensional transformation from absolute spatial coordinates *(X,Y)* to the sensor relative coordinates *(x,y)* of each sensor. The set *E* contains twice as many values as the set *Δ* (i.e. *Δ* contains *N* values and *E* contains 2*N* values), because the probable source locations in *Δ* are projected onto the concentration footprint of both sensors T1 and T2.

3.2.4 Additional constraints in the source determination method

We imposed two additional constraints in the source determination method to exclude spurious solutions that can occur in the context of solving Eq. 3.1 using the Monte Carlo method. The assumption that α_{T1} and α_{T2} can be represented by normal probability distributions $P(\alpha_{T1})$ and $P(\alpha_{T2})$ admits a finite probability of obtaining a spurious or undefined solution to Eq. 3.1. The solution to Eq. 3.1 is spurious if α_{T1} and α_{T2} drawn from $P(\alpha_{T1})$ and $P(\alpha_{T2})$ return a value of $(X_Q,Y_Q)_n$ that lies upwind of the sensors. The solution to Eq. 3.1 is undefined if the source azimuths measured at each tower are equal, i.e. values of α_{T1} and α_{T2} drawn from $P(\alpha_{T1})$ and $P(\alpha_{T2})$ are equal. The probability of a spurious or undefined solution to Eq. 3.1 is <1% for $1.645\delta\alpha < \beta < (180° - 1.645\delta\alpha)$, where 1.645 is the t-distribution critical value for a 90% confidence interval. Thus the source location is set to be undefined when $\beta \leq 1.645\delta\alpha$ or $\beta \geq 180° - 1.645\delta\alpha$. Spurious solutions are excluded from *Δ* when $1.645\delta\alpha < \beta < (180° - 1.645\delta\alpha)$.

If the source is located in a region of low sensitivity within the concentration footprint of either sensor, the source can only be reliably detected by one sensor, only one value of α can be measured, and the source location cannot be determined by

triangulation. Therefore, the source location was determined to be undefined when $\eta_c\left(\left(X_Q, Y_Q\right)_0', z_m\right) / \max[\eta_c(x, y, z_m)] < 0.05$ for either sensor T1 or T2.

3.2.5 Performance assessment

The performance of the source determination method was assessed by parametric analysis. There are four parameters in the triangulation method (Section 3.2.1), and three parameters that determine the concentration footprint (Appendix A.2.1). Figure 3.1 illustrates the four parameters in the triangulation method: r_Q the distance between T1 and Q, r_T the distance between T1 and T2, γ the angle between r_Q and r_T, and $\delta\alpha$ the uncertainty in the source azimuth measurement. The three parameters in the concentration footprint model are z_0 the aerodynamic roughness length, L the Obukhov length, and z_m the measurement height.

The effect of relative source-sensor arrangement and uncertainty in α_{T1} and α_{T2} on the uncertainty in the source location was investigated by varying the parameters r_Q, r_T, γ, $\delta\alpha$. Results are shown for r_T = 0-1000 m; γ = 0-180°; r_Q = 0-1000 m. $\delta\alpha$ = 1.2°, 2.4° corresponding to 99% confidence intervals of $\delta\alpha \approx 3°$ and 6° (consistent with Henry et al, 2002; Nottrott et al, 2013b). z_m = 10 m and z_0 = 0.05 m corresponding to long grassy ground cover and farmland (Stull, 1988). N = 100 in the Monte Carlo method.

The error in the source strength prediction (E; Eq. 3.2) is generally a function of the spatial uncertainty of the source location, and the gradient of the concentration footprint function in the region of the true source location. The functional dependence of E on the gradient of the concentration footprint function was studied for different ABL stability conditions by varying L. Four different ABL stability conditions were simulated: strongly unstable (B3), forced convection (SB2), neutral stratification (N) and stable

stratification (S). Values of surface sensible heat flux $\left(\overline{w'\theta'}\right)_0$, surface shear stress u_*, Obukhov length L, surface wind speed $\bar{u}(10\text{ m})$ and crosswind horizontal r.m.s. velocity fluctuation $\hat{v}$ for each simulation are listed in Table 3.1.

Table 3.1: Values of surface sensible heat flux $\left(\overline{w'\theta'}\right)_0$, surface shear stress u_*, Obukhov length L, surface wind speed $\bar{u}(10\text{ m})$ and crosswind horizontal r.m.s. turbulent velocity fluctuation $\hat{v}$ for the four ABL stability cases. $\left(\overline{w'\theta'}\right)_0$, u_* and L for cases B3, SB2, N and S are based on data from large-eddy simulations of Nottrott et al (2014) and Beare et al (2006). $\bar{u}(10\text{ m})$ was calculated from Eq. A.2.5. $\hat{v}$ was calculated from Eq. A.2.6 with z_i = 1000 m for cases B3 and SB2.

Name	$\left(\overline{w'\theta'}\right)_0$ **[m K s^{-1}]**	u_* **[m s^{-1}]**	L **[m]**	$\bar{u}(10\text{ m})$ **[m s^{-1}]**	$\hat{v}$ **[m s^{-1}]**
B3	0.050	0.12	-2.7	1.0	1.0
SB2	0.10	0.49	-110	6.0	1.4
N	0	0.60	-∞	7.8	1.1
S	-0.012	0.26	96	3.7	0.46

3.3 Results

3.3.1 Uncertainty of source location

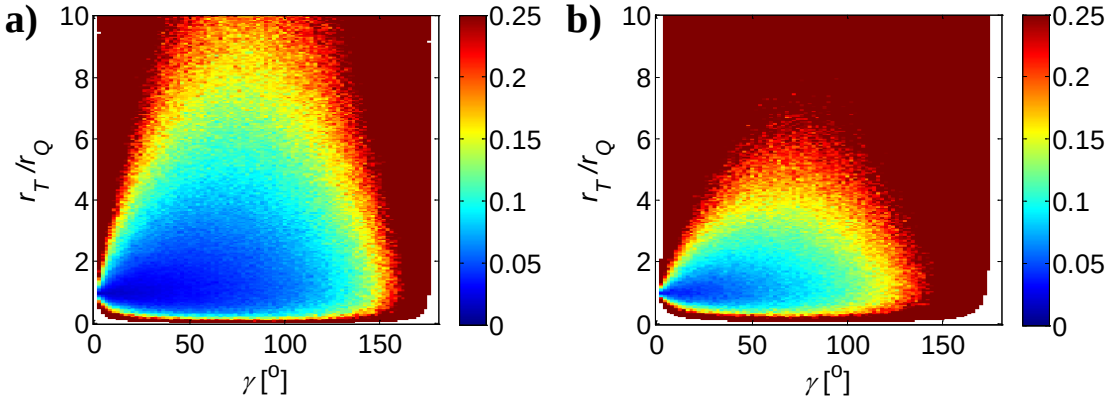

Figure 3.3: The absolute spatial uncertainty of the source location normalized by the source-sensor distance, plotted for different source-sensor arrangements for azimuth angle uncertainty **a)** $\delta\alpha$ = 1.2° and **b)** $\delta\alpha$ = 2.4°. The color scale shows median($||\Delta||$)/ r_Q (the median Euclidian distance of the points in set Δ normalized by r_Q) as a function of γ and r_T/r_Q (see Figures 3.1 and 3.2). White areas correspond to parameter combinations for which the source location cannot be determined due to the conditions described in Section 3.2.4.

The uncertainty of the source location is quantified by the spatial dispersion of the set Δ. A length scale that describes the absolute spatial uncertainty of the source location is defined by median($||\Delta||$). Figure 3.3 shows median($||\Delta||$)$/r_Q$ as a function of γ and r_T/r_Q (see Figure 3.1 for explanation of the variables). median($||\Delta||$)$/r_Q$ is a useful metric for the error in the source localization because it quantifies the magnitude of the spatial uncertainty of the source location relative to the source-sensor distance. median($||\Delta||$)$/r_Q$ is self-similar in γ and r_T/r_Q for the geometry shown in Figure 3.1 by the property of similar triangles. However, the number of parameter combinations for which the source location cannot be determined (i.e. the white areas in Figure 3.3) depends on $\delta\alpha$ and $\underline{z_m}$ because of the constraints described in Section 3.2.4. Noise in Figure 3.3 is due to finite sample size $N = 100$ in the Monte Carlo method and is proportional to $N^{-1/2}$.

The advantage of the self-similar solution is that the spatial uncertainty of the source location can be determined for all possible source-sensor configurations using the data in Figure 3.3. Figure 3.3 shows that the source location can be determined to < 10% of the source-sensor distance r_Q for a wide range of source-sensor arrangements. The uncertainty in the source location is large for small values of r_T/r_Q and large values of γ, because the lines defined by α_{T1} and α_{T2} are nearly parallel, i.e. β is only slightly larger than $\delta\alpha$ (refer to Figure 3.1).

The magnitude of median($||\Delta||$)$/r_Q$ is proportional to $\delta\alpha$ by the arc length formula for a circle, i.e. the uncertainty in the source location scales linearly with $\delta\alpha$. Figure 3.4 confirms that median($||\Delta||$)$/r_Q$ is approximately twice as large for $\delta\alpha = 2.4°$ compared to 1.2°.

The azimuthal direction of the source (α) can only be measured by both sensors if the variation in the mean wind direction (μ) is sufficient to carry the trace gas emitted from the source toward each tower. The change in μ required to measure α at both sensors is plotted in Figure 3.5 as a function of γ and r_T/r_Q. Values of $\mu > 100°$ have been observed at many locations over monthly and seasonal intervals, although the actual value of μ is site specific.

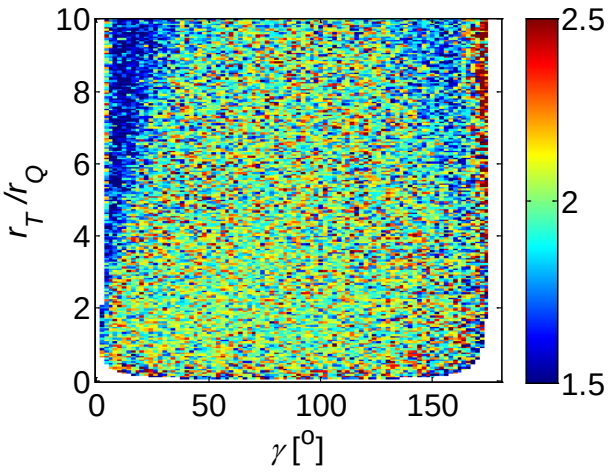

Figure 3.4: The ratio of median($||\Delta||$)/r_Q for $\delta\alpha$ = 2.4° to 1.2°. The median value of the data in Figure 3.4 is 2.00 and the standard deviation is 0.05.

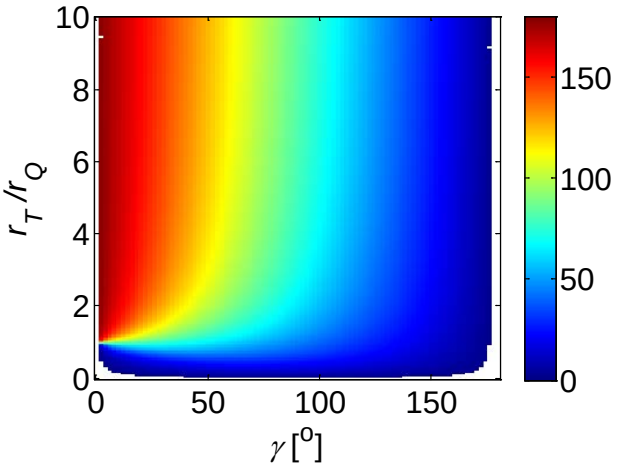

Figure 3.5: The change in mean wind direction μ [°] required to measure α at both sensors as a function of r_T/r_Q and γ.

3.3.2 Impact of uncertain source location on source strength prediction

Uncertainty in the source location causes errors in the source strength prediction (Section 3.2.3, Eq. 3.2), because the exact location of the source within the concentration footprint of the sensor is not known. We quantified the relative error of the source strength prediction by the median absolute deviation of the set *E*, MAD(*E*-1). It is important to note, however, that the quantity MAD(*E*-1) does not account for uncertainty in the source strength due to errors in the concentration footprint model. Figure 6 shows the quantity MAD(*E*-1) for atmospheric boundary layer conditions ranging from strongly convective to stable. MAD(*E*-1) is approximately proportional to absolute spatial uncertainty of the source location median($||\Delta||$), so that greater uncertainty in the source location leads to greater errors in the source strength prediction. MAD(*E*-1) is correlated with the spatial gradient of the concentration footprint $\left[(\partial_x \eta_c)^2+\left(\partial_y \eta_c\right)^2\right]^{1/2}$, where ∂_x and ∂_y indicate spatial derivatives in the *x* and *y* directions, respectively. Therefore, the error in the source strength prediction depends on the relative location of the source within the sensor footprint and the ABL stability condition. The data in Figure 6 show that relative error in the source strength prediction is <10% for most source-sensor arrangements. It is important to realize that MAD(*E*-1) is a function of the concentration footprint (Appendix A.2, Eq. A.2.3b), and therefore is not self-similar in r_Q and $\delta\alpha$.

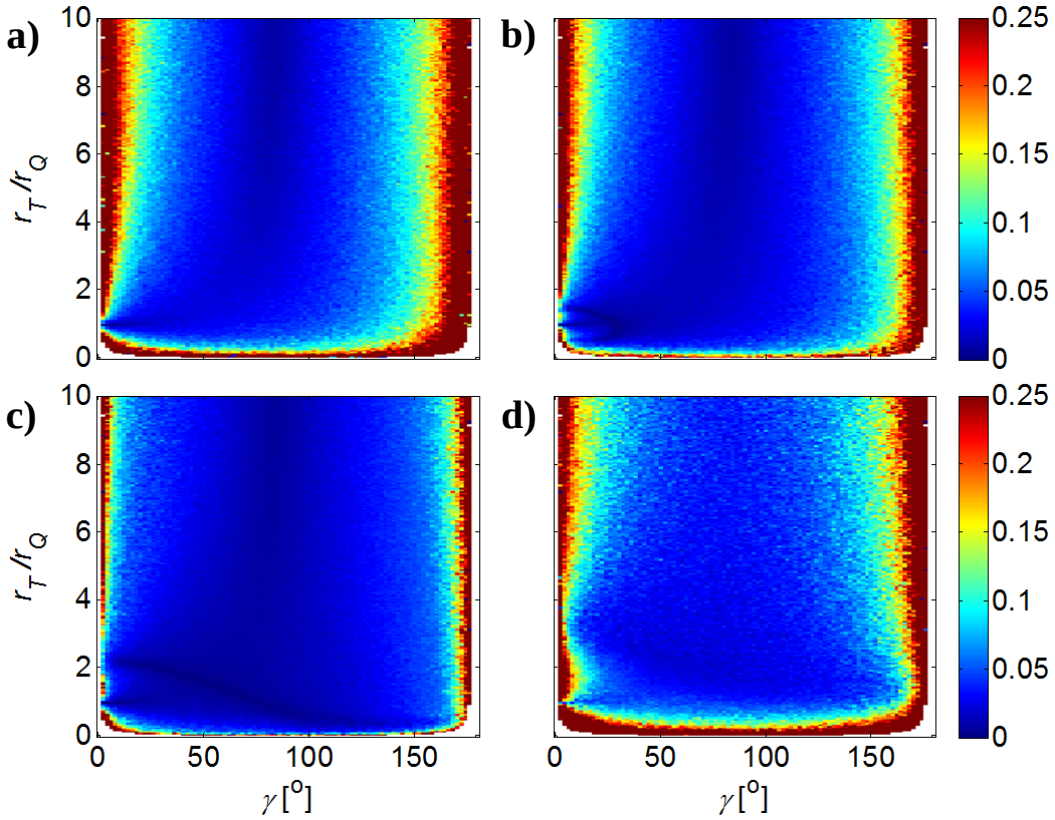

Figure 3.6: The relative error in the source strength prediction due to uncertainty in the source location plotted for different source-sensor arrangements for ABL stability cases **a)** B3, **b)** SB2, **c)** N, and **d)** S. The color scale shows MAD(E-1), the median absolute deviation of the set E-1, plotted as a function of r_T/r_Q and γ. Refer to Table 3.1 for descriptions of the different stability cases. Noise in Figure 3.6 is due to finite sample size N = 100 in the Monte Carlo method. White areas correspond to parameter combinations for which the source location cannot be determined due to the conditions described in Section 3.2.4.

3.3.3 Source determination example

Figures 3.7 and 3.8 show output of the source determination method in X and Y spatial coordinates (see Figure 3.1) for an example sensor configuration with z_m = 10 m, r_T = 250 m, $\delta\alpha$ = 1.2°. Figure 3.7 shows the uncertainty of the source location, and the required variation of the mean wind direction to detect the source at both sensors. Figure 3.7a indicates that the source location can be determined with acceptable accuracy (i.e. median($||\Delta||$) << r_Q) for a large spatial area surrounding the sensor locations. Figure 3.7b

shows that the required variation of the mean wind direction for source detection is generally < 45° for this particular sensor configuration.

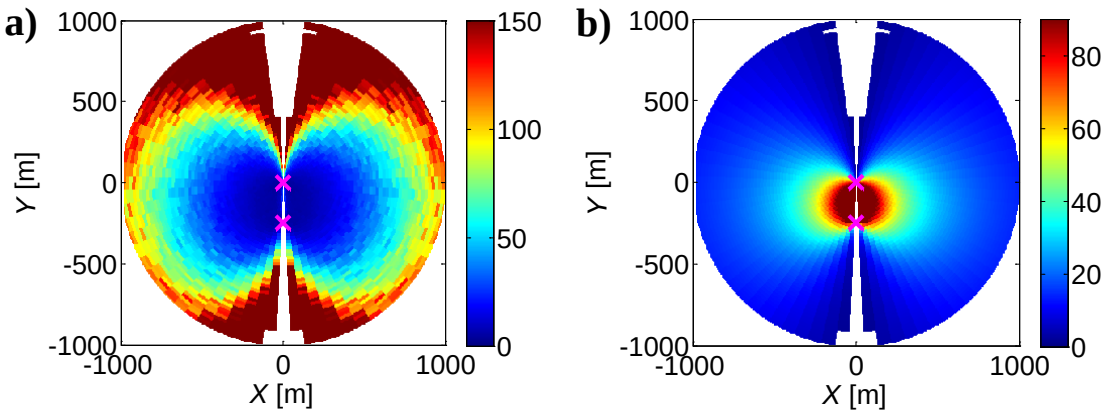

Figure 3.7: a) Absolute spatial uncertainty of the source location, median($||\Delta||$) [m], and **b)** required variation in mean wind direction μ [°] plotted as a function of sensor relative spatial coordinates X and Y (as defined in Figure 3.1 with the origin at T1) for an example sensor configuration. z_m = 10 m, r_T = 250 m, $\delta\alpha$ = 1.2° and r_Q = 0-1000 m. Magenta crosses correspond to the location of sensors T1 and T2. White areas in the region $(X^2+Y^2)^{1/2}$ < 1000 m correspond to parameter combinations for which the source location cannot be determined due to the conditions described in Section 3.2.4.

Figure 3.8 shows the percent error in the source strength prediction due to uncertainty in the source location. MAD(E-1) < 20% in forced convection ABL conditions (Figure 3.8a) for the region where median($||\Delta||$) << r_Q. MAD(E-1) < 10% for median($||\Delta||$) << r_Q in stable ABL conditions (Figure 3.8b). However, it is expected that the concentration footprint function used in this paper (Appendix A.2.1) will be least accurate for the stably stratified ABL due to strong anisotropy of the turbulent velocity field (Sarkar, 2003) and enhanced plume meandering (Etling 1990).

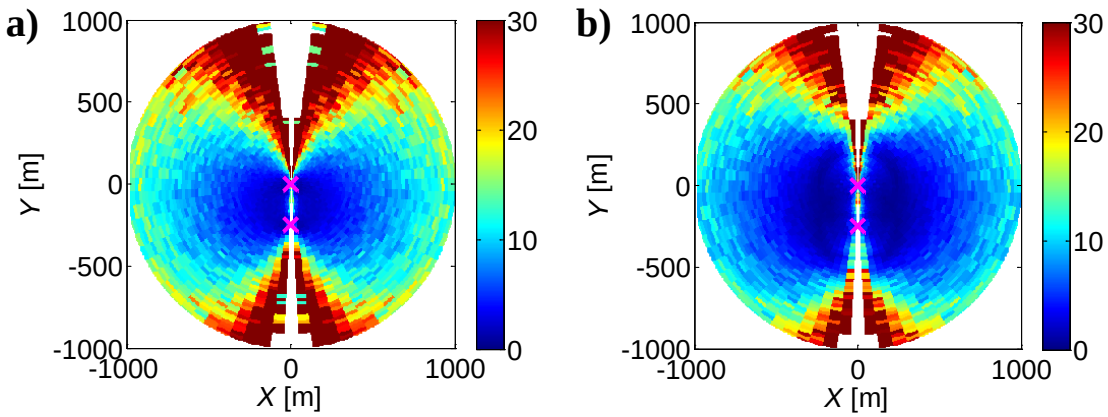

Figure 3.8: Percent error in the source strength prediction due to uncertainty in the source location, MAD(*E*-1) [%], for stability cases **a)** SB2 and **b)** S. The source/sensor parameters are the same as in Figure 3.7. Refer to Table 3.1 for descriptions of the different stability cases.

3.4 Discussion and conclusions

The proposed source determination method provides a useful, practical framework for predicting the location and strength of a priori unknown trace gas sources from concentration and turbulence measurements at two locations. Remarkable features of the method are the use of only two sensors to monitor a large geographic area O(1 km^2), and the application of a concentration footprint rather than a flux footprint (as in Lewicki & Hilley, 2012) to quantify the source strength. There are several advantages of using the concentration footprint instead of the flux footprint for source determination. The upwind extent of the concentration footprint for a given sensor is much larger than the flux footprint. For example, Kljun et al (2002) showed that, for a sensor located 50 m above ground level (AGL), the upwind extent of the 50%-level source area for the concentration footprint is more than two times greater than that of the flux footprint. Measurements of mean concentration at the sensor location can be used to estimate source strength from a concentration footprint, while measurements of the vertical

concentration flux are necessary to determine source strength from the flux footprint. Measurement of vertical concentration flux requires high frequency temporal sampling (Kaimal & Finnigan, 1994) and increases the cost and complexity of the measurement system.

The lowest cost measurement system includes two concentration sensors with 1 Hz sampling capability, a two-dimensional ultrasonic anemometer, a pyranometer and an infrared radiometer. Wind direction and concentration measurements are used to compute the source azimuth relative to each sensor (α_{T1} and α_{T2}). Wind speed, solar radiation and downwelling longwave radiation are used to parameterize daytime ABL stability conditions for the concentration footprint model with the Pascal-Gifford stability classes (Hanna et al, 1982). Although the Pascal-Gifford stability classes only provide an approximate empirical characterization of ABL stability conditions, it is expected that such a classification would be sufficient in light of large uncertainties in flux and concentration footprint models (see Appendices A.2.1 and A.2.2). An eddy-covariance system consisting of a three-dimensional, ultrasonic anemometer and an open-path, infrared gas analyzer (to correct sonic temperature fluctuations for water vapor effects) for direct measurement of u_* and L could be used for more accurate characterization of ABL stability, however, at significantly greater cost. Wind and ABL stability measurements at both concentration sensors may be required if r_T is large, or if significant terrain or vegetation is present in the vicinity of the concentration sensors. The ability to detect low concentration sources or sources located far upwind of the sensor is limited by the sensitivity and precision of the instrument, which determines the ability to resolve concentration enhancements above the background concentration level.

The triangulation method for source localization (Section 3.2.1) has a self-similar solution that quantifies the uncertainty in the source location for any given source-sensor geometry (Figure 3.3). Uncertainty in α_{T1} and α_{T2} was modeled using independent, random normal probability distributions $P(\alpha_{T1})$ and $P(\alpha_{T2})$. That approach does not account for any systematic bias in measurements of α_{T1} and α_{T2}. A systematic bias could be caused by large roughness elements (e.g. trees, buildings, terrain, etc.) between the source and sensor that distort the wind and trace gas concentration fields, or if $r_Q >> r_T$.

The magnitude of $\delta\alpha$ (i.e. the uncertainty in α) depends on a number of factors including the measurement frequency, length of the measurement period, source-sensor distance and terrain. Nottrott et al (2013a, 2013b) showed that using metrics of fluctuating trace gas concentration (e.g. intermittency factor or 99^{th} percentile concentration enhancement) rather than mean concentration can improve estimates of α and reduce the magnitude $\delta\alpha$. At long distances downwind from the source the crosswind horizontal plume width (σ_y) approaches the distance between the concentration sensors (r_T), which may cause the magnitude of $\delta\alpha$ to increase with increasing source-sensor distance. A standard Gaussian plume model (Hanna et al, 1982) predicts $\sigma_y \approx 180$ m for forced convective conditions and $\sigma_y \approx 40$ m for stable stratification at 1000 m downwind of the source. That calculation suggests that, although Figure 8 indicates that the accuracy of the source strength prediction is <15% for most sources at $(X^2+Y^2)^{1/2} \approx 1000$ m, in practice the source strength uncertainty may be larger for sources at upwind ranges ≥ 1000 m. The data of Henry et al (2002) also support this claim. This problem could be alleviated by increasing r_T.

The assumption that the concentration footprint function used in this paper (Section 3.2.2) is perfectly accurate provides a means to quantify uncertainty in the source strength calculation that is caused by uncertainty in the source location, independently from errors contained in the footprint model. We used a simple quasi-analytical footprint model for illustrative purposes. However, the choice of concentration footprint model is not integral to the general source determination method. In reality the total error in the source strength prediction also depends on errors contained in the concentration footprint model. The accuracy of the concentration footprint model depends on ABL stability conditions, and is degraded by inhomogeneous surface characteristics like terrain and vegetation (Finnigan, 2004). The contribution of the error in the footprint function to the total error in the source strength prediction should be assessed with ensemble statistics from different footprint models and experiments. We have shown that flux and concentration footprints calculated with different models vary considerably (Appendix A.2.2). Although a number of flux footprint models have been compared with experimental data (e.g. Hsieh et al, 2000; Kljun et al, 2004; Lewicki & Hilley, 2012), to the knowledge of the authors, no such comparisons have been made for concentration footprints.

Figure 3.3 quantifies the ability of the source determination method to resolve individual sources when multiple sources are present in the sensor footprint. Individual sources can be resolved with 99% confidence if they are separated by a distance of $2 \cdot \text{median}(||\Delta||)/r_Q$. That distance is directly proportional to $\delta\alpha$ (Section 3.3.1, Figure 3.4). In practice, however, crosswind horizontal dispersion may cause plumes from nearby sources to merge downwind, making measurement of unique values of α_{T1} and α_{T2}

difficult. That issue could be mitigated by measuring at night when crosswind dispersion of the instantaneous plume is minimal. However, Etling (1990) observed that plume meandering in the crosswind horizontal direction is enhanced in the stable ABL which may cause de-correlation between the observed wind direction and source azimuth. Two nearby sources with very different source strengths will be difficult to resolve using the proposed source determination method, because emissions from a source with a high emissions rate or large spatial extent may overpower emissions from a smaller source in the concentration signal measured downwind.

Acknowledgement

The content of Chapter 3 has been submitted for publication in Nottrott A., Rahn T., Keeling R., Kleissl J., Dubey M., 2014, Triangulation method for source determination at local spatial scales, Submitted to *Atmospheric Environment*. Anders Nottrott was the principal investigator and first author of this publication.

4. Top-down emissions quantification using atmospheric measurements from a methane controlled release experiment

4.1 Introduction

4.1.1 Motivation

A large scale, outdoor, controlled release experiment to measure methane (CH_4) emissions from quasi-point sources at local spatial scales O(0.01 – 1 km^2) was completed in June, 2013 (Arata et al 2013; Aubrey et al 2013; Dubey et al 2013; Nottrott et al 2013b). The purpose of the experiment was to evaluate and demonstrate capabilities of in situ and airborne remote sensor technologies for top-down emission quantification in a realistic environment. Top-down estimates use atmospheric measurements of GHG concentration to directly quantify GHG emissions from a priori unknown sources (see Section 1.2.3). In this chapter surface-level, in situ measurements from fast response concentration sensors will be used to demonstrate the feasibility of the top-down source determination model developed in Chapter 3. The two main components of the source determination model of Chapter 3 are the determination of the source location by triangulation (Section 3.2.1), and prediction of the source strength using a concentration footprint model (Section 3.2.2). The error associated with each of those components was evaluated in the context of field measurements.

4.1.2 Literature review

The accuracy of the source localization depends on the ability to calculate the azimuth angle of a fugitive emissions source relative to a concentration sensor using coincident wind direction and concentration measurements. Henry et al (2002) partitioned hourly averaged concentration of cyclohexane (C_6H_{12}) by wind direction, and

used a nonparametric regression to determine the azimuthal distribution of an upwind source relative to a single concentration sensor. Henry et al (2002) used measurements from two towers, at downwind ranges of 7 km and 10 km, to triangulate the position of C_6H_{12} source with an error of about ±1 km. The angular uncertainty of the source azimuth was reported as ±3° and ±7° at the 7 km and 10 km downwind towers, respectively. Nottrott et al (2013a) found that the azimuthal direction of CH_4 sources at ranges of 1-5 km could be determined with an uncertainty of approximately ±3° by measuring the 99^{th} percentile CH_4 concentration enhancement distribution as a function of wind direction. The accuracy of the source azimuth calculation using the 99^{th} percentile CH_4 concentration enhancement distribution was evaluated using experimental data (Sections 4.2.7 and 4.3.2).

The accuracy of the source strength prediction depends on the uncertainty in source location and the accuracy of the concentration footprint model. The impact of uncertain source location on the source strength prediction was evaluated in Section 3.3.2. Flux and concentration footprint models contain a large amount of uncertainty in practical applications due to the various assumptions requred to achieve closure of model equations. Many previous studies have validated flux footprint models against measured data (e.g. Flesch et al, 1995; Hsieh et al, 2000; Lewicki & Hilley, 2012), however, no such comparisons have been made for concentration footprint models, to the knowledge of the author. The accuracy of the quasi-analytical concentration footprint model described in Appendix A.2 was evaluated using experimental data.

The controlled release experiment described in this chapter was unprecedented in scope, and type and density of instrumentation. Previous outdoor controlled release

experiments have investigated the effects of turbulence on timeseries of surface-level, point measurements of scalar concentration (Hanna & Insley, 1989; Mylne & Mason, 1991). Hanna & Insley (1989) reviewed data from six laboratory and outdoor controlled release experiments in near neutral to convective atmospheric stability. They studied energy spectra of concentration timeseries, and cross-spectra for coincident concentration and turbulent wind measurements at frequencies up to 1 Hz. They observed strong correlation between collocated measurements of the crosswind horizontal turbulent velocity component and trace gas concentration at the Eulerian timescale of turbulence. Mylne & Mason (1991) measured concentration on vertical and horizontal arrays at 50 to 1000 m ranges downwind of a controlled release from a quasi-point source in near neutral to weakly convective conditions. They proposed a method to enhance the frequency content of fast response concentration measurements that are subject to inherent filtering caused by instrument design. Mylne & Mason (1991) found that the probability distribution of concentration timeseries could be approximated by a clipped-normal probability distribution function (PDF). However, Yee and Chan (1997) showed that a clipped-gamma PDF provides a better representation of low order statistics of concentration timeseries in the atmospheric boundary layer. None of these studies investigated the relationship between concentration fluctuations and source direction.

Details of the design and setup of the controlled release experiment are provided in Sections 4.2.1 and 4.2.2. Data quality control and post processing are described in Sections 4.2.3 through 4.2.6. A method for determining the azimuth of fugitive emissions sources using atmospheric measurements is described in Section 4.2.7. Results and discussion are presented in Sections 4.3 and 4.4, respectively.

4.2 Methodology

4.2.1 Experiment location

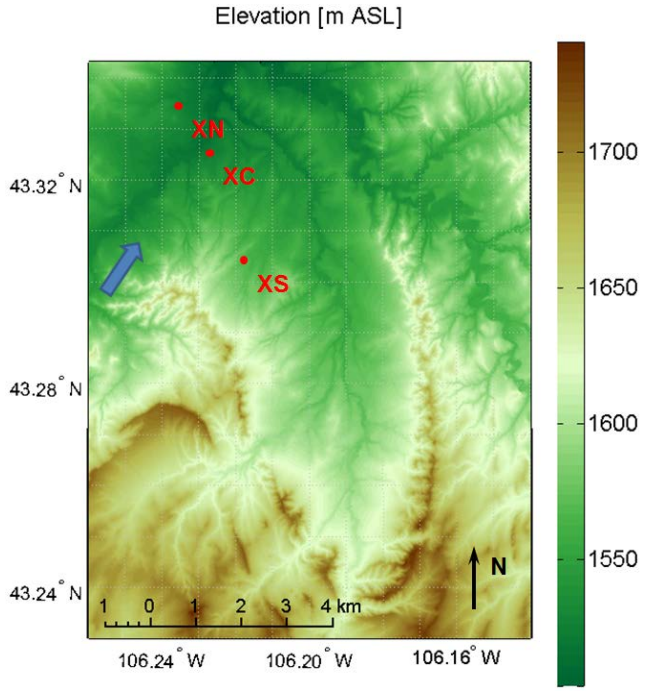

Figure 4.1: A topographic map of the Rocky Mountain Oil Field Test Center (RMOTC) area. Controlled release locations are marked by red points, and the predominant wind direction is indicated by the blue arrow (see Figure 4.2). Data from the site labeled XS is presented in this chapter. The resolution of the map is 1.3 arc-seconds (~5 m). Topographic data was obtained from the USGS National Elevation Dataset (NED).

The controlled release experiment was conducted in June 2013 at the U.S. Department of Energy, Rocky Mountain Oilfield Test Center (RMOTC), approximately 60 miles north of Casper, WY. The RMOTC facility is a large area of approximately 12 km^2 set in a basin which is surrounded by low hills to the southwest and southeast (Figure 4.1). Controlled release experiments were located in the northern part of RMOTC to minimize wake turbulence generated by terrain and interference from petroleum extraction operations occurring in the southern part of the RMOTC facility. Data from the site labeled XS (Figure 4.1) is included in this chapter. The experiment was planned for June based on a high probability of favorable wind and weather conditions. Figure 4.2

shows the climatology of wind speed and direction for the RMOTC area during the month of June obtained from the National Oceanographic and Atmospheric Administration (NOAA) hourly average data Aviation Digital Data Service (ADDS).

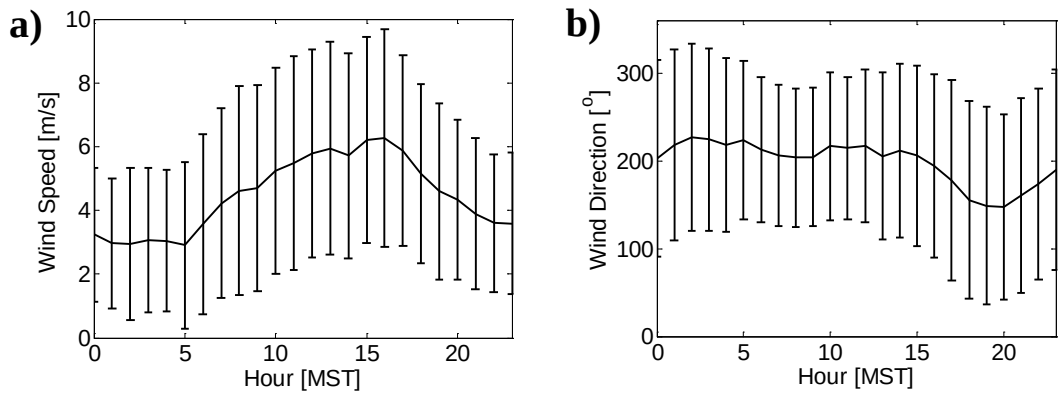

Figure 4.2: Climatology of **a)** wind speed and **b)** direction at the Casper/Natrona International Airport near Casper, Wyoming U.S.A. The climatology includes 6 years of hourly averaged wind data obtained from the National Oceanographic and Atmospheric Administration (NOAA) hourly average data Aviation Digital Data Service (ADDS). Vertical error bars indicate the standard deviation of the data.

4.2.2 Experiment design

The experiment was conducted during a seven day period between June 20th and 26th, 2013. The controlled release rate of CH_4 was different on each day, varying from 15-5000 scf hr^{-1} (0.80-26 g s^{-1}). Figure 4.3 shows a schematic of the experiment setup. CH_4 gas was released from a diffuser, which was designed to simulate fugitive methane emissions from natural gas extraction and transmission infrastructure. Two 15 m high towers were arrayed downwind of the release location. The CH_4 supply for the experiment was stored in liquid form inside a large tube trailer. Compressed CH4 was passed through an expansion regulator that was outfitted with a heat exchanger to ensure that gas was emitted from the diffuser at the ambient air temperature.

The diffuser distributed the CH_4 source over an approximately 1 m^2 area, and ensured that the gas flowing from the source was in isokinetic equilibrium with the surrounding fluid (Figure 4.4a). CH_4 gas was supplied to the diffuser through a 90 m long inlet hose, so that the relative location of the release point and towers could adjusted for variable wind conditions. The CH_4 flux was measured using an Onicon Inc. F-5100 thermal mass flow meter which has a measurement accuracy of ±2%.

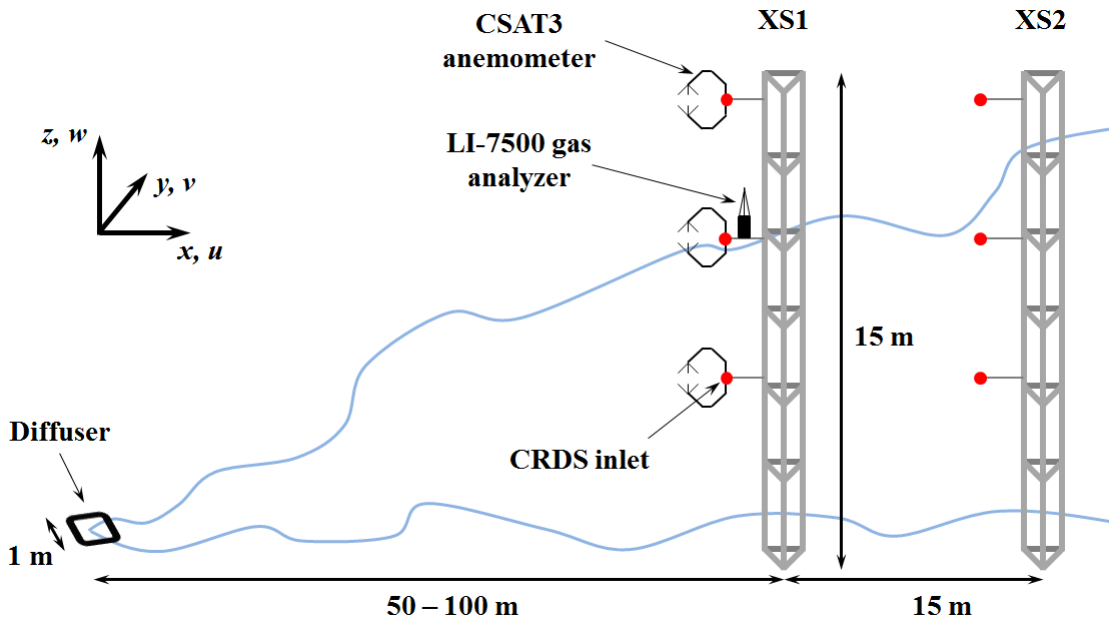

Figure 4.3: A schematic of the experiment setup. The coordinate system is aligned so that the streamwise velocity component (u) is along the x-axis, the crosswind horizontal velocity component (v) is along the y-axis, and the vertical velocity component (w) is along the z-axis. The diagram is not drawn to scale. The blue line represents the instantaneous edge of the CH_4 plume. Photographs of the experiment setup are shown in Figure 4.4.

Turbulent wind measurements and high frequency CH_4 concentration measurements were made on two 15 m high towers located 50-120 m downwind of the release location (Figures 4.4b). The upwind tower (XS1) was instrumented with three Campbell Scientific CSAT3 3-dimensional ultrasonic anemometers, a Licor LI-7500 open path CO_2/H_2O gas analyzer, and a Picarro G2311-f fast response cavity ring-down

spectrometer (CRDS) for CO_2, CH4 and H_2O concentration measurements. The downwind tower (XS2) was only instrumented with a Picarro G2311-f CRDS. Inlets for the Picarro CRDS were placed a three different heights on both towers. Table 4.1 lists the configuration of each tower. The CSAT3 anemometers and LI-7500 gas analyzer were sampled at 20 Hz using a Campbell Scientific CR5000 datalogger. The Picarro CRDS sensors include onboard data logging capabilities and were sampled at 10 Hz. Air temperature (Campbell Scientific T107), and shortwave and longwave components of upwelling and downwelling radiation (Kipp & Zonnen CNR 4 Net Radiometer) were measured on a tripod approximately 250 m upwind of the XS1 tower at heights 2 m AGL and 5.75 m AGL, respectively. Ground surface temperature was measured over an area of approximately 3.1 m^2 using and Apogee SI-111 infrared radiometer. Air temperature, net radiation and surface temperature were sampled at 1 Hz and averaged on a 1 minute interval. All sensors were calibrated according to manufacturer specifications prior to field deployment.

Geographic coordinates of controlled release locations and towers were measured using a Trimble Geo 7X handheld GPS unit. ESRI ArcMap software was used to map and calculate the relative locations of controlled release points and towers. The spatial uncertainty of those calculations was <1 m. Refer to Table 4.2 for information on the relative locations of controlled release points and towers.

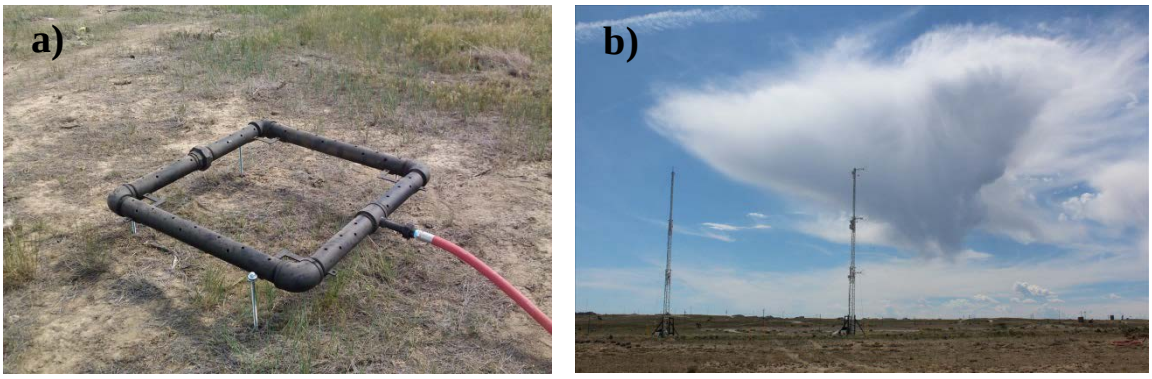

Figure 4.4: Photographs of **a)** the diffuser and **b)** measurement towers during the experiment. The XS1 tower is on the right in Figure 4.4b, and the predominant wind direction was from left to right.

Table 4.1: Configuration of towers during the controlled release experiment. Sensor heights are listed in meters above ground level (AGL). Refer to Figure 4.3 for the layout of the experiment setup.

	XS1			XS2		
CSAT3 [m]	4.75	8.93	12.89	-	-	-
LI-7500 [m]	-	8.81	-	-	-	-
CRDS inlet [m]	4.50	8.66	12.56	4.60	8.49	12.57

4.2.3 Data quality control

All data were carefully quality controlled. Instruments were inspected and cleaned daily to ensure that measurements were not degraded by dust or moisture, and care was taken to minimize interference from personnel, vehicles and wildlife. Both the CR5000 datalogger and the CRDS incorporate a number of automated tests for data quality and flag bad data. All flagged data were excluded from the analysis. Additional post processing tests for data quality included visual inspection of raw data and sensor inter-comparison.

4.2.4 Post processing of ultrasonic anemometer data

The CSAT3 ultrasonic anemometers were leveled in the field by visual inspection, and a tilt correction algorithm (Wilczak et al, 2001) was applied in post processing to ensure that the means of the vertical (w) and crosswind horizontal (v)

velocity components were zero over integral time periods. The integral time period was calculated from z_i/u_*, where z_i is the boundary layer height and u_* is the measured friction velocity (refer to Section 1.3.2). The boundary layer height was estimated from energy spectra of surface-level, turbulent velocity fluctuations (Liu and Ohtaki, 1997). Sonic temperature was corrected for water vapor in the air with data from the LI-7500 using the methods described in Schotanus et al (1883) and Kaimal et al (1991). The compass alignment of the ultrasonic anemometers was measured using a Brunton pocket transit device with an accuracy of about ±1°, assuming a magnetic declination of +9.5° for the RMOTC location (Maus et al, 2010).

Corrected data from the sonic anemometers were used to compute the turbulent momentum fluxes ($\overline{u_i{}'u_j{}'}$, where $i,j \in \boldsymbol{Z} = [1,3]$), sensible and latent heat fluxes ($\overline{w'\theta_v{}'}$ and $\overline{w'q'}$), and the Obukhov length (Eq. 1.8b). Those quantities were used as inputs to the concentration footprint model (refer to Appendix A.2).

4.2.5 Post processing of CRDS concentration data

The Picarro G2311-f CRDS samples CO_2, CH_4 and H_2O concentration at approximately 10 Hz, however, measurements are not triggered on a regular interval so the actual sampling rate varies between approximately 9 Hz and 13 Hz. The output data from the CRDS was linearly interpolated to a 10 Hz interval in post processing to obtain a timeseries with a regular samping rate. The interpolated 10 Hz concentration data were used in the analysis presented here. Data from the CR5000 datalogger and the CRDS analyzer were not synchronized because they were measured on different platforms. The time lag for the CRDS system relative to the CR5000 datalogger was determined from the maximum cross-correlation between timeseries of CH_4 concentration (c_{CH4}) measured

with the CRDS, and the turbulent components of vertical velocity and virtual potential temperature (w' and θ_v') measured with the CSAT3.

The CH_4 concentration measured downwind of the controlled release is the total concentration (c_T) which is the sum of the background (ambient) concentration (c_b) and the concentration enhancement (c_e) due to the controlled release source.

$$c_T = c_b + c_e \tag{4.1}$$

A background detection algorithm was developed to determine the minimum envelope of the measured concentration timeseries and calculate the concentration enhancement. The background concentration was determined by sampling a subset of the concentration timeseries using a sliding time window. The window size was chosen to be several times larger than the Eulerian timescale of crosswind velocity fluctuations ($T_{E,v}$) in order to capture a representative sample of concentration measurements (consistent with the observations of Hanna & Insley, 1989). The background concentration was defined to be the mode of the concentration measurements within the sliding window. The choice of the mode for the value of background concentration is based on the work of Yee & Chan (1997) who showed that the probability distribution of surface-level, scalar concentration measurements downwind of a localized source can be represented by a clipped-gamma distribution function. Thus, the most probable value of measured concentration is defined by the mode of the distribution. And the most probable measured concentration value is associated with the background due to the high level of intermittency in the measured timeseries (see Section 2.3.6). Figure 4.5 illustrates that the method described above is robust, and correctly identifies both large and small concentration fluctuations above the

background level. The concentration enhancement is calculated as $c_e = c_T - c_b$ and any negative values are set to zero.

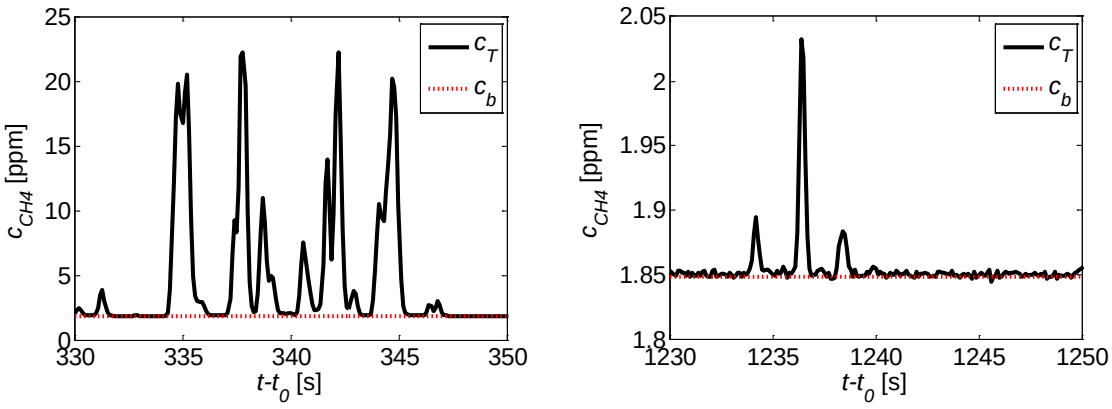

Figure 4.5: Timeseries of CH_4 concentration measured at XS1, 4.50 m AGL on the afternoon of June 23rd, 2013. The black line is the total concentration (c_T), and the red dashed line is the calculated background concentration (c_b). The average background concentration was 1.851 ppm. Units of the horizontal axis are relative time since the beginning of the measurement period.

The CRDS output inherently contains some filtering of the true concentration signal which is caused by of the physical design of the CRDS system. The transfer function between the true 10 Hz concentration signal and the output signal from the CRDS is difficult to quantify because it is a function of parameters like inlet line length, cavity size, cavity shape, optical properties of mirrors and fiber optics. That issue is common in closed path spectroscopy. Mylne and Mason (1991) used a first order, autoregressive sharpening filter to approximate the instrument filtering transfer function and increase the high frequency gain of the output signal.

$$c_n = \frac{(\epsilon - 1)c'_{n-1} + c'_n}{\epsilon} \qquad 4.2$$

c_n is the true concentration for the n^{th} measurement and c'_n is the n^{th} concentration measurement output by the CRDS. The sharpening coefficient (ϵ) varies between 0 and

1, and was determined from empirical tuning to be 0.77 for the instrument at XS1 and 0.73 for the instrument at XS2. According to the Nyquist-Shannon sampling theorem, 10 Hz sampling rate using a perfect concentration sensor would be required to attain 5 Hz temporal resolution of the concentration signal. The application of the sharpening filter in Eq. 4.2 to 10 Hz atmospheric data measured with the Picarro G2311-f CRDS indicates that the inherent filtering of the CRDS results in an actual temporal resolution of approximately 2 Hz rather than the ideal value of 5 Hz (Appendix A.3.1). That result suggests that the response time of the Picarro G2311-f CRDS may be insufficient for eddy covariance measurements in the atmospheric surface layer.

4.2.6 Measurement periods

Six measurement periods were selected for detailed analysis. Criteria for acceptable measurement periods were high data quality, continuous data availability over several integral time periods and quasi-steady atmospheric stability conditions. Measurement periods and experiment parameters for each tower are listed in Table 4.2.

Table 4.2: List of measurement periods selected for analysis, and experiment parameters during each measurement period. t_m is the length of the measurement period, Q_A is the measured controlled release rate during, z_m is the height of the CH_4 concentration measurement, r_Q is the horizontal distance between the source and the sensor, and α_A is the actual azimuth between the source and the sensor (relative to true North).

	Interval Name	**Date**	**Time [MST]**	t_m **[s]**	Q_A **[g s^{-1} m^{-2}]**	z_m **[m]**	r_Q **[m]**	α_A **[°]**
XS1	623A	06/23/13	0915-1200	9900	5.452±0.091	8.66	43±1	215±1
	623B	06/23/13	1210-1325	4500	5.452±0.091	4.50	43±1	215±1
	624A	06/24/13	0940-1040	3600	0.659±0.048	4.50	46±1	209±1
	624B	06/24/13	1120-1230	4200	0.659±0.048	4.50	52±1	199±1
	625	06/25/13	1025-1135	4200	26.312±0.252	8.66	86±1	257±1
	626	06/26/13	0830-1200	12600	0.080±0.080	4.50	93±1	249±1
XS2	624A	06/24/13	0940-1040	3600	0.659±0.048	4.60	60±1	213±1
	624B	06/24/13	1120-1230	4200	0.659±0.048	4.60	64±1	205±1
	625	06/25/13	1025-1135	4200	26.312±0.252	8.49	95±1	264±1
	626	06/26/13	0830-1200	12600	0.080±0.080	4.60	107±1	246±1

4.2.7 Source azimuth detection method

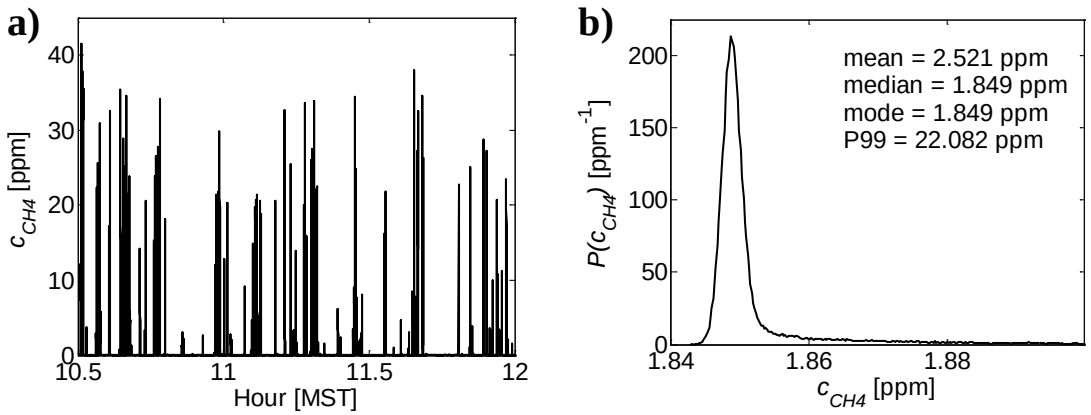

Figure 4.6: a) A timeseries of the total concentration (c_T) measured at 8.66 m AGL, 42.7 m downwind of a 5.452±0.091 g s^{-1} m^{-2} controlled release on June 23rd, 2013. **b)** The probability distribution of concentration measurements in the timeseries. P99 is the 99th percentile value of the distribution.

The source azimuth relative to the concentration sensor (α) was determined by measuring the instantaneous concentration as a function of wind direction. Yee et al (1995) and Nottrott et al (2014) have shown that the signature of a localized source dispersing in the atmospheric surface layer is an intermittent, spiky concentration signal. Figure 4.6a is a timeseries of concentration measurements downwind of a 5.452±0.091 g s^{-1} m^{-2} controlled release on June 23rd, 2013. The data in Figure 4.6a are characterized by a high level of intermittency. Most of the measurements are near the background concentration (about 1.85 ppm), however, there are a large number of concentration spikes in the range of 3-40 ppm. Figure 4.6b shows the probability distribution of the concentration fluctuations along values for the mean, median, mode and 99th percentile (P99) of the distribution. The median and mode are indicators of background concentration, while the mean is not a good representation of the background or intermittent large concentration spikes. The P99 value is representative of concentration

spikes due to the strong skewness of data. Thus the P99 value is a reliable metric for detecting localized sources upwind of a concentration sensor.

The source azimuth relative to the concentration sensor was determined by grouping concentration measurements by wind direction (μ), and calculating the P99 concentration for each bin. The result is the distribution of P99 CH_4 concentration as a function of wind direction (Figure 4.7). The centroid of the distribution indicates the measured source azimuth relative to the sensor (α_m). The α_m is given by,

$$\alpha_m = \frac{\int_{0°}^{360°} \mu P99_{CH4}\, d\mu}{\int_{0°}^{360°} P99_{CH4}\, d\mu} \qquad 4.3$$

Empirical testing showed that the centroid of the distribution is a better indicator of the source azimuth than the maximum of the distribution, because it is less sensitive to individual large concentration events that occur when the wind exactly is not directly aligned with the true source azimuth (α_A).

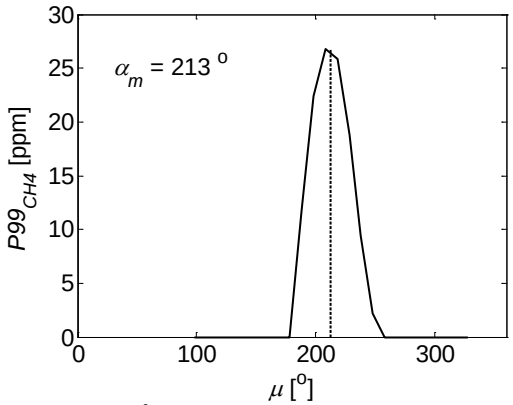

Figure 4.7: Distribution of the 99th percentile CH_4 concentration ($P99_{CH4}$) as a function of wind direction (solid black line) for the data shown in Figure 4.6. The centroid of the distribution indicates the measured source azimuth relative to the concentration sensor (α_m). The width of the wind direction bins is 10°.

4.3 Results

4.3.1 Meteorology and turbulence conditions

Meteorological conditions for each measurement period are listed in Table 4.3. The clear sky index (*kt*) is defined as the ratio of measured global horizontal irradiance (*GHI*) to the clear sky global horizontal irradiance (GHI_{csk}). The clear sky global horizontal irradiance was modeled using the American Society of Civil Engineers standard (Allen et al, 2005). The value of *kt* varies between 1 in clear skies and about 0.1 in overcast conditions, and is an indicator of cloudiness and atmospheric turbidity. Clear sky conditions occurred during measurement periods 623A, 623B and 624A. Large cumulus clouds during periods 624B, 625 and 626 may have contributed to the formation of secondary updrafts and downdrafts due near the surface due to localized patches of surface cooling from cloud shadows.

Table 4.3: Meteorological variables during each measurement period. *GHI* is the global horizontal irradiance, *kt* is the clear sky index (refer to Section 4.3.1), T_{air} is the air temperature, T_{sfc} is the ground surface temperature, $\bar{u}$ is the mean streamwise wind velocity and μ is the wind direction (relative to true North). Average and standard deviations taken over the entire measurement interval are listed for each variable.

Interval Name	*GHI* [W m^{-2}]	*kt* [-]	T_{air} [°C]	T_{sfc} [°C]	$\bar{u}$ [m s^{-1}]	μ [°]
623A	879±64	0.97±0.01	20.5±1.3	33.5±3.2	4.7±1.5	215±22
623B	948±11	0.99±0.00	23.7±0.6	39.1±1.1	3.5±2.4	211±23
624A	891±41	1.00±0.04	28.7±0.4	43.3±1.1	0.25±3.8	182±22
624B	788±248	0.81±0.26	30.4±0.5	43.5±3.6	3.2±2.1	213±28
625	589±339	0.62±0.36	24.7±0.5	36.5±4.9	5.7±2.1	263±25
626	777±210	0.89±0.20	27.7±1.8	41.3±4.7	4.6±1.7	251±23

Sensible and latent heat fluxes, crosswind horizontal turbulence intensity, surface shear stress and Obukhov length are listed in Table 4.4 for the six measurement periods. The sensible heat flux was relatively constant throughout all measurement periods, while significant variability was observed in the latent heat flux. Among periods 623A, 623B,

624A and 624B the latent heat flux is generally greater in the morning than the afternoon. The exceptionally large latent heat flux on 625 was due to rain in the early morning of June 25th, 2013. The surface level stability conditions were primarily characterized by forced convection. Strong convection during the 624A interval was caused by near zero wind speeds (see Table 4.3).

Table 4.4: Turbulence parameters during each measurement period. $\overline{w'\theta_v'}$ is the sensible heat flux, $\overline{w'q'}$ is the latent heat flux, $\overline{v'^2}^{1/2}$ is the root mean square of the turbulent component of crosswind horizontal velocity, u_* is the friction velocity (surface shear stress) and L is the Obukhov length. Averages are taken over the entire measurement interval.

Interval Name	$\overline{w'\theta_v'}$ **[K m s^{-1}]**	$\overline{w'q'}$ **[g$_{H2O}$ g$_{air}^{-1}$ m s^{-1} 10^{-4}]**	$\overline{v'^2}^{1/2}$ **[m s^{-1}]**	u_* **[m s^{-1}]**	L **[m]**
623A	0.23	0.61	1.8	0.41	-22
623B	0.29	0.59	2.1	0.43	-21
624A	0.23	0.41	1.4	0.27	-7.8
624B	0.22	0.30	1.9	0.36	-17
625	0.21	0.94	2.0	0.39	-22
626	0.24	0.20	1.8	0.39	-20

4.3.2 Accuracy of source azimuth detection

The accuracy of the source azimuth detection method described in Section 4.2.7 was evaluated using data from both towers during the six measurement periods (see Table 4.2). Figure 4.8 shows the measured azimuth angle (α_m) plotted as a function of the actual azimuth angle (α_a) in a correlation plot. The vertical error bars represent the 99% confidence interval of α_m. The 99% confidence interval of α_m is based on the width of the wind direction bins used Figure 4.7, assuming there is a uniform probability that α_m lies anywhere within the bin. Using a bin width of 10° the standard deviation (63% confidence interval) associated with the uncertainty in α_m is σ_m = 3.3°, and the 99% confidence interval is 2.576σ_m = 7.7° based on the standard *t*-table. The data in Figure 4.8

show that the azimuth detection method described in Section 4.2.7 accurately predicts the source direction relative to the concentration sensor.

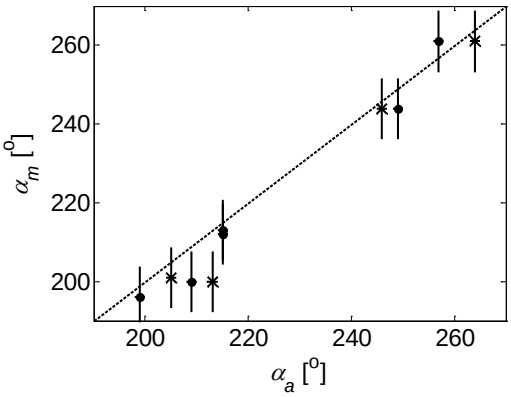

Figure 4.8: A correlation plot of the measured source azimuth angle (α_m) as a function of the actual azimuth angle (α_a). The dashed line is the 1:1 line corresponding to a perfect correlation between α_m and α_a. The vertical error bars represent the 99% confidence interval of α_m. XS1 data indicated by points; XS2 data indicated by crosses.

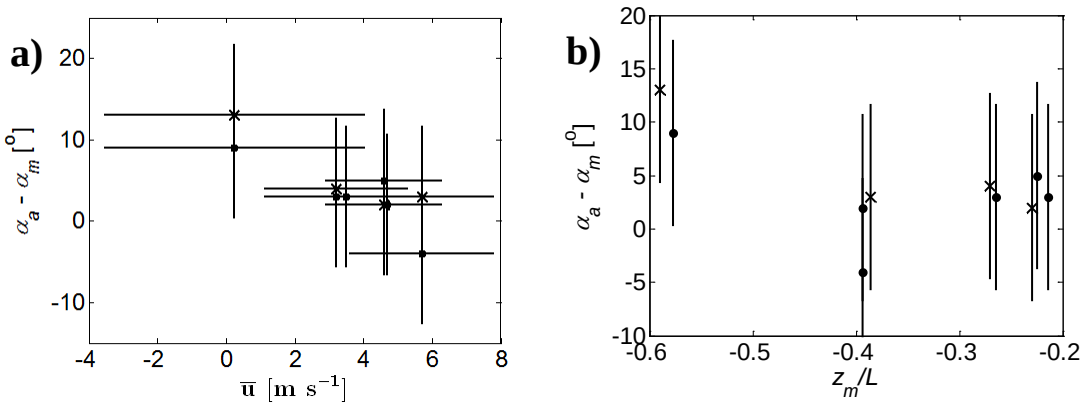

Figure 4.9: The difference between the actual measured source azimuth angle ($\alpha_a - \alpha_m$) as a function of **a)** mean streamwise wind velocity ($\bar{u}$) and **b)** atmospheric stability (refer to Section 1.3.2). The horizontal error bars in Figure 4.9a represent the standard deviation of the mean streamwise wind velocity during each measurement interval. The vertical error bars represent the 99% confidence interval of α_m. XS1 data indicated by points; XS2 data indicated by crosses.

Figure 4.9 shows the difference between the actual and measured source azimuth angle as a function of mean wind speed and atmospheric stability. Generally, the absolute error in the measured azimuth angle is <5° except during calm winds. Large errors in the measured azimuth angle are expected during calm winds because there is a low correlation between the wind direction and measured concentraiton.

4.3.3 Accuracy of the concentration footprint model

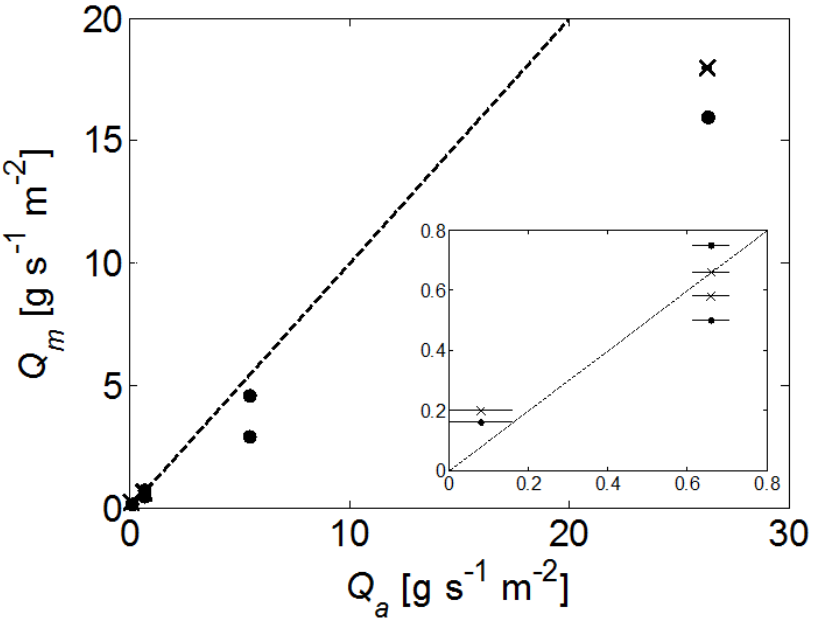

Figure 4.10: A correlation plot of the modeled CH_4 flux (Q_m) as a function of the measured CH_4 flux (Q_a). The dashed line is the 1:1 line corresponding to a perfect correlation between Q_m and Q_a. The inset shows a magnified view of data for release rates <1 g s^{-1} m^{-2}. Horizontal error bars represent the measured variability in CH_4 controlled release rate. The axes of the inset are the same as the main graph. XS1 data indicated by points; XS2 data indicated by crosses.

The accuracy of the quasi-analytical concentration footprint model (refer to Section 3.2.2 and Appendix A.2) for source strength prediction was assessed using data from the six measurement periods. Figure 4.10 is a correlation plot of the modeled CH_4 flux (Q_m) calculated using the concentration footprint model as a function of the

measured CH_4 flux (Q_a). The horizontal error bars in Figure 4.10 represent the measured variability in CH_4 controlled release rate. Strong correlation was observed between the measured and modeled flux rates for fluxes <1 g s^{-1} m^{-2}. There was a large uncertainty associated with data for the lowest flow rate because a standard, analog welding regulator valve was used instead of the digital flow meter in order to achieve a flow rate <0.65 g s^{-1}. At higher flux rates the model significantly underestimated the source flux.

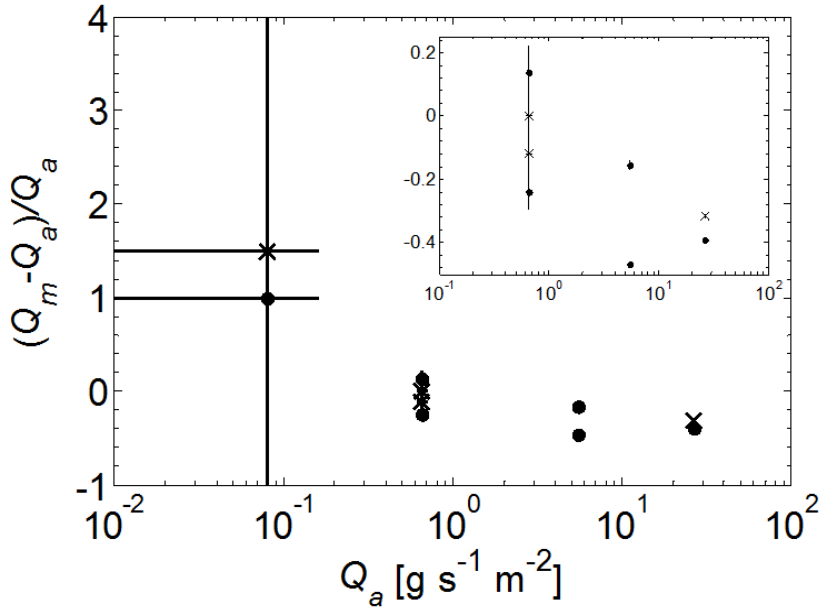

Figure 4.11: The relative error of the modeled CH_4 flux $(Q_m - Q_a)/Q_a$ as a function of the measured flux plotted on a semi-log scale. The inset shows a magnified view of the data for the largest flux rates. Horizontal error bars represent the measured variability in CH_4 controlled release rate. Vertical error bars represent the contribution of the measured uncertainty in CH_4 controlled release rate to the relative error. The axes of the inset are the same as the main graph. XS1 data indicated by points; XS2 data indicated by crosses.

Figure 4.11 shows the relative error of the modeled CH_4 flux $(Q_m - Q_a)/Q_a$ as a function of the measured CH_4 flux. Horizontal error bars represent the measured variability in CH_4 controlled release rate. Vertical error bars represent the contribution of the measured uncertainty in CH_4 controlled release rate to the relative error. Error

propagation was calculated using the partial derivative method (Taylor, 1997). The data in Figure 4.11 show that absolute relative error of the modeled flux is generally <50% with the exception of the lowest flux. However, there is a large uncertainty in the relative error associated with the lowest flux due to the type of regulator valve used to control the CH_4 flow rate.

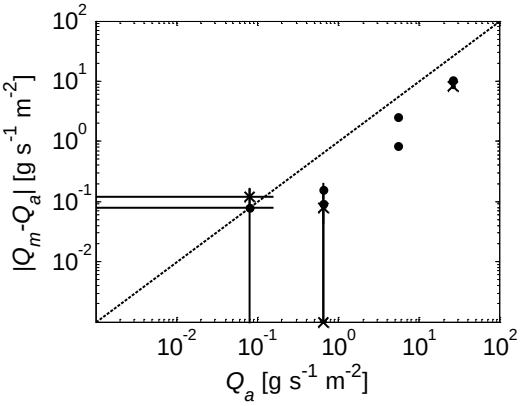

Figure 4.12: The absolute error between the modeled and measured CH_4 flux $|Q_m - Q_a|$ plotted as a function of the measured CH_4 flux on a log-log scale. The dashed line is the 1:1 line. The error bars have the same meaning as in Figure 4.11. XS1 data indicated by points; XS2 data indicated by crosses.

The absolute error between the modeled and measured CH_4 flux $|Q_m - Q_a|$ is plotted as a function of the measured CH_4 flux in Figure 4.12. The absolute error for all modeled fluxes, except the lowest flux, falls below the 1:1 line. That result is important because it demonstrates that the concentration footprint model provides an upper bound for the trace gas flux from fugitive emissions sources.

4.4 Discussion and conclusions

Atmospheric measurements of turbulence and CH_4 concentration made during an outdoor, controlled release experiment were used to demonstrate the feasibility of the

source determination method developed in Chapter 3. The two main components of the source determination model were evaluated. A novel, data based method for detecting the azimuth between a fugitive emissions source (for which the location is not known a priori) and a concentration sensor was described in Section 4.2.7. The azimuth detection method provided accurate predictions of the source azimuth when applied to data from the experiment. The uncertainty of the source azimuth predictions from the experiment (<5°) was consistent with the uncertainty reported by Henry et al. (2002) for more distant sources (±3-7°). It is worth noting that Henry et al. (2002) used one year of concentration and wind data, while the results in Section 4.3.2 were obtained from only a few hours of data. Figure 4.7 demonstrates that an azimuth detection method based on metrics of concentration fluctuations is more sensitive to low flux sources than a method based on mean concentration. Unfortunately, due to the arrangement of the towers, the predicted azimuth data from the field experiment could not be used to determine the source location directly. However, the analysis in Sections 3.3.1 and 3.3.3 showed that the source location could be accurately determined based on the level of observed uncertainty in the azimuth detection method (Figure 4.8).

The accuracy of a concentration footprint model for fugitive emissions flux prediction (Appendix A.2) was assessed in Section 4.3.3. The model underestimated source strength by up to 50%, and the magnitude of the error appeared to increase with source strength (Figures 4.10 and 4.11). An important assumption in Eq. A.2.1 is that the source gas is emitted at the same velocity as the surrounding fluid. A possible explanation for the increase in model error with source strength is that the assumption of an isokinetic source was violated at the largest flow rates. Indeed, visualization of the 26 g s^{-1} m^{-2} flux by

infrared thermography revealed strong jets emanating from the perforations in the diffuser. However, a flux of 26 g s^{-1} m^{-2} is at least one order of magnitude greater than would be expected in fugitive leak detection applications, and would likely be detectable from audible, visual, tactile and/or olfactory queues. For smaller leaks, the source determination model in Chapter 3 can be combined with the measurement techniques described in this chapter for detection and long-term, continuous monitoring applications.

Acknowledgement

The content of Chapter 4 is being prepared for publication in Nottrott A., Rahn T., Dubey M., Keeling R., Kleissl J., 2014, Top-down emissions quantification using atmospheric measurements from a methane controlled release experiment. Manvendra Dubey of Los Alamos National Laboratory (LANL), Earth and Environmental Systems Division was the principal investigator for the field experiment, and Anders Nottrott is the first author of the publication.

5. Conclusion

The credibility of regulatory frameworks for control and reduction of greenhouse gas (GHG) emissions depends on having a reliable method for independent verification and long-term monitoring of the actual emissions of market participants. While long-term verification and monitoring is relatively straightforward for centralized GHG emissions sources, like power plants and refineries, it is complicated for distributed sources, where GHG sources from natural gas infrastructure, petroleum extraction and/or carbon sequestration operations are sparsely distributed over areas on the order of 1-1000 km^2. This work generated new insights into the performance of state of the art trace gas dispersion models, and developed novel measurement and modeling techniques for locating and quantifying fugitive emissions from distributed sources.

5.1 Conclusions

5.1.1 Large-eddy simulation

Large-eddy simulation provides a framework to obtain turbulence data for wind and scalar fields in the atmospheric boundary layer at greater spatiotemporal resolution than mesoscale atmospheric models or direct measurements. At the present time, the computational cost of large-eddy simulation (LES) remains prohibitive for real-time modeling and operational forecasting. However, two-way nesting of mesoscale and local (LES) scale boundary for operational modeling will be feasible in the near future. This capability will enable realistic simulations of dispersion from distributed, local scale GHG emissions sources. The Weather Research and Forecasting model (WRF) has multi-scale, nested simulation capability (from synoptic to local scales), includes real-world

land-use and topographic data, and has the capability to ingest regional-scale meteorological forcing data (i.e. data assimilation).

The WRF model currently provides the best platform for the development of a unified synoptic to local scale atmospheric modeling system. WRF large-eddy simulation code (WRF-LES) accurately modeled mean plume trajectories and concentration fields. WRF-LES statistics of concentration fluctuations in the daytime convective boundary layer were similar to data obtained from laboratory experiments and other LES models. However, poor turbulence resolution near the surface in neutral boundary layer simulations caused under prediction of mean dispersion in the crosswind horizontal direction and over prediction of concentration variance in the neutral surface layer.

5.1.2 In situ atmospheric measurements for GHG monitoring

The development of top-down methodologies for quantifying fugitive greenhouse gas emissions has been hindered by sparse spatiotemporal coverage of direct atmospheric GHG measurements. The lack of direct measurements has been primarily due to inadequacy of existing equipment for field deployment, and the high cost of measurements. The recent development of robust, accurate and affordable spectrometers for GHG measurements has made accurate, long-term, continuous field measurements of GHGs feasible. In-situ, point measurements of GHG concentration are advantageous for top-down emissions measurements because they are capable of continuous sampling rates up to 10 Hz, highly accurate and sensitive to ppb scale changes in concentration for many GHG species. Fast response turbulence measurements can be collocated with

concentration measurements to quantify the influence of upstream sources on point measurements in the context of atmospheric dispersion.

Recently, there has been significant interest in the application of airborne remote sensors to map column integrated GHG concentration over large spatial areas (Thorpe et al, 2013). However, there are several major limitations of airborne remote sensing methods in the context of long-term, continuous monitoring. Although the spatial coverage of remote sensing measurements O(1-1000 km^2) is larger than the sampling footprint of an in situ tower measurement O(1 km^2), remote sensors (like the Airborne Visible/Infrared Imaging Spectrometer; AVIRIS) can only capture instantaneous snapshots of column integrated GHG concentration. Thus the temporal frequency of remotely sensed measurements is limited to a few samples on a monthly interval by the high cost of flying time, the minimum concentration detection threshold for surface sources is high due to the long optical path length between the aircraft and the ground, and emission rate calculations are complicated by unknown surface winds and turbulence variables which drive GHG dispersion. Passive remote sensors also suffer from reduced sensitivity during cloudy and dusty conditions, and are inoperable at night.

By contrast, surface-level, in situ, concentration measurements are autonomous, and cheaper and easier to maintain than airborne remote sensors. A source determination model was developed to predict the location and strength of continuous, surface level, trace gas sources using concentration and turbulence measurements at only two locations. The requirement for measurements at only two location is advantageous because a large sensor array is impractical for GHG monitoring applications due to high equipment costs and practical constraints on feasible sites for sensor placement (such as topography and

land/infrastructure ownership). The model can be applied to determine the optimal placement of sensors required to monitor sources, or to determine the monitoring capability of an existing sensor arrangement over local scale geographic area.

Atmospheric measurements of turbulence and CH_4 concentration made during an outdoor, controlled release experiment were used to demonstrate the feasibility of the source determination method in a realistic setting. A method for determining relative source-senor location by triangulation was applied to accurately predict the location of an a priori unknown fugitive emissions source. A concentration footprint model was used to constrain the trace gas flux from the source. Comparison with atmospheric measurements showed that the footprint model predicted the trace gas flux with less than 50% uncertainty and provided an upper bound for the trace gas flux from fugitive emissions sources. That observation has important implications for verifying GHG emissions in the context of regulatory limits. The source determination model can be used for detection and long-term, continuous monitoring of fugitive emissions.

5.2 Applications and future work

As development of a unified synoptic to local scale atmospheric modeling system continues, future WRF-LES research should focus on improving parameterizations for the eddy diffusivity coefficients in the wall-layer. A zonal approach like the Two-Layer Model (TLM; Piomelli & Balaras, 2002) may be appropriate. WRF-LES could be specialized for source determination applications in complex, inhomogeneous terrain by incorporating a backward Lagrangian stochastic dispersion model such as the Stochastic Time-Inverted Lagrangian Transport (STILT) model (Nehrkorn et al, 2010).

The source determination model of Chapter 3 and the measurement techniques described in Chapter 4 can be combined in a number of interesting applications. A network of stationary monitoring systems could be deployed to monitor and pinpoint fugitive emissions from enhanced oil recovery and carbon sequestration operations, where CO2 and other gasses are pumped into subterranean, depleted oil reservoirs. A mobile (i.e. vehicle based) monitoring system would improve the spatial coverage of the source determination model, and improve leak detection capabilities and industrial safety of oil and utility companies. Leveraging geographic information system (GIS) data about the location of gas infrastructure and measurements of isotopic trace gas ratios would improve the attribution capabilities of the source determination method.

Appendix

A.1 Supplemental information for WRF-LES simulations

A.1.1 Mathematical definitions for the scalar concentration field distribution

Mathematical definitions of the variables that define the trajectory of a scalar concentration field downwind of the source (refer to Section 2.2.1 and Figure 2.1). Eqs. A.1.1-A.1.6 are reproduced from Nieuwstadt (1992).

$$z_l = \frac{\iint_{A(x)} cz\, dy\, dz}{\iint_{A(x)} c\, dy\, dz}, \quad \text{A.1.1}$$

$$\bar{z} = \frac{\int_V cz\, dx\, dy\, dz}{\int_V c\, dx\, dy\, dz}, \quad \text{A.1.2}$$

$$s_z{}^2 = \frac{\int_V c(z - z_l)^2\, dx\, dy\, dz}{\int_V c\, dx\, dy\, dz}, \quad \text{A.1.3}$$

$$m_z{}^2 = \frac{\int_V c(z_l - \bar{z})^2\, dx\, dy\, dz}{\int_V c\, dx\, dy\, dz}, \quad \text{A.1.4}$$

$$\sigma_z^2 = s_z{}^2 + m_z{}^2 \quad \text{A.1.5}$$

$$\sigma_z{}'^2 = \frac{\int_V c(z - z_s)^2\, dx\, dy\, dz}{\int_V c\, dx\, dy\, dz} \quad \text{A.1.6}$$

z_l is the local (or instantaneous) plume centerline height, $\bar{z}$ is the average plume centerline height, s_z is the spreading component about the local centerline height and m_z is the meandering component about the average centerline height, σ_z is the total vertical dispersion, $\sigma_z{}'$ is the total vertical dispersion relative to the source height. *A(x)* in Eq. A.1.1 refers to the cross-sectional area of the numerical domain in the *y*-*z* plane, *V* in Eqs. A.1.2-A.1.6 is the total volume of the numerical domain and z_s is the source height. The same variables may also be used to define the crosswind horizontal trajectory of the plume. Note that $\sigma_y^2 = \sigma_y{}'^2$, because $y_s = 0$ by definition.

A.1.2 Impact of SGS model and grid resolution on horizontal crosswind dispersion

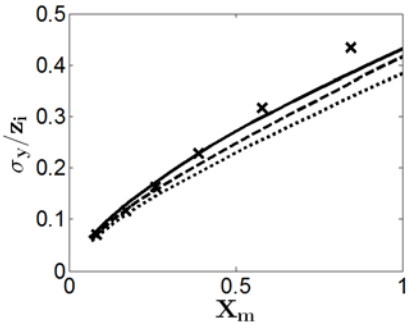

Figure A.1.1: Impact of SGS model and grid resolution on the total horizontal crosswind dispersion in the neutral ABL for a surface layer source at $z_s = 0.07z_i$. Case N without SGS dispersion (dotted line), case N with SGS dispersion (dashed line) and case NHR with SGS dispersion (solid line). WRF-LES data are compared to LES data from Dosio et al (2003) plotted with crosses.

A.2 Supplemental information for the source determination model

A.2.1 A quasi-analytical concentration footprint model

The crosswind integrated flux footprint (*f*) is given by

$$f(x, z_m) = \frac{1}{\kappa^2 x^2} D z_u^P |L|^{1-P} \exp\left(\frac{-1}{\kappa^2 x^2} D z_u^P |L|^{1-P}\right), \quad \text{A.2.1}$$

where x is the upwind distance from the sensor, z is the vertical direction, z_m is the sensor height AGL, L is the Obukhov length, κ is the von Kármán constant, and D and P are empirical coefficients that are piecewise functions of L. $z_u = z_m(ln(z_m/z_0) + z_0/z_m - 1)$ and z_0 is the aerodynamic roughness length. The crosswind integrated concentration footprint (*c*) can be related to *f* by the stationary, two-dimensional advection-diffusion equation (Kormann & Meixner, 2001).

$$u\frac{\partial c}{\partial x} = -\frac{\partial f}{\partial z} \quad \text{A.2.2}$$

First-order closure is used in Eq. A.2.2, crosswind dispersion is assumed to be constant in the *z* direction and horizontal turbulent diffusion along streamlines is assumed to be negligible compared to advection. The assumption of negligible along wind diffusion is commonly used because it simplifies the calculation of the concentration footprint function. Kljun et al (2002) assessed the validity of this assumption using a three-dimensional, stochastic flux footprint model. Kljun et al found that, for a sensor located at 20 m AGL, the effect of neglecting the along wind diffusion component was small in convective conditions. Neglecting the along wind diffusion component in the neutrally stratified ABL caused the location of max(*f*) and max(*c*) to shift upwind relative to the sensor by about 25%, and resulted in a 20-30% reduction in the magnitude of max(*f*) and max(*c*). A 63% upwind shift relative to the sensor of the location of max(*f*) was observed

for a sensor located at 100 m AGL in the neutrally stratified ABL, but the change in the magnitude of max(*f*) was negligible.

The crosswind integrated concentration footprint was obtained by differentiating Eq. A.2.1 with respect to *z* and integrating Eq. A.2.2. *u* in Eq. A.2.2 was taken to be the mean streamwise velocity at the measurement height $\bar{u}(z_m)$. The crosswind distributed flux and concentration footprints (η_f and η_c) are related to the crosswind integrated footprint by

$$\eta_f(x, y, z_m) = D_y(x, y) f(x, z_m), \quad \text{A.2.3a}$$

$$\eta_c(x, y, z_m) = D_y(x, y) c(x, z_m), \quad \text{A.2.3b}$$

where *y* is the crosswind horizontal direction and $D_y(x, y)$ is a Gaussian crosswind distribution function (Schmid, 1994) given by

$$D_y(x, y) = \frac{1}{\sqrt{2\pi}\sigma} \exp\left(\frac{-y^2}{2\sigma^2}\right), \quad \text{A.2.4a}$$

$$\sigma = \hat{v}x/\bar{u}(z_m). \quad \text{A.2.4b}$$

$\hat{v}$ in Eq. A.2.4b is the crosswind horizontal r.m.s. turbulent velocity. In practice $\bar{u}(z_m)$ and $\hat{v}(L)$ would be obtained from measurements, but in this paper we parameterized $\bar{u}(z_m)$ and $\hat{v}(L)$ with empirical correlations. $\bar{u}(z_m)$ was calculated from the Monin-Obukhov similarity theory using flux-profile relationships from Högström (1988).

$$\frac{\partial \bar{u}}{\partial z} = \frac{u_*}{\kappa z} \phi_M(z/L) \quad \text{A.2.5a}$$

$$\phi_M(z/L) = \begin{cases} [1 - 19.3(z/L)]^{-1/4} & L < 0 \\ 1 + 4.8(z/L) & L \geq 0 \end{cases} \quad \text{A.2.5b}$$

$\hat{v}(L)$ was parameterized by empirical correlations from Panofsky et al (1977) and Wyngaard (1975).

$$\hat{v}(L) = \begin{cases} u_*(12 + z_i/|L|)^{1/3} & L < 0 \\ 1.75u_* & L \geq 0 \end{cases} \quad \text{A.2.6}$$

A.2.2 Validation of the footprint function by inter-model comparison

The crosswind integrated footprint function (*f*) computed using Eq. A.2.1 for convective, neutral and stable ABL conditions produced identical results to Hsieh et al (2000). We compared *f* (Eq. A.2.1) and η_f (Eq. A.2.3a) to the model of Kormann & Meixner (2001) for convective, neutral and stable conditions (Figure A.2.1). Differences between modeled values of magnitude of *f* and the location of max(*f*) were <20% in convective and neutral conditions (Figure A.2.1a). The magnitude of *f* modeled with Eq. A.2.1 was 2.5 times larger than the model of Kormman and & Meixner in weakly stable stratification, although the location of max(*f*) was nearly identical between the two models. Major differences were observed between the models for the normalized crosswind distributed flux footprint function $\eta_f/\max(\eta_f)$ (Figure A.2.1b). The data in Figure A.2.1b show that the width of the η_f decreases as *L* increases, however, Kormann & Meixner observed the opposite behavior. Schmid (1994) showed that the width of η_f increases with increasing $\hat{v}$, and the different trend in observed for the width of η_f as a function of *L* was attributed to the different parameterization of $\hat{v}(L)$ (Eq. A.2.6) used in the two models. Plotting Figure A.2.1b using the same parameterization for $\hat{v}(L)$ as

Kormann & Meixner (2001) caused to the width of the η_f increase with L (not shown). This finding is significant because it emphasizes the importance of using the correct value of $\hat{v}$ when computing η_f and η_c. It is worth noting that Kljun et al (2002) also found that the width of η_f increased with L, but they did not list their parameterization for $\hat{v}(L)$. In practice $\hat{v}(L)$ depends on site specific characteristics (e.g. terrain and vegetation), and should be measured directly rather than parameterized.

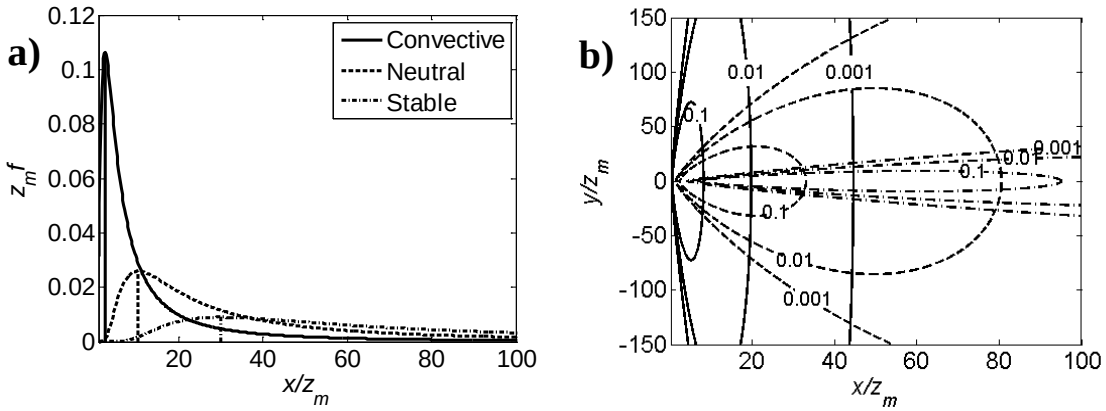

Figure A.2.1: a) Crosswind integrated flux footprint (*f*) from Eq. A.2.1 and **b)** contours of the normalized crosswind distributed flux footprint $\eta_f / \max(\eta_f)$ from Eq. A.2.3a. z_m = 10 m and z_0 = 0.1 m. u_* = 0.2 m s^{-1}, L = -10 m for the convective case (solid line); u_* = 0.8 m s^{-1}, L = -∞ m for the neutral case (dashed line); u_* = 0.5 m s^{-1}, L = 10 m for the stable case (dash-dotted line). Refer to Figure 4 in Kormann & Meixner (2001) for comparison.

Kljun et al (2002) developed a three-dimensional Lagrangian stochastic inverse dispersion model (LPDM-B) to calculate trace gas and concentration footprints. Figure A.2.2 shows crosswind integrated flux and concentration footprints calculated from Eqs. A.2.1 and A.2.2 for z_m = 20 m and z_0 = 0.05 m in convective and neutral ABL stability conditions using the same parameters as in Kljun et al (2002). Generally *f* and *c* computed from Eqs. A.2.1 and A.2.2 are similar to results from LPDM-B. The location of max(*f*) shifted upwind relative to the sensor by about 120-190% in the LPDM-B model compared to Eq. A.2.1, and the location of max(*c*) shifted downwind relative to the sensor by 25-40% in LPDM-B compared to Eq. A.2.2. The magnitude of max(*f*) was 75% smaller in LPDM-B than Eq. A.2.1. max(*c*) was 80% larger in LPDM-B than Eq. A.2.2 for convective conditions and max(*c*) was 40% smaller in LPDM-B than Eq. A.2.2 for neutral stratification. Kljun et al (2004) noted that the location of the max(*f*) modeled with Eq. A.2.1 was similar to other flux footprint models for z_m <20 m in all stability conditions. However, when z_m >20m in strongly convective and strongly stable ABL conditions the location of max(*f*) modeled with Eq. A.2.1 differed considerably from other models. The proposed concentration footprint model is reasonable based on the data in Figures A.2.1 and A.2.2, and the analysis in this paper is restricted to sensor heights z_m <20.

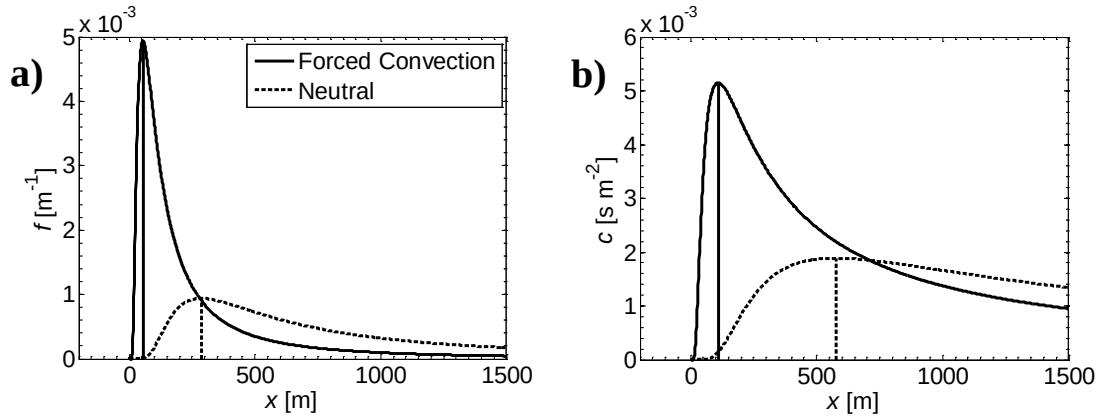

Figure A.2.2: Crosswind integrated **a)** flux footprint (*f*; Eq. A.2.1) and **b)** concentration footprint (*c*; Eq. A.2.2) for forced convective (solid line) and neutral (dashed line) conditions. z_m = 20 m and z_0 = 0.05 m. . u_* = 0.2 m s^{-1}, L = -36 m for the forced convective case; u_* = 0.8 m s^{-1}, L = -∞ m for the neutral case. Refer to Figures 6 and 7 in Kljun et al (2002) for comparison.

A.3 Supplemental information for the methane controlled release experiment

A.3.1 Impact of sharpening filter on the frequency content of measured concentration fluctuations

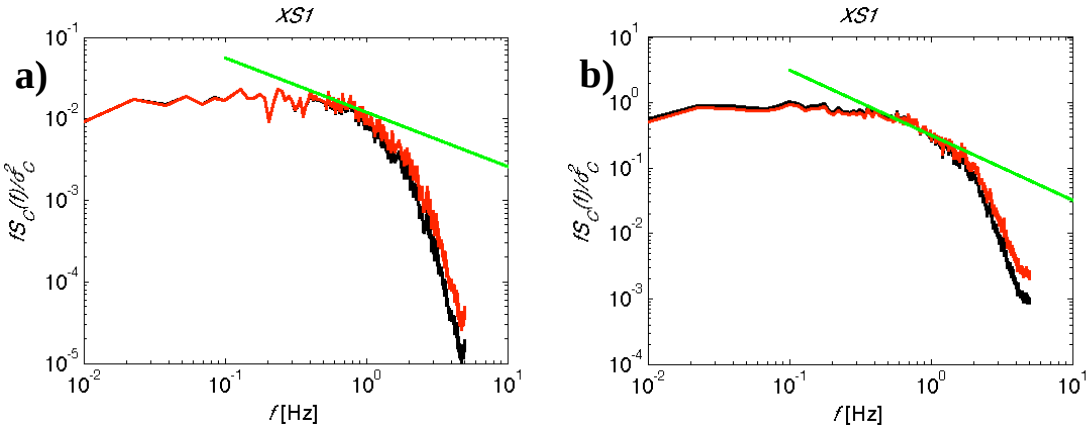

Figure A.3.1: Normalized energy spectra of the concentration time series measured at the XS1 tower on **a)** June 24th, 2013 and **b)** June 26th, 2013 before sharpening (back line) and after sharpening (red line). The green line shows the -5/3 Kolmogorov slope. Note that the difference between the unsharpened and sharpened energy spectra becomes large at frequencies >2 Hz.

References

Allen R.G., Walter I.A., Elliott R., Howell T., Itenfisu D., Jensen M. (Eds.), 2005, The ASCE standardized reference evapotranspiration equation, Task Committee on Standardization of Reference Evapotranspiration, Environmental and Water Resources Institute, American Society of Civil Engineers.

Andren A., Brown A.R., Graf J., Mason P.J., Moeng C-H., Nieuwstadt F.T.M., Schumann U., 1994, Large-eddy simulation of a neutrally stratified boundary layer: A comparison of four computer codes, *Quarterly Journal of the Royal Meteorological Society* 120, pp. 1457-1484.

Arata C., Rahn T.A., Aubrey A.D., 2013, Fugitive Methane Source Detection and Discrimination with the Picarro Mobile Methane Investigator, *American Geophysical Union Fall Meeting, San Francisco, CA.*

Aubrey A.D., Thorpe A.K., Christensen L.E., Dinardo S., Frankenberg C., Rahn T.A., Dubey M.K., 2013, Demonstration of Technologies for Remote and in Situ Sensing of Atmospheric Methane Abundances – a Controlled Release Experiment, *American Geophysical Union Fall Meeting, San Francisco, CA.*

Batchelor G.K., 1952, Diffusion in a field of homogeneous turbulence, *Mathematical Proceedings of the Cambridge Philosophical Society* **48** (2), pp. 345-362.

Beare R.J., Macvean M.K., Holtslag A.A.M., Cuxart J., Esau I., Golaz J.-C., Jimenez M.A., Khairoutdinov M., Kosovic B., Lewellen D., Lund T.S., Lundquist J.K., McCabe A., Moene A.F., Noh Y., Raasch S., Sullivan P., 2006, An intercomparison of large-eddy simulations of the stable boundary layer, *Boundary-Layer Meteorology* **118**, pp. 247-272.

Borgas M.S., Sawford B.L., 1991, The small-scale structure of acceleration correlations and its role in the statistical theory of turbulent dispersion, *Journal of Fluid Mechanics* **228**, pp. 295-320.

Bou-Zeid E., Meneveau C., Parlange M., 2005, A scale-dependent Lagrangian dynamic model for large eddy simulation of complex turbulent flows, *Physics of Fluids* **17**, pp. 025105.

Bundesamt für Umwelt (BAFU), Schweizerische Eidgenossenschaft, 2013, Erhebung der CO_2-Abgabe auf Brennstoffen (Collecting CO_2 tax on fuels), Available online at <http://www.bafu.admin.ch/co2-abgabe/12357/index.html?lang=de>, Accessed December, 5th 2013.

Businger J.A., 1982, Equations and concepts, In Nieuwstadt F.T.M., van Dop H. (Eds.), *Atmospheric Turbulence and Air Pollution Modelling*, Dordrecht, The Netherlands: Kluwer Academic Publishers.

California Environmental Protection Agency, Air Resources Board (CARB), "Cap-and-Trade Program", Available online at <http://www.arb.ca.gov/cc/capandtrade/capandtrade.htm>, Accessed March 18th, 2013.

Chen B., Black T.A., Coops N.C., Hilker T., Trofymow J.A., Morgenstern K., 2009, Assessing tower flux footprint climatology and scaling between remotely sensed and eddy covariance measurements, *Boundary-Layer Meteorology* **130**, pp. 137-167.

Chen J.C., Yao K., Hudson R.E., 2002, Source localization and beamforming, *IEEE Signal Processing Magazine* **19** (2), pp. 30-39.

Christen A., Coops N.C., Crawford B.R., Kellett, KN Liss, I Olchovski, TR Tooke, M van der Laan, JA Voogt, Validation of modeled carbon-dioxide emission form an urban neighborhood with direct eddy-covariance measurements, *Atmospheric Environment* 45, 2011, pp. 6057-6069.

Crosson E.R., 2008, A cavity ring-down analyzer for measuring atmospheric levels of methane, carbon dioxide, and water vapor, *Applied Physics B: Lasers and Optics* **92** (3), pp 403-408.

Deardorff J.W., 1970, A numerical study of three-dimensional turbulent channel flow at large Reynolds numbers, *Journal of Fluid Mechanics* **40** (2), pp. 453-480.

Deardorff J.W., 1978, Closure of second and third moment rate equations for diffusion in homogeneous turbulence, *Physics of Fluids* **21**, pp. 355-376.

Deardorff J.W., Willis G.E., 1984, Groundlevel concentration fluctuations from a buoyant and a non-buoyant source within a laboratory convectively mixed layer, *Atmospheric Environment* **18** (7), 1297-1309.

Dosio A., Arellano J.V-G., Holtslag A.A.M., Builtjes P.J.H., 2003, Dispersion of a passive tracer in buoyancy- and shear-driven boundary layers, *Journal of Applied Meteorology* **42**, pp. 1116-1130.

Draxler R.R., 1976, Determination of atmospheric diffusion parameters, *Atmospheric Environment* **10**, pp. 99-105.

Driedonks A.G.M., Tennekes H., 1984, Entrainment effects in the well-mixed atmospheric boundary layer, *Boundary-Layer Meteorology* **30**, pp. 75-105.

Dubey M.K., Lindernaier R., Arata C., Costigan K.R., Frankenberg C., Kort E.A., Rahn T.A., Henderson B.G., Love S.P., Aubrey A.D., 2013, Field Observations of Methane Emissions from Unconventional and Conventional Fossil Fuel Exploration, *American Geophysical Union Fall Meeting, San Francisco, CA.*

Ekins P., Barker T., 2002, Carbon taxes and carbon emissions trading, *Journal of Economic Surveys* **15** (3), pp. 326-376.

Emission Database for Global Atmospheric Research (EDGAR), Release version 4.0, 2009, European Commission, Joint Research Centre (JRC)/Netherlands Environmental Assessment Agency (PBL), Available online at <http://edgar.jrc.ec.europa.eu>, Accessed December 20th, 2012.

Etling D., 1990, On plume meandering under stable stratification, *Atmospheric Environment* **24A** (8), pp. 1979-1985.

Fackrell J.E., Robins A.G., 1982, Concentration fluctuations and fluxes in plumes from point sources in a turbulent boundary layer, *Journal of Fluid Mechanics* **117**, pp. 1-26.

Finnigan J., 2004, The footprint concept in complex terrain, *Agricultural and Forest Meteorology* **127**, pp. 117-129.

Fischer H.B., List E.J., Koh R.C.Y., Imberger J., Brooks N.H., 1979, Mixing in Inland Coastal Waters, Academic Press, New York, 497 pgs.

Flesch T.K., Wilson J.D., Yee E., 1995, Backward-time Lagrangian stochastic dispersion models and their application to estimate gaseous emissions, *Journal of Applied Meteorology* **34**, pp. 1320-1332.

Gesch, D.B., 2007, The National Elevation Dataset, in Maune, D. Ed., Digital Elevation Model Technologies and Applications: The DEM Users Manual, 2nd Edition: Bethesda, Maryland, American Society for Photogrammetry and Remote Sensing, pp. 99-118.

Gesch, D., Oimoen, M., Greenlee, S., Nelson, C., Steuck, M., and Tyler, D., 2002, The National Elevation Dataset: Photogrammetric Engineering and Remote Sensing, **68** (2), pp. 5-11.

Grant A.L.M., 1986, Observations of boundary layer structure made during the 1981 KONTUR experiment, *Quarterly Journal of the Royal Meteorological Society* **112**, pp. 825-841.

Grant A.L.M., 1992, The structure of turbulence in the near-neutral atmospheric boundary layer, *Journal of Atmospheric Sciences* **49**, pp. 226-239.

Hanna S.R., Briggs G.A., Hosker R.P., 1982, Handbook on Atmospheric Diffusion, Technical Information Center, U.S. Department of Energy, DOE/TIC-11223.

Hanna S.R., Insley E.M., 1989, Time series analyses of concentration and wind fluctuations, *Boundary-Layer Meteorology* **47**, pp. 131-147.

Henn D.S., Sykes R.I., 1992, Large-eddy simulation of dispersion in the convective boundary layer, *Atmospheric Environment* **26A** (17), pp. 3145-3159.

Henry R.C., Chang Y.-S., Spiegelman C.H., 2002, Locating nearby sources of air pollution by nonparametric regression of atmospheric concentrations on wind direction, *Atmospheric Environment* **36**, pp. 2237-2244.

Högström U, 1988, Non-dimensional wind and temperature profiles in the atmospheric surface layer: a re-evaluation, *Boundary-Layer Meteorology* **42**, pp. 55-78.

Hsieh C.-I., Katul G., Chi T.-W., 2000, An approximate analytical model for footprint estimation of scalar fluxes in thermally stratified atmospheric flows, *Advances in Water Resources* **23**, pp. 765-772.

Humphries R., Jenkins C., Leuning R., Zeglin S., Griffith D., Caldow C., Berko H., Feitz A., 2012, Atmospheric tomography: A Bayesian inversion technique for determining the rate and location of fugitive emissions, *Environmental Science and Technology* **46**, pp. 1739-1746.

IPCC, 2007: Climate Change 2007: The Physical Science Basis. Contribution of Working Group I to the Fourth Assessment Report of the Intergovernmental Panel on Climate Change [Solomon, S., D. Qin, M. Manning, Z. Chen, M. Marquis, K.B. Averyt, M.Tignor and H.L. Miller (Eds.)]. Cambridge University Press, Cambridge, United Kingdom and New York, NY, USA.

Kaimal J.C., Finnigan J.J., 1994, Atmospheric Boundary Layer Flows – Their Structure and Measurement, Oxford University Press, New York, 289 pgs.

Kaimal J.C., Gaynor J.E., 1991, Another look at sonic thermometry, *Boundary-Layer Meteorology* **56**, 401-410.

Keats A., Yee E., Lien F.-S., 2007, Bayesian inference for source determination with applications to a complex urban environment, *Atmospheric Environment* **41**, pp. 465-479.

Keeling R.F., 2008, Recording earth's vital signs, *Science* **28** (5871), pp. 1771-1772.

Keeling R.F., Walker S.J., Piper S.C., Bollenbacher A.F., 2013, Atmospheric CO_2 concentrations (ppm) derived from in situ air measurements at Mauna Loa Observatory, Hawaii, Available online at <http://scrippsco2.ucsd.edu/data/mlo.html>, Accessed December, 2nd 2013.

Kiehl J.T., Trenberth K. E., 1997, Earth's annual global mean energy budget, *Bulletin of the American Meteorological Society* **78**, pp. 197-208.

Kirkil G., Mirocha J., Bou-Zeid E., Chow F.K., Kosović B., 2012, Implementation and evaluation of subfilter-scale stress models for large-eddy simulation using WRF, *Monthly Weather Review* **140**, pp. 266-284.

Kljun N., Calanca P., Rotach M.W., Schmid H.P., 2004, A simple parameterization for flux footprint predictions, *Boundary-Layer Meteorology* **112**, pp. 503-523.

Kljun N., Rotach M.W., Schmid H.P., 2002, A three-dimensional backward Lagrangian footprint model for a wide range of boundary-layer stratifications, *Boundary-Layer Meteorology* **103**, pp. 205-226.

Kormann R., Meixner F.X., 2001, An analytical footprint model for non-neutral stratification, *Boundary-Layer Meteorology* **99**, pp. 207-224.

Lewicki J.L., Hilley G.E., 2012, Eddy covariance network design for mapping and quantification of surface CO_2 leakage fluxes, *International Journal of Greenhouse Gas Control* **7**, pp. 137-144.

Liu X., Ohtaki E., 1997, An independent method to determine the height of the mixed layer, *Boundary-Layer Meteorology* **85**, pp. 497-504.

Maus S., Macmillan S., McLean S., Hamilton B., Thomson A., Nair M., Rollins C., 2010, The US/UK World Magnetic Model for 2010-2015, NOAA Technical Report NESDIS/NGDC, Available online at <http://www.ngdc.noaa.gov/geomag/WMM/data/WMM2010/WMM2010_Report.pdf>, Accessed June 20th, 2013.

Miller S.M., Wofsy S.C., Michalak A.M., Kort E.A., Andrews A.E., Biraud S.C., Dlugokencky E.J., Eluszkiewicz J., Fischer M.L., Janssens-Maenhout G., Miller B.R., Miller J.B., Montzka S.A., Nehrkorn T., Sweeney C., 2013, Anthropogenic emissions of methane in the United States, *Proceedings of the National Academy of Sciences* **110** (50), pp. 20018-20022.

Moeng C-H., Dudhia J., Klemp J., Sullivan P., 2007, Examining two-way grid nesting for large eddy simulation of the PBL using the WRF model, *Monthly Weather Review* **135**, pp. 2295-2311.

Moeng C-H., Sullivan P.P., 1994, A comparison of shear- and buoyancy-driven planetary boundary layer flows, *Journal of the Atmospheric Sciences* **51** (7), pp. 999-1022.

Mylne K.R., Mason P.J., 1991, Concentration fluctuation measurements in a dispersing plume at a range of up to 1000 m, *Quarterly Journal of the Royal Meteorological Society* **117**, pp. 177-206.

National Oceanographic and Atmospheric Administration (NOAA), Aviation Digital Data Service (ADDS), Casper/Natrona County International Airport (C/NCIA) METAR, Available online at <http://aviationweather.gov/adds/metars/>, Accessed November 18th, 2012.

Nehrkorn T., Eluszkiewicz J., Wofsy S.C., Lin J.C., Gerbig C., Longo M., Freitas S., 2010, Coupled weather research and forecasting-stochastic time-inverted Lagrangian transport (WRF-STILT) model, *Meteorology and Atmospheric Physics* **107** (1-2), pp. 51-64.

Nieuwstadt F.T.M., 1992, A large-eddy simulation of a line source in a convective atmospheric boundary layer – I. dispersion characteristics, *Atmospheric Environment* **26A** (3), pp. 485-495.

Nottrott A., Keeling R., Novakovskaia E., Sloop C., Prasad K., Kleissl J., 2013a, Continuous measurement and large-eddy simulation of greenhouse gas emissions at local spatial scales, *4th North American Carbon Program All-Investigators Meeting, Albuquerque, NM.*

Nottrott A., Kleissl J., Keeling R., 2014, Modeling passive scalar dispersion in the atmospheric boundary layer with WRF large-eddy simulation, *Atmospheric Environment* **82**, pp. 172-182.

Nottrott A., Rahn T., Costigan K., Canfield J., Sauer J., Arata C., Dubey M., Keeling R., Thorpe A., Aubrey A., Frankenberg C., 2013b, Measurements and simulation of methane during a controlled release experiment for top-down emission quantification by in situ and remote sensing, *American Geophysical Union Fall Meeting, San Francisco, CA.*

Okubo A., 1971, Oceanic diffusion diagrams, *Deep-sea Research* **18**, pp. 789-802.

Panofsky H.A., Tennekes H., Lenschow D.H., Wyngaard J.C., 1977, The characteristics of turbulent velocity components in the surface layer under convective conditions, *Boundary-Layer Meteorology* **11**, pp. 355-361.

Pétron G., Frost G, Miller B.R., Hirsch A.I., Montzka S.A., Karion A., Trainer M., Sweeney C., Andrews A.E., Miller L., Kofler J, Bar-Ilan A., Dlugokencky E.J.,

Patrick L., Moore C.T., Ryerson T.B., Siso C., Kolodzey w., Lang P.M., Conway T., Novelli P., Masarie K., Hall B., Guenther D., Kitzis D., Miller J., Welsh D., Wolfe D., Tans P., 2012, Hydrocarbon emissions characterization in the Colorado Front Range: A pilot study, *Journal of Geophysical Research* **117**, doi:10.1029/2011JD016306.

Piomelli U., Balaras E., 2002, Wall-layer models for large-eddy simulations, *Annual Review of Fluid Mechanics* **34**, pp. 349-374.

Pope S.B., 2000, Turbulent flows, Cambridge University Press, Cambridge, 771 pgs.

Ramanathan V., Cicerone R.J., Singh H.B., Kiehl J.T., 1985, Trace gas trends and their potential role in climate change, *Journal of Geophysical Research* **90** (D3), pp. 5547-5566.

Raval A., Ramanathan V., 1989, Observational determination of the greenhouse effect, *Nature* **342**, pp. 758-761.

Richardson L.F., 1926, Atmospheric diffusion shown on a distance-neighbor graph, *Proceedings of the Royal Society (A)* **110**, pp. 709-727.

Roberts P.J.W., Webster D.R., 2002, Turbulent diffusion, In Shen H.H., Cheng A.H.D., Wang, K-H., Teng M.H., Liu C.C.K. (Eds.), *Environmental Fluid Mechanics: Theories and Applications* (pp. 7-45), Reston, VA: American Society of Civil Engineers.

Sarkar S., 2003, The effect of stable stratification on turbulence anisotropy in uniformly sheared flow, *Computers and Mathematics with Applications* **46**, pp. 639-646.

Schmid H.P., 1994, Source areas for scalars and scalar fluxes, *Boundary-Layer Meteorology* **67**, pp. 293-318.

Schmid H.P., 2002, Footprint modeling for vegetation atmosphere exchange studies: a review perspective, *Agricultural and Forest Meteorology* **113**, pp. 159-183.

Schotanus P., Nieuwstadt F.T.M., DeBruin H.A.R., 1983, Temperature measurement with a sonic anemometer and its application to heat and moisture fluctuations, *Boundary-Layer Meteorology* **26**, 81-93.

Shaughnessy E.J., Morton J.B., 1977, Laser light-scattering measurements of particle concentration in a turbulent jet, *Journal of Fluid Mechanics* **80** (1), pp. 129-148.

Singh S.K., Sharan M., Issartel J.-P., 2013, Inverse modeling for identification of multiple-point releases from atmospheric concentration measurements, *Boundary-Layer Meteorology* **146**, pp. 277-295.

Skamarock W.C., Klemp J.B., 2008, A time-split nonhydrostatic atmospheric model for weather research and forecasting applications, *Journal of Computational Physics* **227** (7), pp. 3465-3485.

Sloop C., Novakovskaia E., Continuous GHG monitoring at local to statewide scales, *4th NACP All-Investigators Meeting, Albuquerque, New Mexico.*

Stommel H., 1949, Horizontal diffusion due to oceanic turbulence, *Journal of Marine Research* **8**, pp. 199-225.

Stull R.B., 1988, An Introduction to Boundary Layer Meteorology, Kluwer Academic Publishers, Dordrecht, 666 pgs.

Taylor G.I., 1922, Diffusion by continuous movement, *Proceedings of the London Mathematical Society* **20**, pp. 196-212.

Taylor J.R., 1997, An introduction to error analysis: The study of uncertainties in physical measurements, University Science Books, Sausalito, 333 pgs.

Thomson D.J., 1987, Criteria for the selection of stochastic models of particle trajectories in turbulent flows, *Journal of Fluid Mechanics* 180, pp. 529-556.

Thorpe A.K., Roberts D.A., Bradley E.S., Funk C.C., Dennison P.E., Leifer I., 2013, High resolution mapping of methane emissions from marine and terrestrial sources using a cluster-tuned matched filter technique and imaging spectrometry, *Remote Sensing of Environment* **134**, pp. 304-318.

US Environmental Protection Agency (EPA), 2013, Inventory of U.S. Greenhouse Gas Emissions and Sinks: 1990-2011, Technical Report EPA 430-R-13-001, Environmental Protection Agency, Washington, Available online at <http://www.epa.gov/climatechange/Downloads/ghgemissions/US-GHG-Inventory-2013-Main-Text.pdf>, Accessed December 20th, 2012.

van Dop H., Nieuwstadt F.T.M., Hunt J.C.R., 1985, Random walk models for particle displacements in inhomogeneous unsteady turbulent flows, *Physics of Fluids* **28**, pp. 1639-1653.

Venkatram A., Wyngaard J.C. (Eds), 1988, Lectures on air pollution modeling, American Meteorological Society, Boston, 390 pgs.

Weil J.C., Sullivan P.P., Patton E.G., Moeng C-H., 2012, Statistical variability of dispersion in the convective boundary layer: ensembles of simulations and observations, *Boundary-Layer Meteorology* **145**, pp. 185-210.

Weil J.C., Synder W., Lawson Jr. R.E., Shipman M.S., 2002, Experiments on buoyant plume dispersion in a laboratory convection tank, *Boundary-Layer Meteorology* **102**, pp. 367-414.

Welp L.R., Keeling R.F., Weiss R.F., Paplawsky W., Heckman S., 2012, Design and performance of a Nafion dryer for continuous operation at CO_2 and CH_4 air monitoring sites, *Atmospheric Measurement Techniques Discussions* **5**, pp 5449-5468.

Wilczak J.M., Oncley S.P., Stage S.A., 2001, Sonic anemometer tilt correction algorithms, *Boundary-Layer Meteorology* **99**, pp. 127-150.

Willis G.E., Deardorff J.W., 1976, A laboratory model of diffusion into the convective planetary boundary layer, *Quarterly Journal of the Royal Meteorological Society* **102** (432), pp. 427-445.

Willis G.E., Deardorff J.W., 1981, A laboratory study of dispersion from a source in the middle of the convectively mixed layer, *Atmospheric Environment* **15** (2), pp. 109-117.

Wilson J.D., Sawford B.L., 1996, Review of Lagrangian stochastic models for trajectories in the turbulent atmosphere, *Boundary-Layer Meteorology* **78** (1-2), pp. 191-210.

Wyngaard J.C., 1975, Modeling the planetary boundary layer – extension to the stable case, *Boundary-Layer Meteorology* **9**, pp. 441-460.

Yee E., Chan R., 1997, A simple model for the probability density function of concentration fluctuations in atmospheric plumes, *Atmospheric Environment* **31** (7), pp. 991-1002.

Yee E., Chan R., Kosteniuk P.R., Chandler G.M., Bitloft C.A., Bowers J.F., 1995, The vertical structure of concentration fluctuation statistics in plume dispersing in the atmospheric surface layer, *Boundary-Layer Meteorology* **76** (1-2), pp. 41-67.

Yver C.E., Graven H.D., Lucas D.D., Cameron-Smith P.J., Keeling R.F., Weiss R.F., 2013, Evaluating transport in the WRF model along the California coast, *Atmospheric Chemistry and Physics* **13**, pp. 1837-1825.

Zheng X., Chen Z., 2011, Inverse calculation approaches for source determination in hazardous chemical releases, *Journal of Loss Prevention in the Process Industries* **24**, pp. 293-301.